

2-2013

Numerical Modeling of Anti-Icing Using an Array of Heated Synthetic Jets

Nikisha Maria Nagappan
Embry-Riddle Aeronautical University - Daytona Beach

Follow this and additional works at: <https://commons.erau.edu/edt>



Part of the [Aerospace Engineering Commons](#), and the [Meteorology Commons](#)

Scholarly Commons Citation

Nagappan, Nikisha Maria, "Numerical Modeling of Anti-Icing Using an Array of Heated Synthetic Jets" (2013). *Dissertations and Theses*. 109.
<https://commons.erau.edu/edt/109>

This Thesis - Open Access is brought to you for free and open access by Scholarly Commons. It has been accepted for inclusion in Dissertations and Theses by an authorized administrator of Scholarly Commons. For more information, please contact commons@erau.edu.

Numerical Modeling of Anti-Icing Using an Array of Heated Synthetic Jets

By

Nikisha Maria Nagappan

A Thesis Submitted to the

Aerospace Engineering Department

In Partial Fulfillment of the Requirements for the Degree of

Master of Science in Aerospace Engineering

Embry-Riddle Aeronautical University

Daytona Beach, Florida

February 2013

© Copyright Nikisha Maria Nagappan 2013

All Rights Reserved

NUMERICAL MODELING OF ANTI-ICING USING AN ARRAY OF HEATED SYNTHETIC JETS

By

NIKISHA MARIA NAGAPPAN

This thesis was prepared under the direction of the candidate's Thesis Committee Chair, Dr. Vladimir Golubev, Professor, Daytona Beach Campus, and has been approved by the Thesis Committee. It was submitted to the Department of Engineering in partial fulfillment of the requirements for the degree of Masters of Science in Aerospace Engineering.

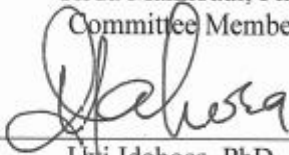
Thesis Review Committee:



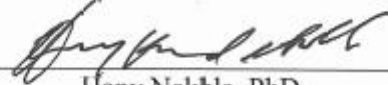
Vladimir Golubev, PhD.
Committee Chair



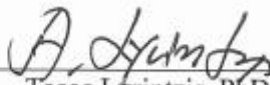
Reda Mankbadi, PhD.
Committee Member



Uyi Idahosa, PhD.
Committee Member



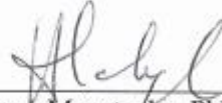
Hany Nakhla, PhD.
Committee Member



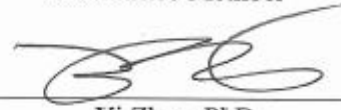
Tasos Lyrintzis, PhD.
Aerospace Engineering Department Chair



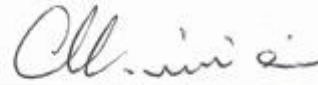
Wagdi Habashi, PhD.
Committee Member



Hany Moustapha, PhD.
Committee Member



Yi Zhao, PhD.
MSAE Graduate Program Chair



Maj Mirmirani, PhD.
Dean College of Engineering



Robert Oxley, PhD.
Associate Vice President of Academics

2-21-2019
Date



There is nothing I cannot
do in the One who
strengthens me.

-Philippians 4:13

Dedicated to God



ABSTRACT

Author: Nikisha Maria Nagappan
Title: Numerical Modeling of Anti-Icing Using an Array of Heated Synthetic Jets
Institution: Embry-Riddle Aeronautical University
Degree: Master of Science in Aerospace Engineering
Year: 2013

A novel approach to icing control using an array of thermally activated synthetic jet actuators (SJAs) embedded in a wedge surface subject to a super-cooled flow is investigated numerically. The effects of SJA actuation with and without jet heating on ice accretion are studied using the FENSAP-ICE software. It is shown that the heated actuating SJAs can lead to a significant reduction in the amount of ice accreted on the surface. Additional parametric studies on several icing and SJA parameters are analyzed for their influence on the amount of ice accretion.

ACKNOWLEDGEMENTS

I would like to sincerely thank my loving husband, Ryan M Agner for his love and support which made this work possible. Ryan, I can't thank you enough, you are a blessing in my life.

I would like to thank my advisor Dr. Golubev for providing his guidance throughout the thesis work and writing. Your ideas and suggestions were invaluable to my effort of this entire project. To my committee members Dr. Habashi, Dr. Idahosa, Dr. Nakhla, Dr. Moustapha, and Dr. Mankbadi, thank you for lending your valuable time and expertise in reviewing this body of work.

I would like to give special thanks to Dr. Habashi for lending us the FENSAP-ICE software to use in this research. Also, the members of the NTI team for their relentless help and training provided to me to attain a deeper knowledge for using this software.

I would like to thank Dr. Mankbadi, Dr. Lyrintzis, and Dr. Tang for their valuable feedback during our brown bag meetings. I would also like to thank Dr. Perrell and Dr. Drakunov for their assistance on this project.

I would like to thank my lab mates Lap Nguyen and Shibani Bhatt for their feedback and assistance in this project for the power requirement calculations.

Last but not least, to my loving Mom and sister who were with me in their prayers, love and encouragement throughout this project.

TABLE OF CONTENTS

Abstract	iv
Acknowledgements	v
Table of Contents	vi
List of Figures	viii
List of Tables	xi
Chapter 1: Introduction	1
1.1 Motivation for Research	1
1.2 Thesis Outline	3
1.3 Goals	4
Chapter 2: Theory and Literature Review	5
2.1 Classification of Supercooled Water Droplets	8
2.2 Types of Ice Accretion	12
2.3 Deicing and Anti-icing	15
2.4 Structure of Icing Code	17
2.4.1 Eulerian Droplet Impingement	17
2.4.2 Mass and Energy Balance for Ice Accretion	21
2.4.3 Conjugate Heat Transfer for Anti-Icing	26
2.5 Synthetic Jet Actuator	27
Chapter 3: Methodology/Approach	29
3.1 Test Study Cases: Wedge in Supercooled Flow	30
3.2 Numerical Implementation: Grid specifications	31
3.3 Procedure of Analysis: Transient Flow with SS CHT3D	33
3.4 Case D Parametric Studies	35
3.5 Miscellaneous Program Inputs	38
Chapter 4: Case Study Results	40
4.1 Case A: Baseline	40
4.2 Case B: Non-Actuated, Heated SJA	42
4.3 Case C: Actuated, Non-Heated SJA	44
4.4 Case D: Actuated, Heated SJA	47
4.4.1 Snapshot 1	47
4.4.2 Snapshot 2	49

4.4.3 Snapshot 3.....	51
4.4.4 Snapshot 4.....	53
Chapter 5: Case D Parametric Study	56
5.1 Parametric Study I: Droplet Distribution	56
5.1.1 Snapshot 1.....	56
5.1.2 Snapshot 3.....	57
5.2 Parametric Study II: SJA Inlet Temperature Variation.....	59
5.2.1 Snapshot 1.....	59
5.2.3 Snapshot 3.....	61
5.3 Parametric Study III: SSD and SLD	63
5.3.1 Snapshot 1.....	63
5.3.3 Snapshot 3.....	64
5.4 Parametric Study IV: Freestream Temperature Variation.....	65
5.4.1 Snapshot 1.....	66
5.4.3 Snapshot 3.....	67
5.5 One SJA anti-ice Effectiveness	69
5.6 PRELIMINARY Power Requirement for Heated and Actuated SJA.....	70
5.7 Piccolo Tube Simulation	73
Chapter 6: Conclusion.....	75
6.1 Future Work	76
References.....	77
Appendix.....	79
A.1 Validation of Numerical results to analytical model.....	79
A.2 Case D, Snapshot 2 Flow Comparison with previous FLUENT results	81
A.3 Additional Results From Chapter 5.....	82
Case D: Droplet Distribution Comparison	82
Case D: SJA Temperature Comparison.....	87
Case D: SSD vs SLD	90
Case D: Freestream Temperature Comparison.....	94

LIST OF FIGURES

Figure 1: Statistical Analysis of Icing Due to Various Factors [1].....	3
Figure 2: Prediction of large areas of icing potential (Left) and a longer flight map to avoid a front (Right) [1].....	6
Figure 3: (a) Cumulus congestus (b) Cumulonimbus calvus precipitation (c) Cumulonimbus capillatus incus [2]......	7
Figure 4: Distribution of supercooled water droplets in clouds [8].....	9
Figure 5: Relative droplet sizes in microns [11].....	9
Figure 6: Droplet trajectories for (a) 20 micron and (b) 100 MICRONS [10].....	11
Figure 7: Formation SLD due to freezing rain [12].....	12
Figure 8: Formation of SLD by collision-coalescence process [11].....	12
Figure 9: Ice Accretion process. Formation of glaze ice (top) and rime ice (bottom) [8].....	13
Figure 10: Glaze ice shapes [12].....	14
Figure 11: Rime ice shape (Left) and mixed ice shape (Right) [12].....	14
Figure 12: (a) Pneumatic Boot (b) Weeping wing close-up [1] (c) Thermal bleed anti-icing (d) Weeping wing [12].....	16
Figure 13: Definition of local collection efficiency [17].....	21
Figure 14: Water film layer model used in ICE3D [18].....	23
Figure 15: Mass balance (left) and energy balance (right) in a control volume [4].....	24
Figure 16: Schematic of a Synthetic Jet Actuator [25].....	28
Figure 17: FENSAP-ICE Procedure.....	29
Figure 18: Test Case Diagram.....	30
Figure 19: Grid designed for a wedge with a series of six SJAs (left); close-up view of SJA region (right).....	32
Figure 20: Grid for the solid domain.....	33
Figure 21: Graphical Representation of Time Snapshots.....	34
Figure 22: SSD Langmuir-d distribution (left) and SID langmuir-D distribution (right).....	37
Figure 23: Pressure (Left), Velocity (Middle) and Temperature (Right) Contours. Bottom contours are closeups.....	41
Figure 24: Ice Accumulation. Smaller picture is of the front of the wedge.....	41
Figure 25: Instant Ice Growth Plot.....	42
Figure 26: Pressure (Left), Velocity (Middle) and Temperature (Right) Contours. Bottom contours are closeups.....	43
Figure 27: Ice Accumulation. Smaller picture is of the front of the wedge.....	43
Figure 28: Instant Ice Growth Plot.....	44
Figure 29: Pressure (Left), Velocity (Middle) and Temperature (Right) Contours. Bottom Contours are Closeups.....	45
Figure 30: Ice Accumulation. Smaller Picture is of the Front of the Wedge. Langmuir-D distribution (Left) monodisperse (right).....	46
Figure 31: Instant Ice Growth Plot. Langmuir-D distribution (Left) monodisperse (right).....	46
Figure 32: Pressure (Left), Velocity (Middle) and Temperature (Right) Contours. Bottom contours are closeups.....	47
Figure 33: Ice Accumulation. Smaller picture is of the front of the wedge.....	49

Figure 34: Instant Ice Growth Plot.....	49
Figure 35: Pressure (Left), Velocity (Middle) and Temperature (Right) Contours. Bottom contours are closeups.	50
Figure 36: Ice Accumulation. Smaller picture is of the front of the wedge.....	51
Figure 37: Instant Ice Growth Plot.....	51
Figure 38: Pressure (Left), Velocity (Middle) and Temperature (Right) Contours. Bottom contours are closeups.	52
Figure 39: Ice Accumulation. Smaller picture is of the front of the wedge.....	53
Figure 40: Instant Ice Growth Plot.....	53
Figure 41: Pressure (Left), Velocity (Middle) and Temperature (Right) Contours. Bottom contours are closeups.	54
Figure 42: Ice Accumulation. Smaller picture is of the front of the wedge.....	55
Figure 43: Instant Ice Growth Plot.....	55
Figure 44: Ice Accumulation (monodisperse left, Langmuir right)	57
Figure 45: Ice Thickness Plot (monodisperse left, Langmuir right)	57
Figure 46: Ice Accumulation (monodisperse left, Langmuir right)	58
Figure 47: Ice Thickness Plot (monodisperse left, Langmuir right)	59
Figure 48: Ice Accumulation (Inlet Temperature: 75C left, 100C right).....	60
Figure 49: Ice Thickness Plot (Inlet Temperature: 75C left, 100C right).....	60
Figure 50: Solid Temperature (Inlet Temperature: 75C left, 100C right)	61
Figure 51: Ice Accumulation (Inlet Temperature: 75C left, 100C right).....	62
Figure 52: Ice Thickness Plot (Inlet Temperature: 75C left, 100C right).....	62
Figure 53: Solid Temperature (Inlet Temperature: 75C left, 100C right)	63
Figure 54: Ice Accumulation (SSD left, SLD right)	64
Figure 55: Ice Thickness Plot (SSD left, SLD right)	64
Figure 56: Ice Accumulation (SSD left, SLD right)	65
Figure 57: Ice Thickness Plot (SSD left, SLD right)	65
Figure 58: Ice Accumulation (Freestream temperatures of -20C left, -10 right).....	66
Figure 59: Ice Thickness Plot (Freestream temperatures of -20C left, -10 right).....	66
Figure 60: Solid Temperature (Freestream temperatures of -20C left, -10 right)	67
Figure 61: Ice Accumulation (Freestream temperatures of -20C left, -10 right).....	68
Figure 62: Ice Thickness Plot (Freestream temperatures of -20C left, -10 right).....	68
Figure 63: Solid Temperature (Freestream temperatures of -20C left, -10 right)	68
Figure 64: Ice Accretion using One SJA	69
Figure 65: Ice Thickness Plot using one SJA	70
Figure 66: CHT3D convergence history for heat flux for Internal and External piccolo tube	73
Figure 68: Incompressible and Irrotational flow past a wedge [35]	80
Figure 69: Analytical solution for streamlines.....	80
Figure 70: Velocity flow field comparison. FEnsap (left) Fluent (right).....	81
Figure 71: temperature field comparison. FEnsap (left) Fluent (right).....	82
Figure 72: Collection Efficiency (monodisperse left, Langmuir right)	83
Figure 73: Collection Efficiency (monodisperse left, Langmuir right)	83
Figure 74: Ice Accumulation (monodisperse left, Langmuir right)	84
Figure 75: Ice Thickness Plot (monodisperse left, Langmuir right).....	84

Figure 76: Collection Efficiency (monodisperse left, Langmuir right)	85
Figure 77: Collection Efficiency (monodisperse left, Langmuir right)	85
Figure 78: Ice Accumulation (monodisperse left, Langmuir right)	86
Figure 79: Ice Thickness Plot (Monodisperse Left, Langmuir, Right).....	86
Figure 80: Ice Accumulation (Inlet Temperature: 75C left, 100C right).....	87
Figure 81: Ice Thickness Plot (Inlet Temperature: 75C left, 100C right).....	87
Figure 82: Solid Temperature (Inlet Temperature: 75C left, 100C right)	88
Figure 83: Ice Accumulation (Inlet Temperature: 75C left, 100C right).....	88
Figure 84: Ice Thickness Plot (Inlet Temperature: 75C left, 100C right).....	89
Figure 85: Solid Temperature (Inlet Temperature: 75C left, 100C right)	89
Figure 86: Collection Efficiency (SSD left, SLD right)	90
Figure 87: Collection Efficiency (SSD left, SLD right)	90
Figure 88: Ice Accumulation (SSD left, SLD right)	91
Figure 89: Ice Thickness Plot (SSD left, SLD right)	91
Figure 90: Collection Efficiency (SSD left, SLD right)	92
Figure 91: Collection Efficiency (SSD left, SLD right)	92
Figure 92: Ice Accumulation (SSD left, SLD right)	93
Figure 93: Ice Thickness Plot (SSD left, SLD right)	93
Figure 94: Ice Accumulation (Freestream temperatures of -20C left, -10 right).....	94
Figure 95: Ice Thickness Plot (Freestream temperatures of -20C left, -10 right).....	94
Figure 96: Solid Temperature (Freestream temperatures of -20C left, -10 right)	95
Figure 97: Ice Accumulation (Freestream temperatures of -20C left, -10 right).....	95
Figure 98: Ice Thickness Plot (Freestream temperatures of -20C left, -10 right).....	95
Figure 99: Solid Temperature (Freestream temperatures of -20C left, -10 right)	96

LIST OF TABLES

Table 1: ASRS Data for Icing Versus Weather Accidents 1997-2006 [27]	2
Table 2: Icing Categories according to Metrological definition [2].	5
Table 3: Summary of Cases	31
Table 4: Time Snapshots for quasi steady analysis	33
Table 5: Parametric cases run for case D.....	35
Table 6: Case D Parametric Study Summary	38

CHAPTER 1: INTRODUCTION

Inflight icing adversely affects the performance of an aircraft by increasing drag due to the roughness or shape of the accreted ice, reducing lift, decreasing stall angle and modifying longitudinal and lateral stability. Ice accretion in the preliminary stage can reduce the lift and increase drag drastically. Experimental and in flight tests have proven that an ice accumulation on the leading edge or the upper surface of the wing as thick or rough as a course sand paper can reduce the lift up to 30% and increase the drag up to 40% whereas larger accretion could increase drag up to 80% or even more[1]. Addition of weight is not a major concern for larger commercial aircrafts but can be a potential threat to a smaller aircraft. Icing on engine components such as nacelles can reduce the engine performance furthermore the accreted ice could flake off and be ingested into the engine causing damage to the engine components or even flame out.

1.1 MOTIVATION FOR RESEARCH

Ice accretion on an aircraft surface has caused fatal accidents throughout the years. The data recorded by Aviation Safety Reporting System (ASRS), was analyzed by National Aeronautics and Space Administration (NASA) Langley Research Center [27]. The ASRS database consists of all types of aircraft accident reports and these accidents are reported by a voluntary system where the repartees can be anyone who is involved with the accident such as crew members. The database is then reviewed and screened by the authorities and is available in <http://asrs.arc.nasa.gov>. The table below shows the accident reports from 1997-2006;

Year	# All	# weather	# Icing	% all	% weather
1997	8018	332	52	.65	16
1998	8428	276	34	.40	12
1999	9866	245	29	.29	12
2000	7998	232	38	.48	16
2001	8612	197	21	.24	11
2002	7198	201	26	.36	13
2003	8143	266	32	.39	12
2004	6200	161	27	.44	17
2005	3524	109	25	.71	23
2006	5196	188	11	.21	9

TABLE 1: ASRS DATA FOR ICING VERSUS WEATHER ACCIDENTS 1997-2006 [27]

Weather related accidents contributed approximately 10-20 percent of all aircraft accidents. This is very significant number even though the total number of accidents has much higher numbers, ice accretion accidents are weather related and they have significant impact. Although the later years have lesser number of icing accidents reported those were all recorded around the same time frame.

A pie chart of accident reports can be seen in Figure 1, for various factors [1]. The figure accounts for weather related accidents occurred during the years of 1990-2000 and 27 percent of those accidents involved fatalities. The figure shows the icing accidents contributed 12 percent of total weather related accidents and they are mainly due to in-flight icing. Structural icing is due to the ice accretion on the aircraft surfaces such as wings, stabilizers or the fuselage. Structural icing contributes the penalties in aerodynamic performance as discussed above. The structural icing contributes 40 percent of icing accidents. The induction icing is caused by ice accreting in the carburetor or in fuel injected engine, ice blocking the air low inlet causes 52 percent of the

accidents. Even experienced pilots with over 1000 flight hours have difficulties during icing condition as they contribute 48 percent of accidents. Icing tends to affect smaller general aviation aircrafts [3] than commercial aircrafts as they have greater capabilities of anti-icing/deicing systems installed. The general aviation aircrafts fly at lower altitudes where icing conditions are more dominant.

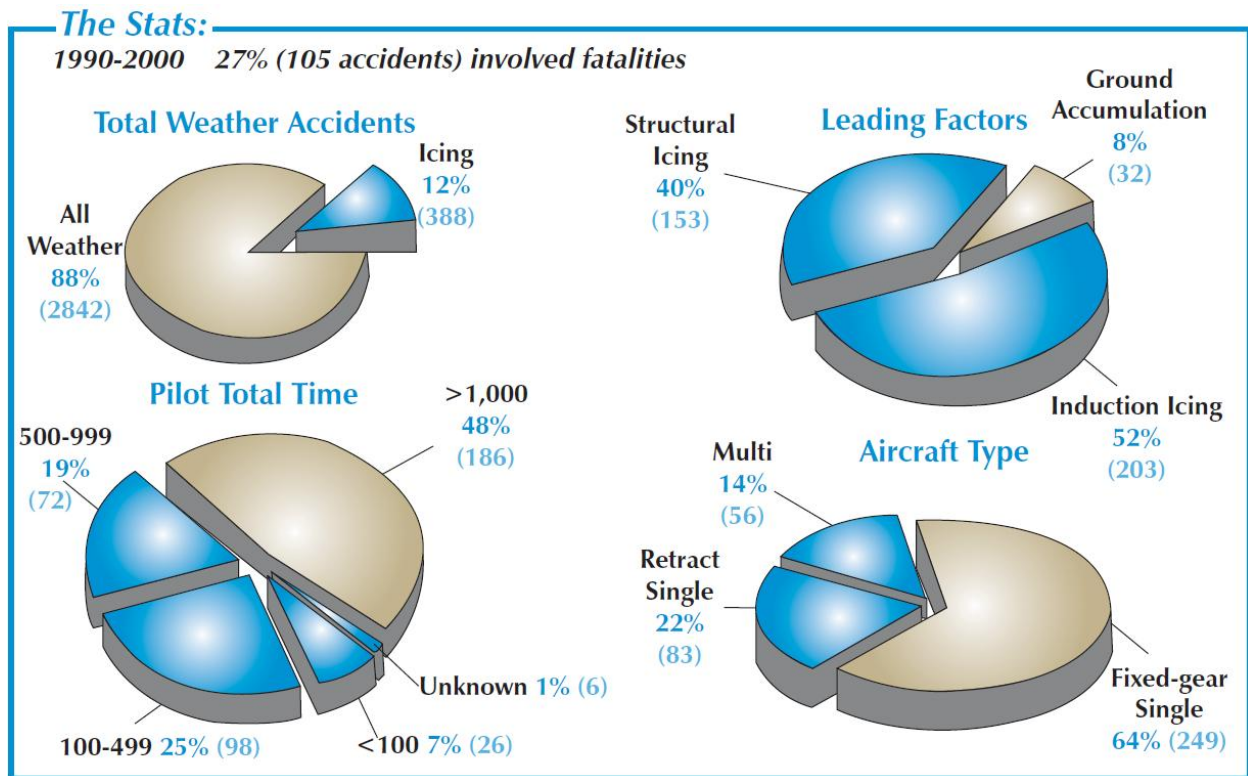


FIGURE 1: STATISTICAL ANALYSIS OF ICING DUE TO VARIOUS FACTORS [1]

1.2 THESIS OUTLINE

Chapter 2 covers the basics of the icing such as parameters influencing icing, conditions, and the theory. Chapter 3 includes the methodology used for this research and the parametric study details. Chapter 4 demonstrated the results obtained from different Synthetic Jet Actuators

on and off phases with and without heat. Chapter 5 shows results from parametric study analysis and following conclusion in Chapter 6.

1.3 GOALS

An approach to icing control using an array of thermally activated Synthetic Jet Actuators (SJAs) embedded in a wedge surface subject to a super-cooled flow is investigated numerically.

CHAPTER 2: THEORY AND LITERATURE REVIEW

Icing conditions are classified into different categories according to the damage it could inflict to the aircraft performance and the measures needed to respond to the conditions. In a trace ice formation, ice becomes visible [4], but not dangerous even without the ice protection systems and occurs when the rate of accretion is slightly larger than the rate of sublimation. Although, after a prolonged exposure (more than an hour) may require activation of deicing/anti-icing systems [2, 4]. A light ice formation could generate aerodynamic penalties after extended exposure and intermittent use of deicing/anti-icing procedure will prevent any ice formation. In moderate icing condition, a short period of exposure could be potentially hazardous and constant use of deicing/anti-icing will be required. Considerable aerodynamic performance degradation will occur as ice grows and extended exposure (no more than 45 minutes) is not advised [4]. And finally a severe case of accumulation is when a deicing/anti-icing system would fail and immediate flight diversion is mandatory. The above classification is highly dependent on the size of the aircraft as a light accretion for a larger commercial aircraft could be hazardous to smaller propeller driven aircrafts. Hence a more generalized classification (Table 2) are used by meteorologist using Liquid Water Content (LWC), which is the mass of water per volume of cloud or density of liquid water in a cloud and has units of g/m^3 [2].

METEOROLOGICAL DEFINITION	
Icing Category	LWC (g/m^3)
Trace	< 0.1
Light	0.11-0.6
Moderate	0.61-1.2
Severe	>1.2

TABLE 2: ICING CATEGORIES ACCORDING TO METROLOGICAL DEFINITION [2].

LWC plays an important role in determining the amount of water required for icing and is one of the three primary factors that influence icing. The higher value of LWC implies a greater impingement of water droplets on an aircraft surface thus increasing the ice accretion [4]. The other two major parameters are freestream temperature and average mean droplet diameter aka Mean Volume Diameter (MVD) [2].

For ice accretion, existence of water droplets with appropriate LWC in clouds and freestream temperature below zero degrees centigrade (32 degree Fahrenheit) is essential and these parameters are recorded to predict large icing areas (Figure 2, Left). Since most pilot reports of icing near the fronts, weather predictions play an important role in order to avoid icing conditions [3].

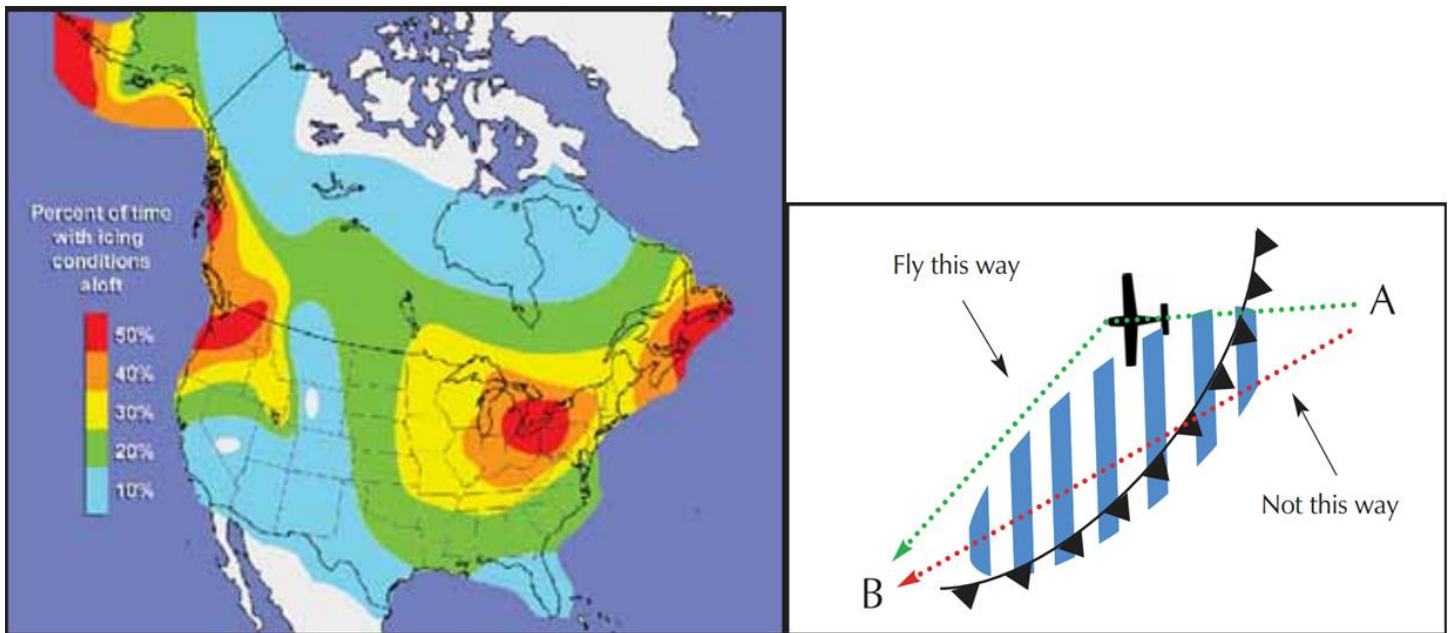


FIGURE 2: PREDICTION OF LARGE AREAS OF ICING POTENTIAL (LEFT) AND A LONGER FLIGHT MAP TO AVOID A FRONT (RIGHT) [1].

Even though the prediction of large icing potential is done with ease, prediction of more precise location and attitude of icing potential is more of a challenge as there are numerous

parameters other than the primary one's, such as geographical features, wind, atmospheric pressure variation etc. and needs to be considered. Pilot reports indicated that the most frequent icing condition occurs in front of or adjacent to surface warm fronts that provide air with high LWC if the freestream temperature is in between 0°C and -20°C [3]. Hence usually a longer route (Figure 2, Right) is chosen by aircrafts to avoid the fronts as much as possible to reduce ice accretion and accidents.

As the dry clouds, which have a very low LWC, do not pose a threat of icing, the wet clouds that have a tremendous amount of moisture are a serious threat to the aircraft. As a cloud consists of water droplets it can also have ice crystals or a combination of both. Ice crystals are not a threat as they tend not to attach on aircraft surfaces. The clouds under the consideration of icing study are only the one's that contain water droplets or clouds that are a combination of droplets and ice crystals [2].



FIGURE 3: (A) CUMULUS CONGESTUS (B) CUMULONINBUS CALVUS PRECIPITATION (C) CUMULONINBUS CAPILLATUS INCUS [2].

Cloud water droplet contents are identified by the sharpness of the cloud edge as shown in Figure 3 which represents a Cumulus congestus cloud. These clouds are a major threat to an

aircraft in flight as they mostly consist of water droplets at ambient temperatures down to -20°C . The updraft in convective clouds differ its composition of water droplets by moving them higher and increasing their size with altitude thus varying the icing risk [5]. The common values of LWC found of highly convective clouds like Cumulus is less than 0.5 g/m^3 to 0.7 g/m^3 and could reach up to values of $\sim 1.2\text{-}1.3\text{ g/m}^3$ or higher [3]. A Cumulonimbus cloud (Figure 3) contains a mixture of both water droplets and ice crystals with a LWC of less than 0.3 g/m^3 to 0.5 g/m^3 . The Cumulonimbus capillatus incus (Figure 3) are large ice crystal clouds that poses little to no threat to the aircraft [2, 3].

2.1 CLASSIFICATION OF SUPERCOOLED WATER DROPLETS

Supercooling is the process of lowering the temperature of a liquid or a gas below its freezing point without changing their phase to solid. The supercooled water droplets can maintain their liquid phase if the cloud condensation nuclei (small particles typically $1/100^{\text{th}}$ the size of water droplets [7]) is absent. The water droplets present in the Stratiform and cumuliform clouds are called supercooled water droplets when the ambient temperature is between 0°C and -40°C [9]. In ambient temperatures below negative 40°C , the supercooled water droplets will crystalize without the need of ice nuclei and are not a threat to airframe icing but could cause engine flameout. These supercooled water droplets are very unstable and will freeze, completely or partially depending on the size of the droplet, on contact with an aircraft structure in below freezing ambient temperatures. In Figure 4, a distribution of water droplets, supercooled water droplets and ice crystals are shown with a temperature scale corresponding to their formation in clouds. Note the existence of supercooled water droplets even lower than -40°C when there is an updraft in the atmosphere causing a very flavorful icing condition in those areas.

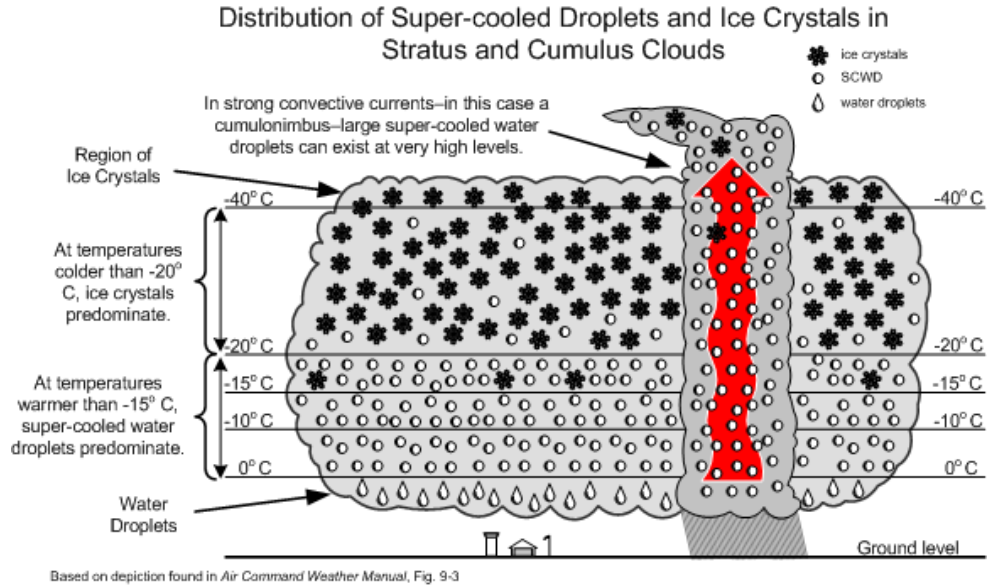


FIGURE 4: DISTRIBUTION OF SUPERCOOLED WATER DROPLETS IN CLOUDS [8]

Supercooled water droplets are classified into two categories depending on their MVD. Supercooled Small Droplets (SSD) has a MVD between $10\mu\text{m}$ to $50\mu\text{m}$ and due to their lower mass they will follow the streamlines of the flow, which may lead to the droplets avoiding impact with the aircraft surface. The airflow effect of a supercooled droplet is directly proportional to the square of the diameter while the mass of a droplet is directly proportional to the cube of droplet diameter [9]. The second criterion is far more serious problem to aircraft icing than SSD and they are Supercooled Large Droplets (SLD) with MVD exceeding $50\mu\text{m}$ and could go as high as few millimeters.

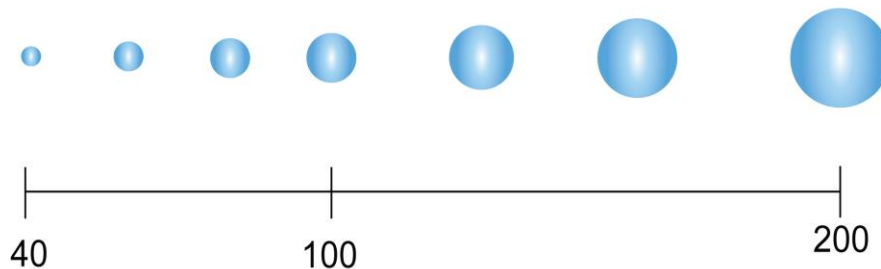


FIGURE 5: RELATIVE DROPLET SIZES IN MICRONS [11]

A relative droplet size comparison between SSD and SLD can be seen in Figure 5. The initial droplet of $40\mu\text{m}$, shown in the figure is towards a higher end of SSD and the $200\mu\text{m}$ is a middle ranged SLD as they can be even larger than $400\mu\text{m}$.

As these SLD have higher mass they possess higher inertia and could deviate from the streamline flow and follow a much straighter path towards colliding the airframe structure. SLD is capable of impacting much aft of an airfoil than SSD, where these areas may not be protected from deice/anti-ice system. A comparison between $20\mu\text{m}$ and $100\mu\text{m}$ supercooled water droplet trajectories are shown in Figure 6, where a $100\mu\text{m}$ water droplet impinges further back than the smaller $20\mu\text{m}$ droplet. The SLD could run back along the aircraft surface before freezing and roughness from this accreted ice will induce a much greater drag than SSD impinging close to the stagnation point (Refer Figure 6) at the leading edge [3].

The area where the droplet has a direct hit is known as impingement limit and the areas where it could run back and accrete are called impingement zones. The impingement zones cover more area than impingement limit and for a SSD ice accretes only at the impingement limits as SSD follows the streamlines and does not have contact with the surface. This can be observed in rime ice formation which is discussed later.

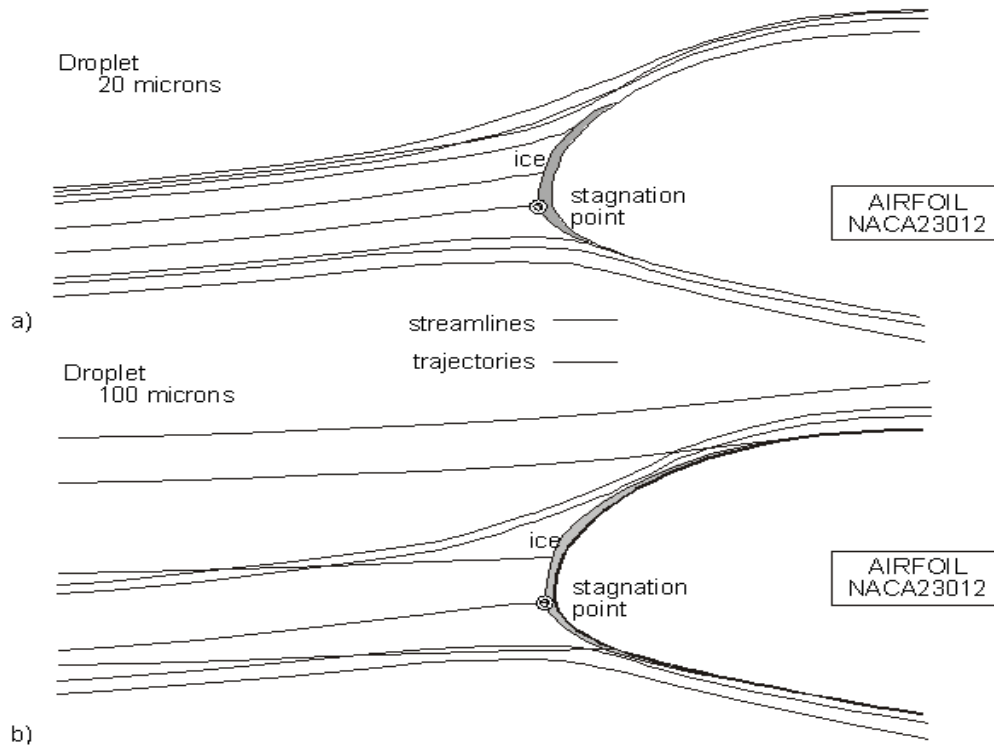


FIGURE 6: DROPLET TRAJECTORIES FOR (A) 20 MICRON AND (B) 100 MICRONS [10]

Formation of SLD is due to two circumstances, freezing rain or freezing drizzle and these two processes differs from one another on the processes of formation of SLD and also the diameter of the supercooled droplets. Freezing rain is the result of snow from upper clouds falling into layers of clouds or atmosphere where it is warmer where it melts to form larger rain droplets greater than $400\mu\text{m}$ [9]. If these rain droplets fall or pass through an atmospheric layer where temperatures are below 0°C , SLD are formed. Freezing rain is common with frontal conditions where temperature inversions can exist. These temperature inversions provide ideal conditions for the melted snow to supercool again. The freezing rain process is demonstrated in Figure 7, where the snow from aloft is melted and then supercooled in lower atmospheric layers to form SLD.

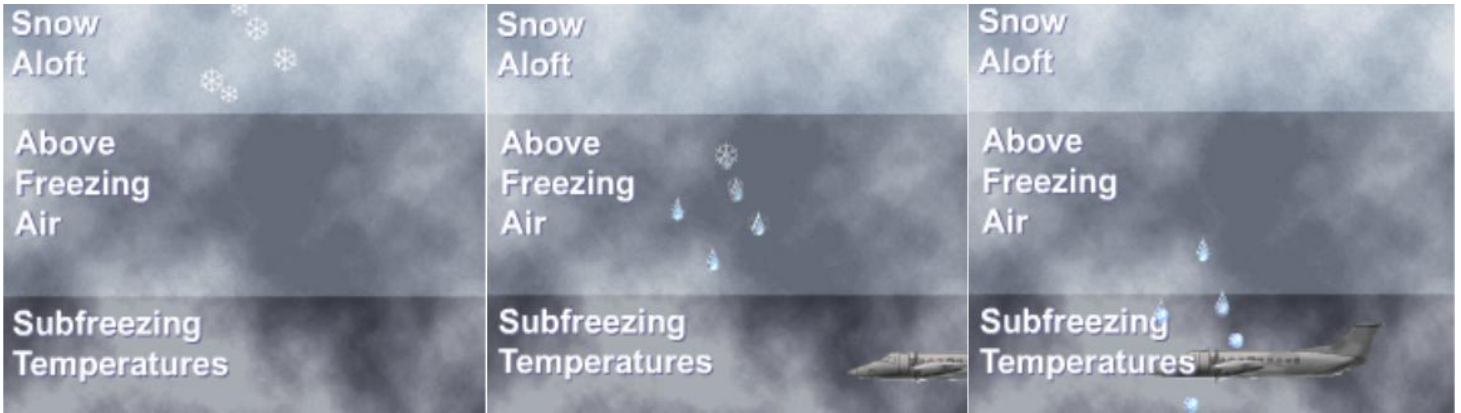


FIGURE 7: FORMATION SLD DUE TO FREEZING RAIN [12]

Freezing drizzle is formed due to collision-coalescence process and creates SLD of sizes between $50\mu\text{m}$ and $400\mu\text{m}$ [9]. The process of freezing drizzle is explained in Figure 8, where the Stratiform clouds due to turbulence under goes a coalescence process forming large droplets. As the Stratiform clouds lack much vertical extent these droplets falls down as rain before they can attain a higher droplet diameter. The aircrafts are more likely to encounter SLD from by freezing drizzle process rather than freezing rain.

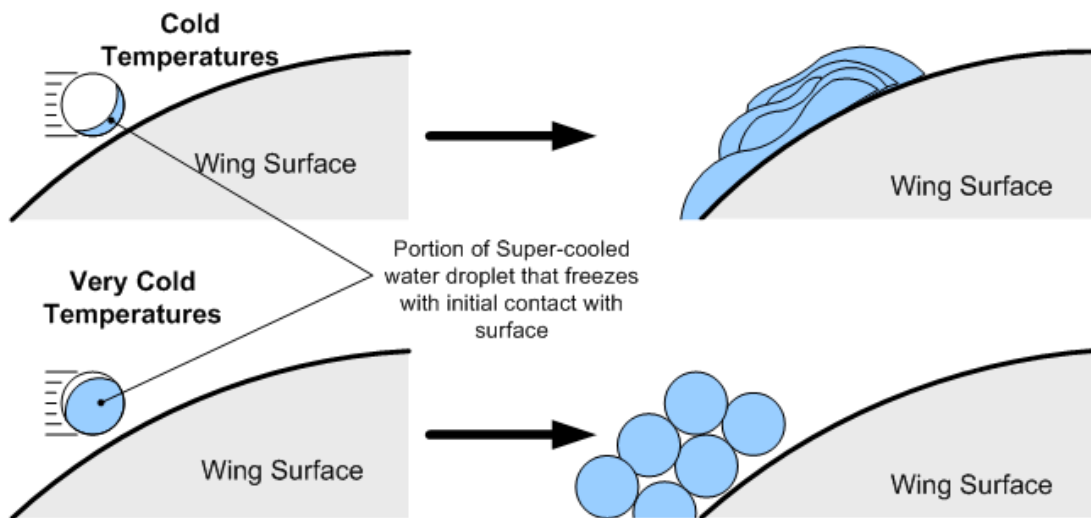


FIGURE 8: FORMATION OF SLD BY COLLISION-COALESCENCE PROCESS [11]

2.2 TYPES OF ICE ACCRETION

Formation of ice shape depends on the freestream temperature, droplet size and LWC. According the texture and shape the ice accretion can be classified to glaze, rime, mixed, run back and frost [10].

A glaze ice formation is more likely to occur in cumuliform clouds at temperatures between 0°C and -10°C and also in the presence of SLD [4]. The glaze ice formation occurs as the portion of the impinged droplet in contact with the surface freeze instantly but the rest of the droplet remain in liquid form due to the insufficient heat transfer and flows back or run back as shown in Figure 9 (top). This frozen run back water acts as a barrier and allow accumulation of ice in same area creating horn like structures. These irregular shapes formed with horns (Refer Figure 10) can adversely affect the aircraft aerodynamics by inducing tremendous amount of drag. Glaze ice lacks air pockets as they are formed slower by creating a water film due to run back and then freezing this water film. As a result, the glaze ice is transparent making it harder to notice by an eye inspection and it is very cohesive and dense hence harder to break off. Due to the run back from SLD glaze ice could form in the areas where deice/anti-ice protection system does not cover and could be potentially hazardous to the aircraft.



Based on depiction found in Fig. 9-4 of Air Command Weather Manual.

FIGURE 9: ICE ACCRETION PROCESS. FORMATION OF GLAZE ICE (TOP) AND RIME ICE (BOTTOM) [8]

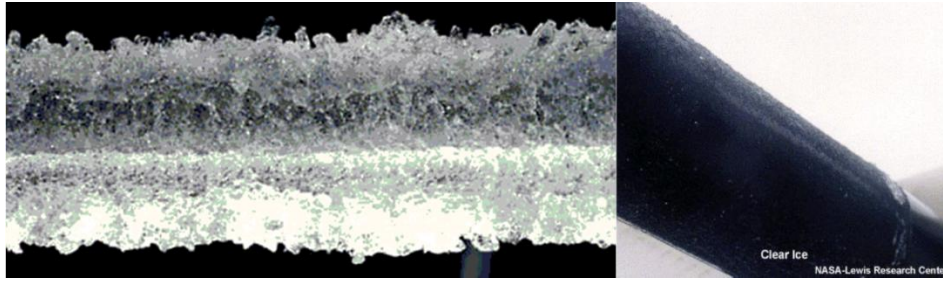


FIGURE 10: GLAZE ICE SHAPES [12]

Rime ice is formed in extremely cold freestream temperatures with moderate amount of LWC and smaller MVD. The droplets freeze immediately on contact with the airframe with no run back (Refer Figure 9, bottom) and as a result, rime ice takes the shape of the structure. Since the rime ice takes the shape of the airframe structure, this type of ice induces less aerodynamic penalties than glaze ice even with added thickness and roughness (compared to a clean airfoil). Due to the sudden freezing, rime ice traps air molecules inside, thus it is opaque and very easy to identify and flake off, of the airframe structure. Rime ice shape can be seen in Figure 11 (left), formed in the leading edge of an airfoil.

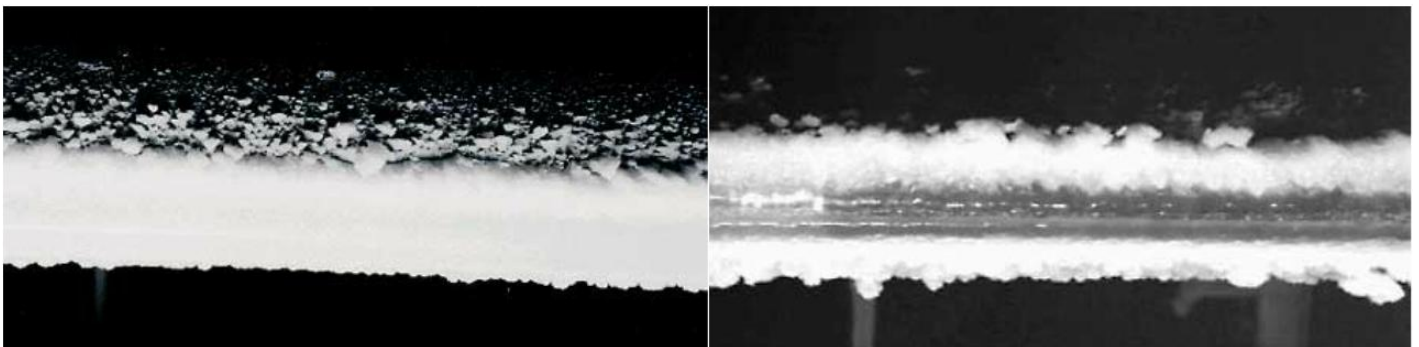


FIGURE 11: RIME ICE SHAPE (LEFT) AND MIXED ICE SHAPE (RIGHT) [12]

A combination of both rime and glaze ice is called mixed ice as it has the density of rime ice but the property of glaze. In the laminar region, near stagnation point a glaze ice will be formed and in the turbulent zone further upstream of airfoil, rime ice formation will occur with

feather like structures called rime feathers [4]. In Figure 11 (right), formation of transparent glaze ice can be seen at the stagnation point and at the upstream opaque rime ice with rime feathers on the top and bottom surfaces.

2.3 DEICING AND ANTI-ICING

To minimize performance penalties and escape icing environments, most aircraft are equipped with some form of icing protection system. Icing protection is of two types: an anti-ice system and a deice system. A commonly used deicing system is pneumatic boot and two widely used anti-ice systems are weeping wing and thermal bleed anti ice system.

The first type prevents the formation of ice completely from the protected areas and the later removes it after a certain amount is accumulated. There are different types of deice systems. An example of a deice system is pneumatic boot, located on the leading edge of the wing. The boot has inflatable rubber strips, and when ice accretes they are activated using pressurized air from compressor, which allows the boots to expand and break off the accreted ice from the surface (Refer Figure 12), which will be carried away by the airflow [1]. The inflated boot will be returned to the original shape once the ice is removed using a suction process. A boot protection can be usually seen leading edges of the wing, horizontal tail and vertical stabilizers.

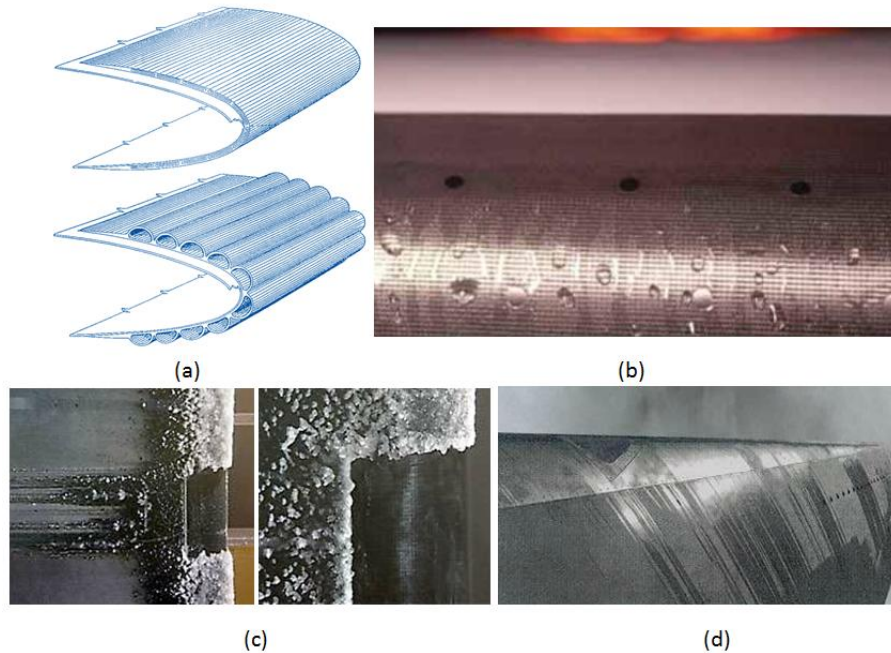


FIGURE 12: (A) PNEUMATIC BOOT (B) WEEPING WING CLOSE-UP [1] (C) THERMAL BLEED ANTI-ICING (D) WEEPING WING [12]

An anti-ice system will be activated prior to entering the icing conditions to prevent the formation of ice. Thermal bleed air anti-icing can be seen in commercial aircrafts where the hot bleed air for anti-icing is provided by the last stages of the compressor and for the small aircrafts the hot air is provided by heaters. This hot air is then ducted in the areas of interest such as wings, nacelles, vertical and horizontal tail [12]. The efficiency of this type of anti-ice system is very low due to the loss in engine efficiency from the bleed and the bleed air heat loss before reaching the desired surface. Thus to maintain the surface at required temperature demands more bleed air. If there is insufficient heat to completely evaporate the water droplets impinged, they form a water film and run back ice will be formed in the unprotected region. The run back ice formed in the unprotected region can be seen in Figure 12(c) with zoom in on the right.

A weeping wing anti-ice system is not widely used as the thermal hot air bleed system. The system uses an antifreeze ice protection fluid pumped from panels mounded on the leading

edge to wings horizontal and vertical tail. The impinging supercooled water droplet mixes with the freezing point depressant solution and flows off the surface. The solution consists mostly of glycol along with alcohol and de-ionized water [13]. A wing undergoing the process of anti-ice fluid can be seen in Figure 12 (b) zoomed in and full wing in (d).

2.4 STRUCTURE OF ICING CODE

The general structure of an ice prediction code includes four different steps. The initial step is to obtain the flow solution around the surface of interest. Using this flow solution, impingement limit is calculated for the impacting droplets. The third step is to find the ice accretion parameters and finally to perform energy balance to perform ice accretion. The ice accreted through this process will be subjected under an anti-icing/deicing segment using a conjugate heat transfer method to analyze its efficiency. The icing code for the interest of this study is FENSAP-ICE developed by Newmerical Technologies International, Montréal, Canada [14]. FENSAP-ICE consists of the FENSAP flow solver, DROP3D, ICE3D, and CHT3D, which analyzes the structures explained above.

2.4.1 EULERIAN DROPLET IMPINGEMENT

DROP3D uses an Eulerian approach to droplet impingement instead of the traditional Lagrangian so that the calculation is much faster. The Lagrangian formulation tracks each individual supercooled water droplet trajectories which may or may not hit the surface. This method is computationally expensive due to the amount of droplets that needs to be individually tracked in order to form a complete droplet impingement solution. Thus a set of Navier-Stokes or Eulerian based two fluid model reformed for droplet related continuity and momentum equations as given in Equation 2.2 and Equation 2.3 are used [15]. Although, water droplets are present in

coupled air and droplet model, a classical Navier-Stokes equations which are the basis for compressible flow calculations, could be used without alterations as the flow and droplets are kept independent. The bulk density ratios are given below (mass of the phase in mixture per unit volume) in Equation 2.1

$$Mass\ loading = \frac{\rho_{B\,Droplet}}{\rho_{B\,Air}} \cong 10^{-3} \quad \text{EQUATION 2.1}$$

Where $\rho_{B\,Droplet}$ is the bulk density of the droplet and $\rho_{B\,Air}$ is the bulk density of air. Navier-Stokes equations are valid for very small mass loading less than the order of 10^{-1} [16].

For in-flight icing scenarios certain assumptions hold true and could be applied to the Navier-Stokes continuity and momentum equations. The following five assumptions are considered in DROP3D calculations [16]:

- The droplet is assumed to be perfectly spherical with no deformations or breaking
- Droplets are assumed to have no collisions, coalescence or splashing
- Heat and mass transfer between the droplets and the surrounding air is neglected
- The turbulence effects from the atmosphere to the droplet is ignored
- Forces acting on the droplets are air, drag, buoyancy and gravity

Turbulent effect of flow around the droplet and the collisions-coalescence of the droplets are directly related as the collisions and coalescence are caused due to turbulence. Another parameter neglected for the simplicity is atmospheric pressure gradient and droplet interaction. Applying these assumptions continuity and momentum [16] is as follows.

$$\frac{\partial \alpha}{\partial t} + \nabla \cdot (\alpha u) = 0 \quad \text{EQUATION 2.2}$$

$$\frac{\partial u}{\partial t} + u \cdot \nabla u = \left(\frac{C_d Re_d}{24K} \right) (u_a - u) + \left(1 - \frac{\rho_a}{\rho} \right) \left(\frac{1}{Fr^2} \right) g \quad \text{EQUATION 2.3}$$

Where $\alpha(x, t)$ is the mean non-dimensionalized volume fraction of water; $u(x, t)$ is the mean non dimensionalized velocity of the water droplets with respect to freestream velocity (u/U_∞); u_a is the non-dimensionalized air velocity; ρ_a is the air density; ρ is the density of water; d is the diameter of water droplets; U_∞ is the speed of air at ∞ (infinity); L is the characteristic length of the impinging surface and μ is the dynamic viscosity of air.

The droplet Reynolds number is given by the expression;

$$Re_d = \frac{(\rho d U_\infty |u_a - u|)}{\mu} \quad \text{EQUATION 2.4}$$

The droplet Reynolds number is a measure of how the droplet breaks apart on impact with the surface. A higher droplet Reynolds number will cause an impinging droplet to break up into many smaller droplets which can be carried away by the flow, thus an important parameter in determining ice accretion.

The inertia parameter K is obtained from empirical relation;

$$K = \frac{\rho d^2 U_\infty}{18L\mu} \quad \text{EQUATION 2.5}$$

The drag coefficients for spherical droplets, C_D is obtained from empirical relation;

$$C_D = \left(\frac{24}{Re_d} \right) (1 + 0.015 Re_d^{0.687}) \quad \text{EQUATION 2.6}$$

The above equation is valid for $Re_d \leq 1000$, and for $Re_d > 1000$ the drag coefficient can be taken as $C_D = 0.4$

The Froude number Fr is obtained from the following relation;

$$Fr = \frac{(U_{\infty})}{\sqrt{Lg}} \quad \text{EQUATION 2.7}$$

The Froude number is defined as a ratio of body's inertia to gravitational force and the above relation is usually used for shallow water waves for example, tidal waves. In fluid dynamics, Froude number represents subcritical flow when less than one and supercritical flow above one thus it is analogous to Mach number.

The second term on the right hand side of Equation 2.3, accounts for the gravity term $\left(\frac{1}{Fr^2}\right)g$ which has units of m/s^2 and $\left(\frac{\rho_a}{\rho}\right)\left(\frac{1}{Fr^2}\right)g$ takes care of buoyancy effects. The first term represents the drag force exerted on the droplets by air.

A significant parameter that controls the ice accretion process is the local collection efficiency, β . This parameter is defined as the ratio of the amount of water droplets impinging the interested surface, ds compared to the amount of water droplets passing through the plane upstream, dy_0 of the impinging surface. An illustration of local collection efficiency is represented in Figure 13, and total collection efficiency is obtained by integrating the local collection efficiencies [17].

$$\beta = \frac{dy_0}{ds} \quad \text{EQUATION 2.8}$$

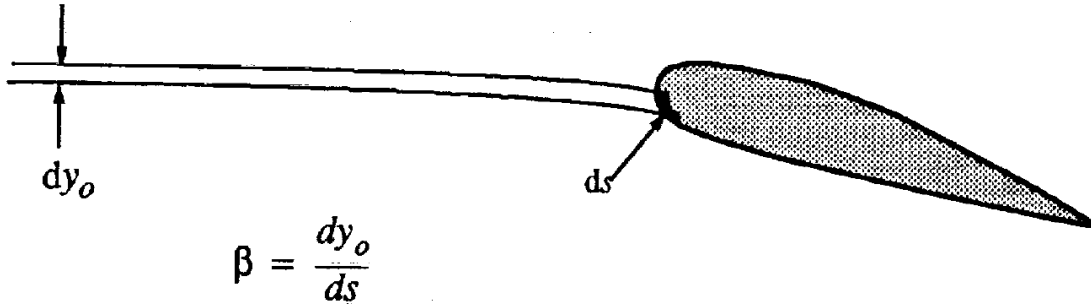
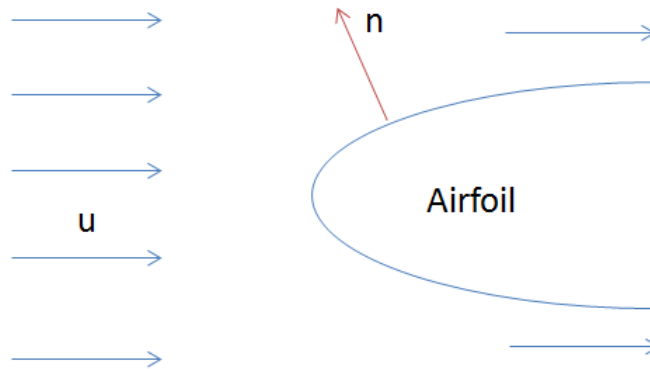


FIGURE 13: DEFINITION OF LOCAL COLLECTION EFFICIENCY [17]

Local collection efficiency can also be calculated as normalized flux of water droplets on a surface. Using the droplet solution which produces α and u on the entire solution domain, β can be calculated as;

$$\beta = -\alpha u \cdot n \quad \text{EQUATION 2.9}$$

Where n is the surface normal to the computational domain at mesh points on solid boundaries [15].



2.4.2 MASS AND ENERGY BALANCE FOR ICE ACCRETION

The icing accretion module in FENSAP-ICE uses a thin water film (of the order of tens of microns) model of thickness h_f , which extracts relevant inputs from air and droplet solution.

This water film analysis is based upon the Messinger model energy balance extended for aircraft icing as discussed in Reference 20. The impinging local mass flow rate, \dot{m}_β is calculated from local collection efficiency obtained from the droplet solution. For the implementation of thin water film model for mass and energy balance, certain assumptions need to be considered. The water film model is considered fully developed and the run back water is considered uniform in and out of the domain. The breakup of water film into rivulets and splashing and bouncing of impinging water droplets are neglected. The water film viscous terms dominate over the inertia terms and thus it is neglected. The impact velocity of the impinging droplet is assumed to be the freestream velocity and is used to calculate the kinetic energy of the impinging droplets. The water film in the control volume is assumed to have the temperature of the solid surface due to the very small thickness of water film. The shear stress of the water film does not alter the airstream as the mean velocity of the water film is negligibly small compared to the freestream velocity and the value of wall shear stress calculated by the flow solution is assumed equal at air and water film interface as well [19].

As the water film thickness under the consideration for anti-icing cases are never above $10\mu\text{m}$, higher order terms in the velocity profiles are negligible and a linear water film velocity profile can be used with no slip condition applied to the surface walls as given in Equation 2.10 [21].

$$u_f(x, y) = \frac{y}{\mu_w} \tau_w(x, y) \quad \text{EQUATION 2.10}$$

Where the water film velocity is denoted as $u_f(x, y)$ can be seen in Figure 14; $\tau_w(x, y)$ is the air wall shear stress tensor; μ_w is the dynamic viscosity of water and y is the coordinate normal to

the wall as seen in Figure 14. The shear stress is the major force exerted on the water film as the pressure gradient and gravity can be ignored except for the stagnation point (Reference 21).

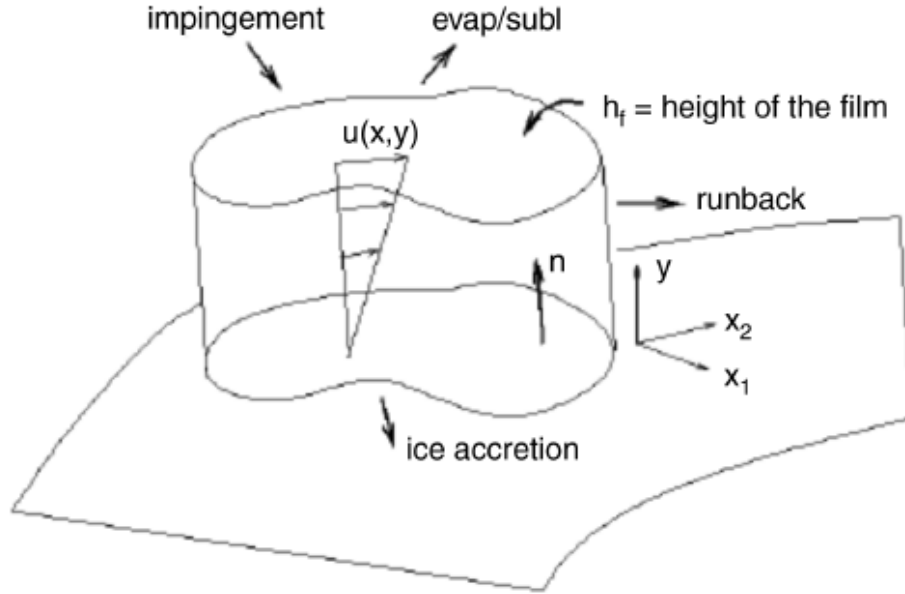


FIGURE 14: WATER FILM LAYER MODEL USED IN ICE3D [18]

A mean water film velocity, $\bar{u}(x, y)$ can be obtained by integrating along the thickness of water film, h_f ;

$$\bar{u}(x, y) = \frac{1}{h_f} \int_0^{h_f} u_f(x, y) dy = \frac{h_f}{2\mu_w} \tau_w(x) \quad \text{EQUATION 2.11}$$

Thus, the mass conservation equation can be written using Figure 15 (Left) as the mass flow rate of water run back in and out of control volume is assumed uniform:

$$\dot{m}_{in} = \dot{m}_{\beta} = \dot{m}_{evap} + \dot{m}_{ice} = \dot{m}_{out} \quad \text{EQUATION 2.12}$$

Where \dot{m}_{evap} is the mass flow rate leaving the control volume due to evaporation; \dot{m}_{ice} is the mass flow rate leaving the control volume due to ice accretion and \dot{m}_β is the incoming mass flow rate from impinging water droplets which is proportional to the collection efficiency, β .

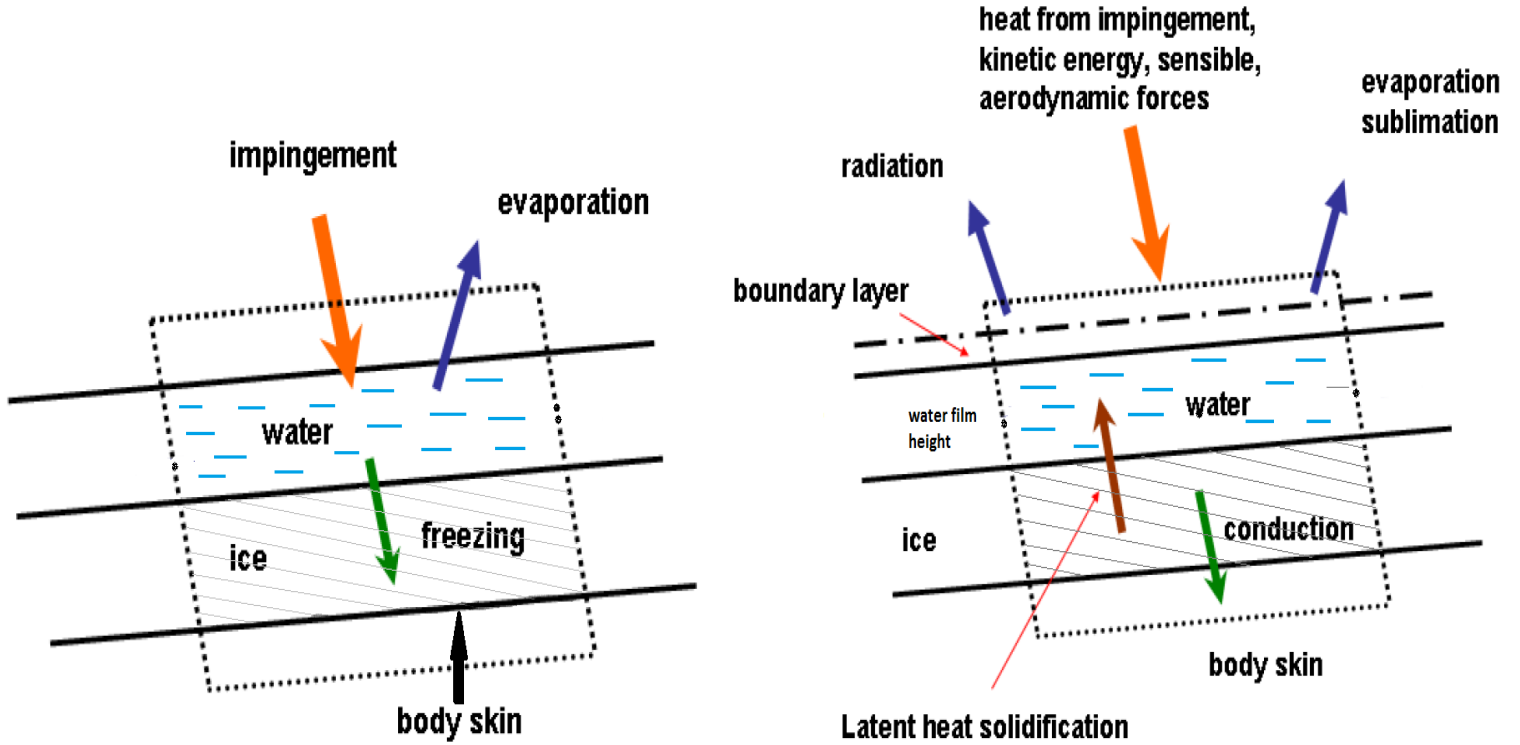


FIGURE 15: MASS BALANCE (LEFT) AND ENERGY BALANCE (RIGHT) IN A CONTROL VOLUME [4]

Using Figure 15, the energy balance using typical Messinger model can be written as [4],

$$\dot{Q}_{evap} + \dot{Q}_{conv} + \dot{Q}_{fus} + \dot{Q}_{ice} - \dot{Q}_{Rad} - \dot{Q}_\beta - \dot{Q}_{kin} = 0 \quad \text{EQUATION 2.13}$$

The above equation represents energy balance within the control volume for energies lost and gained due to different heat fluxes. The heat fluxes representing energy losses are by evaporation or sublimation \dot{Q}_{evap} ; heat flux due to convection \dot{Q}_{conv} ; heat flux due to sensible and latent heat \dot{Q}_{fus} ; conduction through the ice could add or remove heat \dot{Q}_{ice} . The energy gained are due to

radiative heat flux \dot{Q}_{Rad} , kinetic energy gained by the droplets from free stream \dot{Q}_{kin} and due to the impinging droplets \dot{Q}_β .

The above mass and energy conservation expressed in partial differential equations is as follows;

$$\rho_w \left[\frac{\partial h_f}{\partial t} + \nabla \cdot (\bar{\mathbf{u}} h_f) \right] = U_\infty (LWC) \beta - \dot{m}_{evap} - \dot{m}_{ice} \quad \text{EQUATION 2.14}$$

$$\rho_w \left[\frac{\partial h_f C_w \tilde{T}}{\partial t} + \nabla \cdot (\bar{\mathbf{u}} h_f C_w \tilde{T}) \right] = \left[C_w \tilde{T}_{d,\infty} + \frac{\|\mathbf{u}_d\|^2}{2} \right] \times U_\infty LWC \beta \quad \text{EQUATION 2.15}$$

$$-0.5(L_{evap} + L_{subl})\dot{m}_{evap} + (L_{fusion} - C_{ice}\tilde{T})\dot{m}_{ice} + \epsilon\sigma(T_\infty^4 - T^4) + \dot{Q}_h$$

In Equation 2.14, the terms on the right hand side represent the mass transfer by the source of water film (impinging droplets), the evaporation and the ice accretion respectively.

In Equation 2.15, the first term corresponds to the heat transfer due to the impinging droplets where ρ_w is the density of water; C_w is the specific heat for water; \tilde{T} is the temperature at wall/air/liquid-water/ice interface in °C; $\tilde{T}_{d,\infty}$ is the temperature of the water droplet at infinity in °C; \mathbf{u}_d is the droplet velocity. The second term corresponds to the heat transfer due to evaporation where L_{evap} is the latent heat of vaporization/evaporation; L_{subl} is the latent heat of sublimation. The third term represents heat transfer due to ice accretion where L_{fusion} is the latent heat of fusion at 0°C; C_{ice} is the specific heat for ice. The fourth terms corresponds to the radiative heat transfer where ϵ is the emissivity of the solid; σ is the Boltzmann Constant and equals $1.381e^{-23} \frac{m^2 kg}{s^2 K}$; T_∞ is the temperature at infinity in Kelvin; T is the temperature at wall/air/liquid-water/ice interface in Kelvin. And the last term is for the convective heat transfer. In anti-icing simulation the heat loss through radiation is a key parameter and during an evaporation process half the water is considered liquid while the other half remains solid [21].

The flow solver calculates the convective heat transfer term from Equation 2.15, \dot{Q}_h which before the ice accretion process is used to find heat transfer coefficient, h ;

$$h = \frac{\dot{Q}_h}{(T - T_\infty)} \quad \text{EQUATION 2.16}$$

This heat transfer coefficient, h will change drastically depending on the boundary layer thickness but is not very dependent on the surface temperature distribution. Thus, between every iteration of the flow solver, Equation 2.15, a constant value of $h(x)$ is chosen in order to obtain a convective heat flux.

2.4.3 CONJUGATE HEAT TRANSFER FOR ANTI-ICING

The conjugate heat transfer module is used for deicing/anti-icing simulations by iteratively matching the total heat flux between the solid and fluid domain and through any initial accreted ice. This gives more realistic results for the heat flux because the wall boundary conditions in flow solver calculations have to set to specified values which may change due to ice accretion. In order to run CHT3D an initial solution for the flow droplet and ice accretion is needed. A solid domain representing the heat conducting surface is also required, as well as defining the interface between the solid domain and the fluid domain. The iterative process within CHT3D consists of six steps within all iterations.

The first step is to solve the Navier-Stokes equations using a flow solver with Dirichlet boundary conditions at the specified interfaces. The next step is to evaluate the surface heat fluxes at these interfaces due to the Dirichlet boundary conditions from previous step. The third step solves Poisson Heat Conduction equations in the solid domain with Neumann boundary conditions. The surface temperature at the fluid-solid interface is then evaluated based upon the

heat conduction solution obtained from the previous step. The final step is to update the Dirichlet boundary conditions at the interfaces in the flow solution in step one by using a relaxation factor [22].

2.5 SYNTHETIC JET ACTUATOR

The current work employs CFD analysis to examine a new method of efficient icing control using an array of thermally activated synthetic jet actuators (SJAs) distributed on the surface exposed to ice accretion. SJA is a zero-net mass flux (ZNMF) device that is able to produce a time-averaged microjet of air (Fig.2) without using an external supply of net air mass flow. It accomplishes this through an oscillating piezoelectric membrane (in most designs) situated inside a cavity [6]. The opposite side of this cavity has a small orifice where the air travels through. When the membrane oscillates downward, the air from the surroundings is pulled into the actuator's cavity. When the membrane oscillates upward, the air is pushed back outward with a certain amount of momentum that carries it away from the device. During the cycles of membrane oscillations, a stream of expelled convected vortices under certain optimal conditions may form a jet produced by the SJA. Note that the membrane oscillations are induced by an alternating current applied across the piezoelectric membrane which transfers electrical oscillations into mechanical oscillations. The important parameters of the actuator including the produced peak velocity of the jet are affected by variations in the actuator geometry and by the amplitude and frequency of the diaphragms' oscillations.

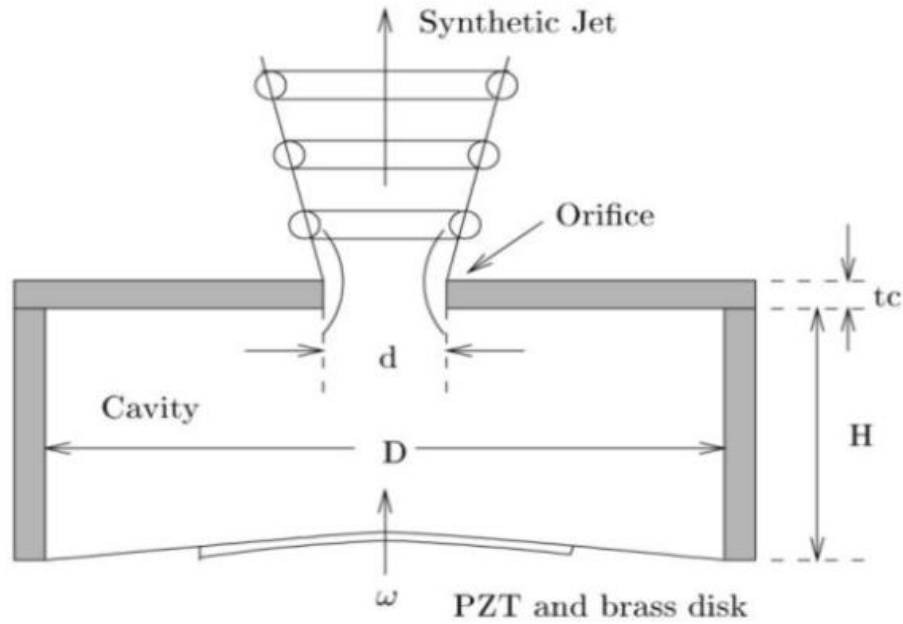


FIGURE 16: SCHEMATIC OF A SYNTHETIC JET ACTUATOR [25]

Much work has been done in the past to investigate SJA effectiveness for unsteady flow control. In particular, our previous numerical study [8] investigated using SJAs for active control of unsteady flow over a low-speed airfoil in the presence of a sharp-edge gust. In the numerical procedure, the actuator's dimensional scaling and excitation frequency effects were examined for a specific SJA configuration using a low-fidelity model employed in conjunction with RANS analysis to determine a simple fluctuating-velocity boundary condition at the bottom of the actuator's orifice. The same method based on embedding only SJA orifice in the surface exposed to an upstream super-cooled flow and using a prescribed time-dependent velocity at the bottom of the orifice is used in the current study. Note that such approach greatly enhances computational efficiency by excluding the full actuator cavity from the analysis while allowing for the expelled jet to freely interact with the grazing external flow.

CHAPTER 3: METHODOLOGY/APPROACH

FENSAP-ICE is a complete ice accretion package that includes a Reynolds Averaged Navier-Stokes (RANS) based flow solver, a droplet impingement solver, an ice accretion and water runback solver and a heat conduction solver. Each of the solver modules is able to interface directly with each other to pass the results from one to the other in a seamless manner. A complete icing analysis begins with calculating the flow solution using the FENSAP flow solver with input grid generated using various grid creation software. The result from the flow solver is then used by DROP3D to calculate droplet impingement on the surfaces of interest. Both the flow solution and the droplet impingement solution are then used by ICE3D to calculate the water runback, ice accretion, and heat fluxes due to this process on the surface. CHT3D then uses the results from all three modules as initial conditions for the iterative process to calculate the total heat flux due to the anti-icing system. Finally, ICE3D is used again with the final heat flux solutions to calculate ice accretion on the surfaces of interest under the influence of the anti-ice system. This process is summarized in the flow chart in Figure 17.

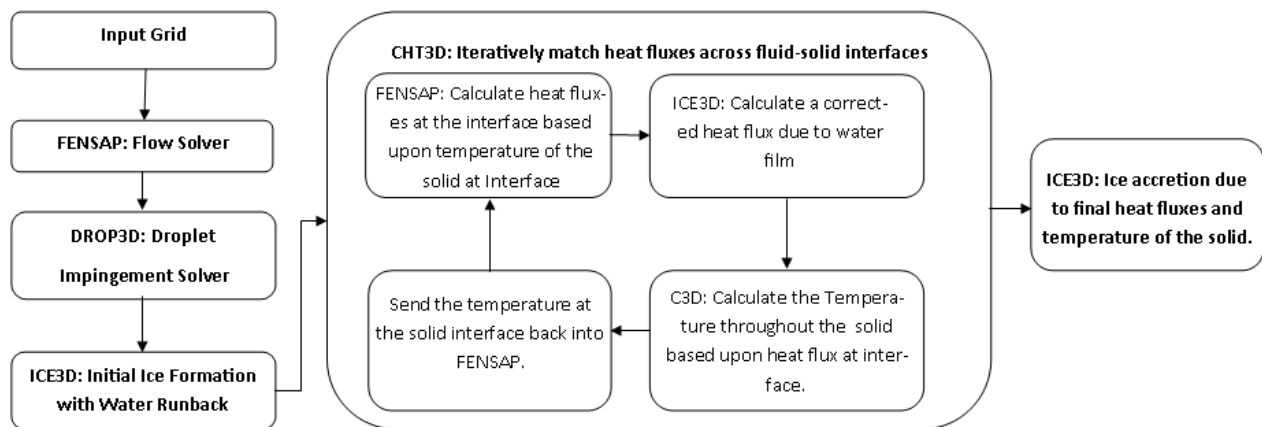


FIGURE 17: FENSAP-ICE PROCEDURE

3.1 TEST STUDY CASES: WEDGE IN SUPERCOOLED FLOW

The effect of employing an array of six heated or non-heated actuated jets to prevent and/or reduce ice accretion is examined for a 15° wedge of length $L=54\text{mm}$ in a super-cooled flow with upstream Mach number $M=0.1$ (Figure 18). The wedge configuration is chosen as a benchmark for this study because of its simplicity while at the same time satisfying necessary requirements for ice accretion as well as due to FENSAP-ICE academic license restrictions.

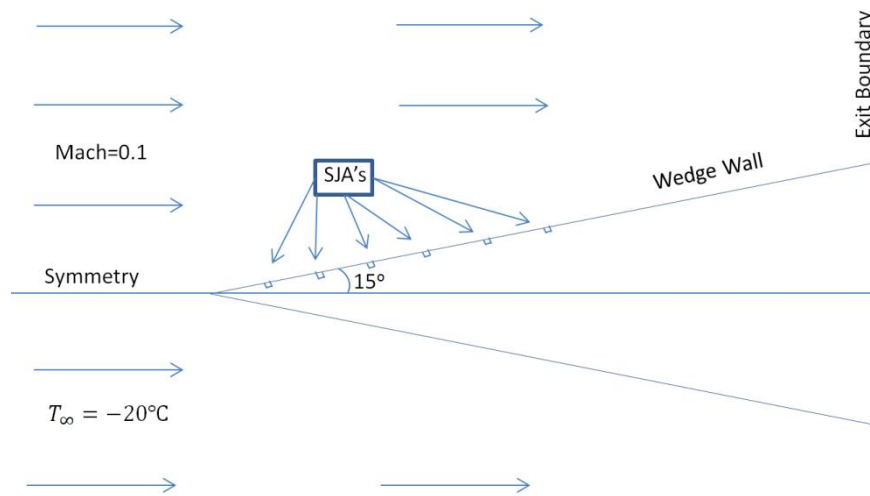


FIGURE 18: TEST CASE DIAGRAM

Furthermore, the same SJA geometry and parameters previously investigated in the airfoil unsteady flow control study of Reference [26] is considered in the current work. In particular, the prescribed amplitudes of the jet velocities at the bottoms of the actuators' orifices are taken to be 25m/s produced by SJAs with orifice diameters and heights of 0.5mm and actuation frequencies of 1000Hz . The actuators are distributed 5mm apart along the wedge (Figure 19).

Four test cases are considered in the current study according to Table 3. For each case, the upstream supercooled flow is imposed with temperature $T=-20^\circ\text{C}$, and the formation of ice

shape and thickness is predicted at $t=10$ sec. Cases B has a heated SJA chamber with a prescribed temperature of 100°C . Case D contains several subcases for further parametric studies described later in this chapter and as such the SJA chamber has two prescribed temperatures of 100°C and 75°C .

	SJA Temperature ($^{\circ}\text{C}$)	SJA Inlet Velocity (m/s)
Case A: Baseline case	Freestream	0
Case B: Non-Actuated, Heated SJA	100	0
Case C: Actuated, Non-Heated SJA	Freestream	$25\sin(2\pi ft)$
Case D: Actuated, Heated SJA	75,100	$25\sin(2\pi ft)$

TABLE 3: SUMMARY OF CASES

3.2 NUMERICAL IMPLEMENTATION: GRID SPECIFICATIONS

The grid employed in this study (Figure 19) is generated using Pointwise software with 244,336 grid points to satisfy the FENSAP-ICE academic license restrictions. An airfoil shape was not analyzed in this study due to the node limitations in the licence. In the FENSAP solver simulations, the inlet boundary condition is imposed at the upstream surface while the exit boundary conditions are imposed at the top and downstream surfaces of the computational domain. The symmetry condition is imposed at the bottom of the domain upstream of the wedge, and the wall boundary condition is imposed along the wedge itself. The SJA orifices are considered as wall boundaries on the sides and inlet boundaries on the bottoms. In all cases, the FENSAP solutions employed by FENSAP-ICE are obtained at $t=0.15$ sec after 3,000 iterations (with a time step of $5e-5$ sec). The flow simulations are implemented using Spalart-Allmaras turbulence model.

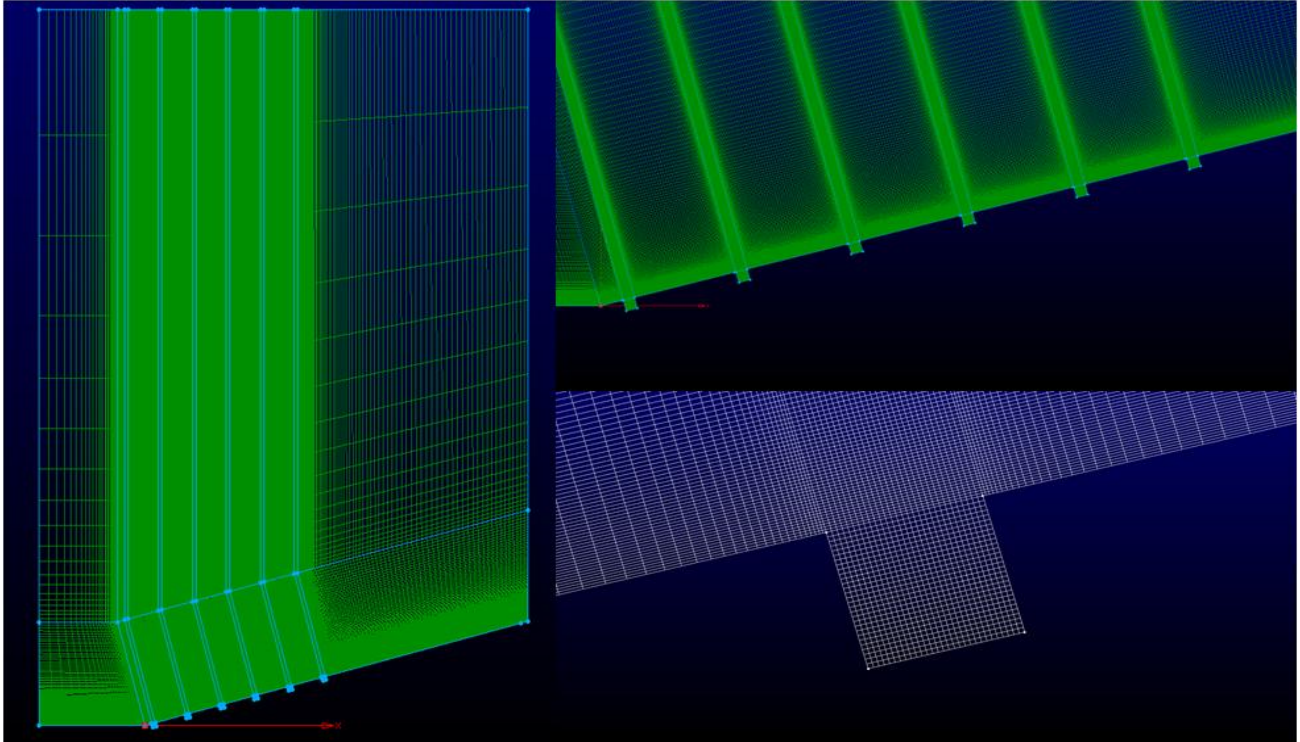


FIGURE 19: GRID DESIGNED FOR A WEDGE WITH A SERIES OF SIX SJAS (LEFT); CLOSE-UP VIEW OF SJA REGION (RIGHT)

The front of the wedge before the first SJA orifice is defined in ICE3D as a water sink to avoid water buildup inside the domain. The grid for the heat-conducting solid domain (Figure 20) is created in Pointwise with 29,700 points to implement an interface for CHT3D solver. In the CHT3D analysis, an adiabatic boundary condition (zero heat flux) is imposed at the front, back and bottom boundaries of the solid domain, while the sides have a symmetry boundary condition. Furthermore, the walls of the wedge and the SJAs are defined as interfaces with the fluid grid. CHT3D thus matches the heat flux between the fluid and solid domains at these interfaces in an iterative process to ensure the ice formation dependence on the flow conditions.

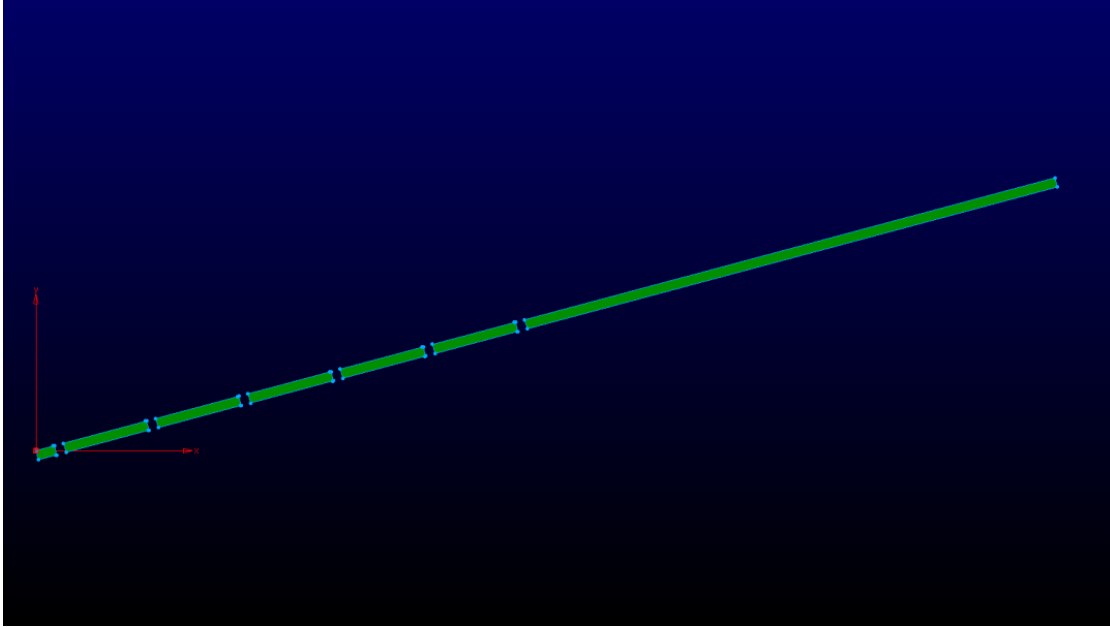


FIGURE 20: GRID FOR THE SOLID DOMAIN

3.3 PROCEDURE OF ANALYSIS: TRANSIENT FLOW WITH SS CHT3D

The CHT3D module within FENSAP-ICE currently cannot perform a fully unsteady anti-icing analysis with a transient flow solution. CHT3D uses an iterative process that matches the heat flux between a fluid domain and a solid domain and as such requires a flow solution that does not change during this process. Synthetic Jet Actuators require a transient flow solution due to the dependence of the jet velocity in time so a quasi-steady analysis method is used to study the anti-icing effectiveness of the SJA's. This method takes several snapshots in time throughout one cycle of the SJA orifice velocity as shown in Table 4.

	Time (s)	SJA Inlet Velocity (m/s)
Snapshot 1	0.015	0
Snapshot 2	0.01525	25
Snapshot 3	0.0155	0
Snapshot 4	0.01575	-25

TABLE 4: TIME SNAPSHOTS FOR QUASI STEADY ANALYSIS

The first snapshot is taken at the 3000th iteration at a time of 0.015 seconds when the velocity at the orifice is at 0m/s between the last suction phase and the next ejecting phase. The second snapshot is fifty iterations later at t=0.01525 seconds when the SJA is fully ejecting with a velocity of 25m/s. The third snapshot is again fifty iterations later at t=0.0155 seconds after the ejection phase but before the suction phase when the orifice velocity is at 0m/s. The last snapshot is another fifty iterations later at t=0.01575 seconds when the orifice is fully in the suction phase at a velocity of -25m/s. The plot in Figure 21 shows the position of the time snapshots graphically in relations to the SJA orifice velocity.

The locations of the time snapshots are at the extremes of velocity in the SJA cycle and allow for the analysis to find the maximum and minimum amount of ice accretion due to the orifice velocity. This method would only be used in Cases C and D due to the time dependence of the actuation. Cases A and B do not have a time dependent SJA actuation velocity and only need to be analyzed at one time snapshot.

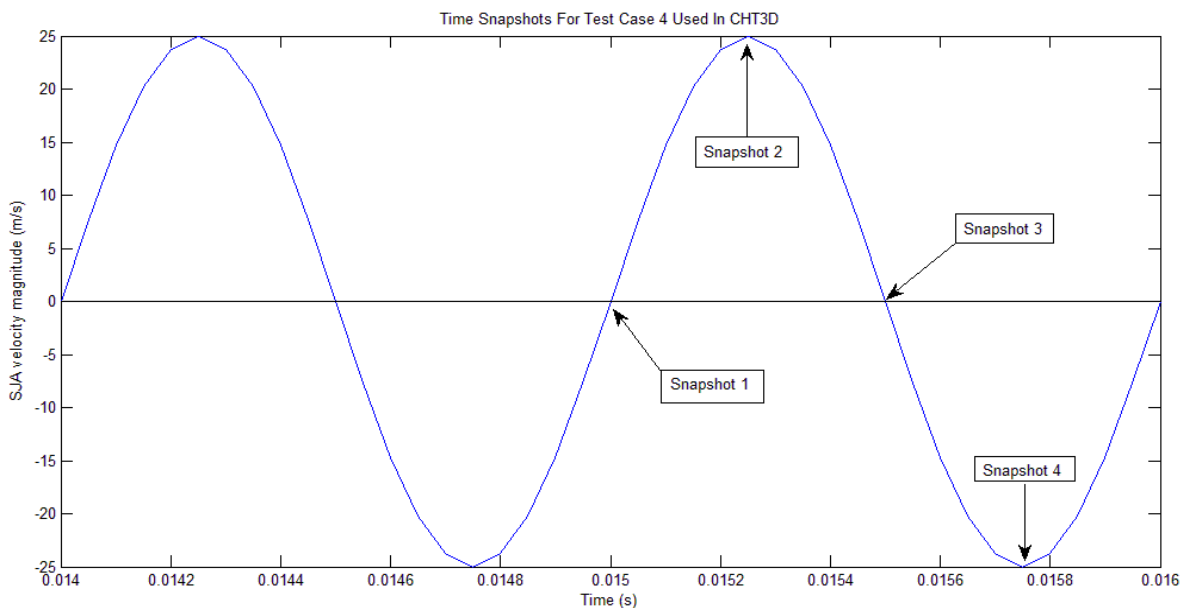


FIGURE 21: GRAPHICAL REPRESENTATION OF TIME SNAPSHOTS

3.4 CASE D PARAMETRIC STUDIES

In addition to the case studies outlined in section 3.1, several parametric studies for the actuated and heated case are performed for different parameters and the difference in the total ice accretion on the surface of the wedge will be compared. Each sub-case will use snapshots two and four as outlined above with the ice accretion comparisons performed each. These studies will examine the effect of SJA inlet temperature, droplet distribution, droplet size and freestream temperature on the ice accumulation on the wedge wall. The different parameters for the parametric study are summarized in Table 5.

Case D Parametric Studies			
SJA Inlet Temperature (°C)	Droplet distribution type	MVD (microns)	Freestream Temperature (°C)
75	Monodisperse	20	-20
75	Langmuir-D	20	-20
100	Langmuir-D	20	-20
100	Langmuir-D	100	-20
100	Langmuir-D	20	-10

TABLE 5: PARAMETRIC CASES RUN FOR CASE D

The first parameter for study is the droplet distribution type in which the Monodisperse and the Langmuir-D droplet distributions will be compared. The Monodisperse droplet distribution is one in which all droplets are of the same size, 20 microns in diameter for this case. The Langmuir-D droplet distribution has droplets of varying diameters with a statistical weighting centered on a specified diameter of 20 microns for the comparison. This distribution is a more realistic spectrum of droplet sizes found in clouds at icing altitudes. Very small droplet sizes can be carried by the flow more easily compared to larger droplets so that the larger droplets in the Langmuir-D distribution may induce more ice accretion by more effectively hitting the wedge surface. The weighting function for this distribution centered on 20 microns is shown in Figure 22 (Left). A SJA inlet temperature of 75°C was chosen for this study because a

higher temperature can evaporate the small droplets before they hit the icing surface thereby invalidating the comparison.

The second parameter for study is the SJA inlet temperature for 75°C and 100°C. At 100°C the flow from the SJA's will evaporate smaller droplets completely before they have a chance to impinge on the surface and freeze. The 75°C temperature is not hot enough to completely evaporate the impinging droplets so more ice accretion may occur along the unprotected areas of the surface. This can also cause more water runback by melting impinging ice particles that would otherwise impact the surface and bounce away from the surface. Therefore ice accretion for these SJA temperatures will be compared. The Langmuir-D distribution centered at 20 microns is chosen so that larger droplet sizes up to 40microns are included in the flow.

The next comparison will be between Supercooled Small Droplets and Supercooled Large Droplets. This comparison will be performed at a SJA temperature of 100°C using a Langmuir-D distribution so that the effect of droplet evaporation and water runback from the larger droplets on ice accretion can be studied. The distributions for both SSD and SLD are shown in Figure 22.

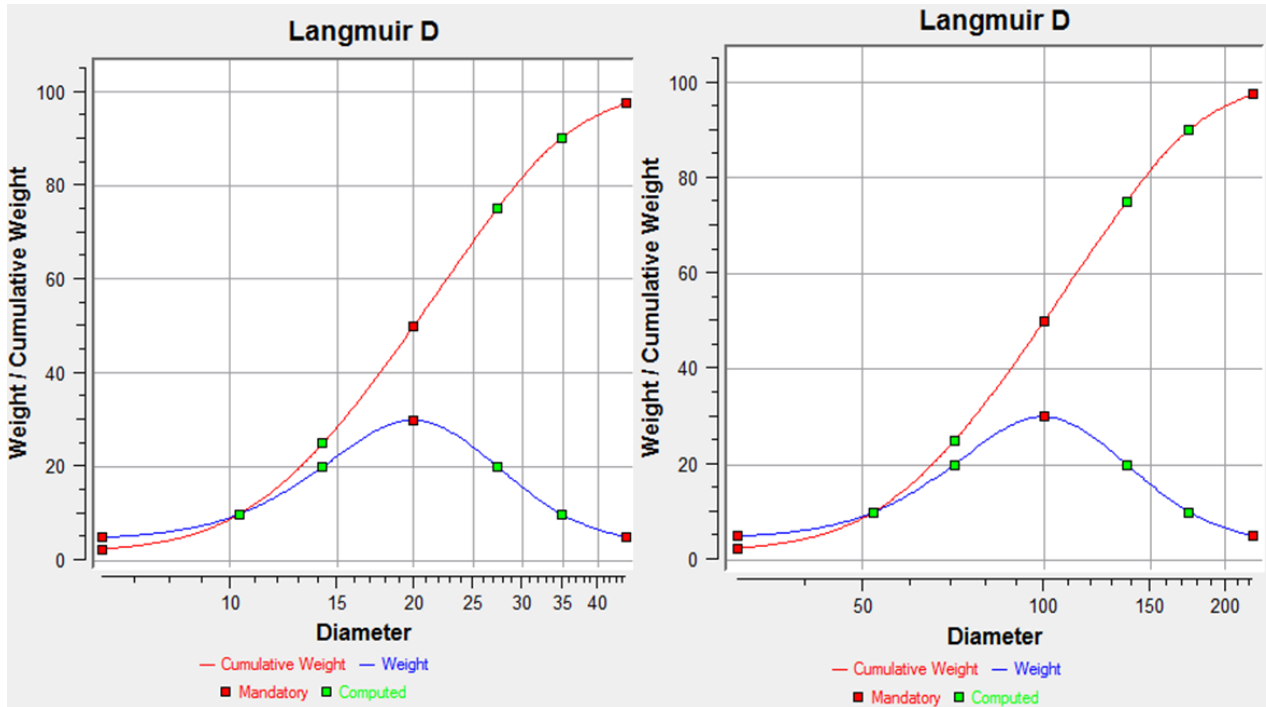


FIGURE 22: SSD LANGMUIR-D DISTRIBUTION (LEFT) AND SLD LANGMUIR-D DISTRIBUTION (RIGHT)

The last parameter to study is the effect of the freestream temperature on ice accumulation on the wedge using -20°C and -10°C . A higher freestream temperature will require less heat flux from the heated flow out of the SJA's to evaporate the droplets impinging on the surface thus allowing for more effective anti-icing. This will also allow for the effectiveness of this anti-icing method on both Rime and Glaze ice condition to be studied. A summary of each study and the parameters used is shown in Table 6.

	SJA Inlet Temperature (°C)	Droplet distribution type	MVD (microns)	Freestream Temperature (°C)
Parametric Study I: Droplet Distribution	75	Monodisperse	20	-20
	75	Langmuir-D	20	-20
Parametric Study II: SJA Inlet Temperature Variation	75	Langmuir-D	20	-20
	100	Langmuir-D	20	-20
Parametric Study III: SSD and SLD	100	Langmuir-D	20	-20
	100	Langmuir-D	100	-20
Parametric Study IV: Freestream Temperature Variation	100	Langmuir-D	20	-20
	100	Langmuir-D	20	-10

TABLE 6: CASE D PARAMETRIC STUDY SUMMARY

3.5 MISCELLANEOUS PROGRAM INPUTS

A major advantage of the FENSAP-ICE software package is that the flow solver can be replaced by other commercially available CFD flow solvers such as FLUENT or CFX. The FENSAP flow solver was used for this project instead of any of these is due to the additional speed afforded by using the integrated solver. FENSAP-ICE has the ability to run the droplet impingement solver simultaneously with the flow solver using the air and droplet coupled option which greatly reduces the computational time. There is also no need for a conversion of the flow solution from one CFD solver format to FENSAP-ICE's format.

ICE3D contains options to model both glaze ice and rime ice formations separately under any conditions. The module also has the ability to let the conditions of the flow determine what type of ice is formed under the Glaze-Advanced option. This study varies several different parameters which can affect the type ice formed on the surface of the wedge so this glaze-advanced option was used to account for a possible rime and glaze ice mixture. The Hot Air Chamber option is also used in the ICE3D calculation. This option provides a better estimation

of the heat transfer coefficients and evaporation quantities due to secondary inlets injecting hot air into the freestream flow.

The solid grid for the CHT3D module is assumed to be made of duralumin. The density is $2787 \frac{kg}{m^3}$, the conductivity is $164 \frac{W}{Km}$, and the enthalpy is taken to be $241060 \frac{J}{kg}$. These values were taken from the FENSAP-ICE tutorial. The interface boundary condition in CHT3D between the solid and fluid grids is located at the walls of the wedge and the SJA orifice walls. This interface is where CT3D calculates the heat flux between the solid and fluid grids.

CHAPTER 4: CASE STUDY RESULTS

A total of four cases for studying the effects on ice accretion with embedded SJA's on a 15° wedge in a Mach 0.1 flow are analyzed with two separate parameters are considered here, the SJA actuation and the SJA chamber temperature. Each cases flow properties and resultant ice accretion will be compared to gain insight into the effect that the heated, and actuated SJA's will have on the formation of ice.

4.1 CASE A: BASELINE

The baseline case has the SJA inlet velocity being zero and the SJA chamber temperature set to the freestream temperature. In this case the flow field acts as a simple wedge flow as seen in Figure 23. The pressure at the tip of the wedge is higher than the pressure downstream and is expected due to the stagnation point located at the wedge tip. The velocity flow field shows the flow increasing in speed as it moves along the wedge which matches with the pressure results in that a negative pressure gradient induces a positive velocity gradient. The close-up of the velocity field in the SJA orifice shows slight vortices forming due to the velocity shear between the flow over the wedge and the orifice opening. The flow field temperature is constant throughout the domain due to the lack of heat sources in this baseline case.

The Langmuir-D droplet distribution centered at a 20 micron MVD was used with a freestream temperature of -20°C . These types of conditions are inductive to rime ice formation which is characterized by a layer over the surface which follows the geometry. Figure 24 shows the total ice accretion after 10 seconds and matches the description of a rime ice formation. Note that the very front of the wedge surface does not have any ice due to the water sink condition imposed upon it to avoid numerical errors. The rounded bulges at the back corners of the SJA

orifices are due to the increased collection efficiency in that area due to the angle of the wedge with respect to the freestream flow field.

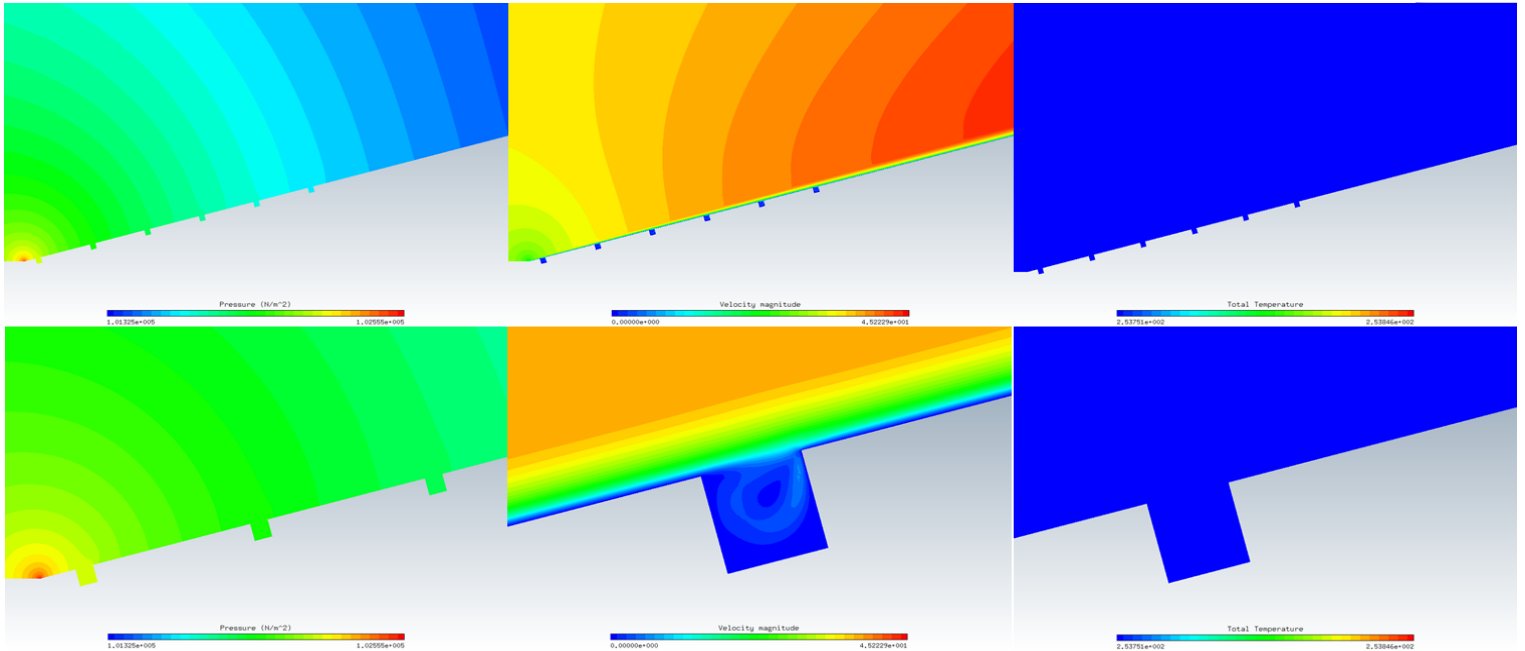


FIGURE 23: PRESSURE (LEFT), VELOCITY (MIDDLE) AND TEMPERATURE (RIGHT) CONTOURS. BOTTOM CONTOURS ARE CLOSEUPS.

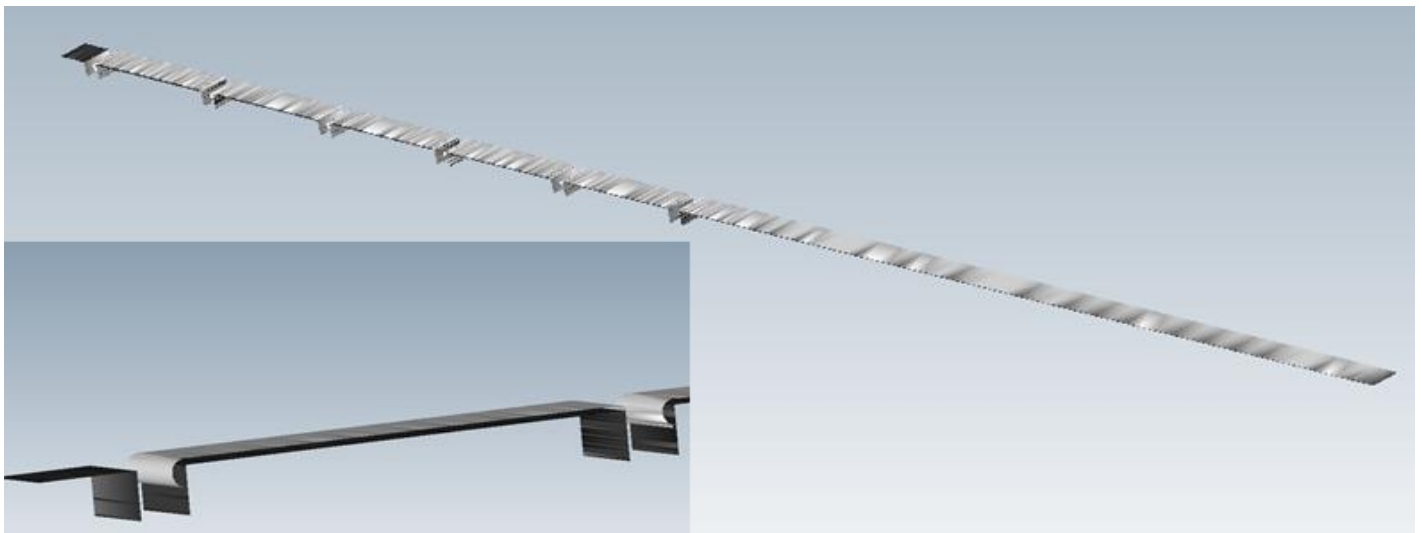


FIGURE 24: ICE ACCUMULATION. SMALLER PICTURE IS OF THE FRONT OF THE WEDGE.

The plot in Figure 25 shows the instant ice growth on the wedge during the ten seconds of ice accretion. The larger spikes in this plot are due to the bulges at the back corners of the SJA orifices. The total ice growth decreases along the wedge because of the growing boundary layer which pushes the smaller droplets away from the surface of the wedge thereby not allowing the droplets to impinge and freeze.

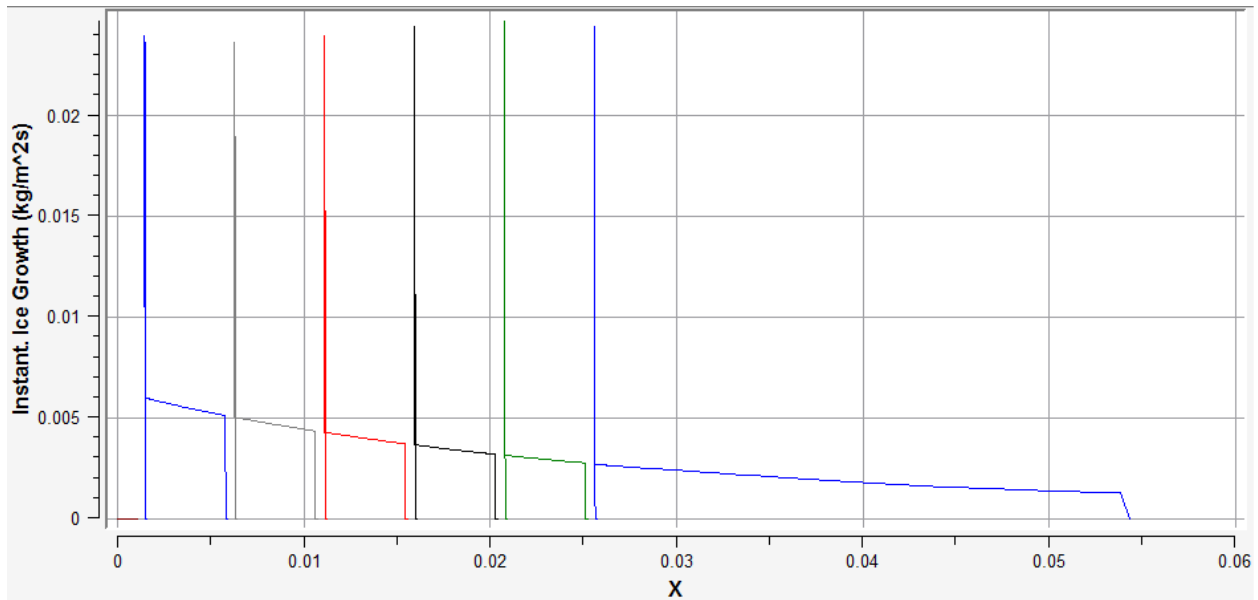


FIGURE 25: INSTANT ICE GROWTH PLOT

4.2 CASE B: NON-ACTUATED, HEATED SJA

For this case the SJA inlet velocity is still set to zero but the inlet temperature is at 100°C which simulates having a heated SJA chamber. This case also uses the Langmuir-D droplet distribution and a freestream temperature of -20°C. Figure 26 shows the pressure, velocity, and temperature contours of the flow field above the wedge. The pressure and velocity contours are the same as with the baseline case due to the lack of SJA actuation. The temperature contour shows a much higher temperature throughout the entire orifice section because of the heated SJA

chamber. There is also some higher temperature air over the surface of the wedge that is carried out of the orifice by the induced vortices.

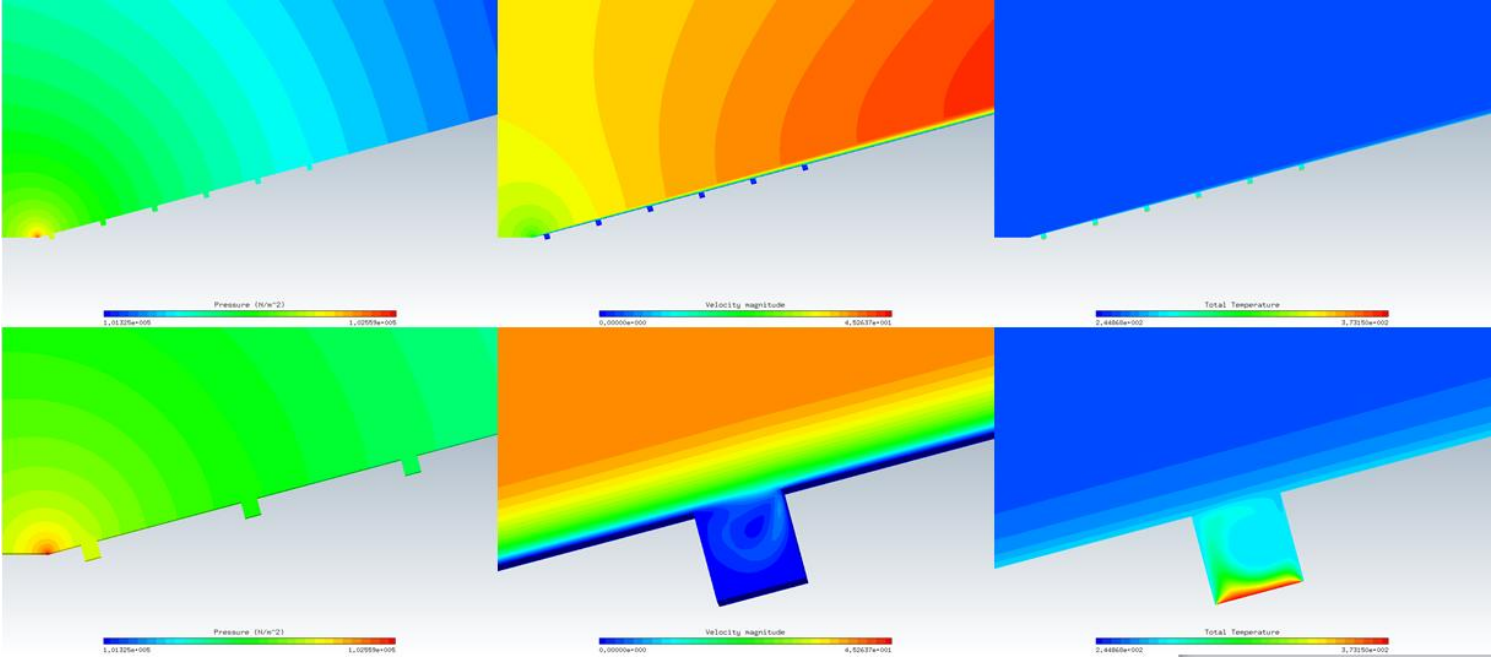


FIGURE 26: PRESSURE (LEFT), VELOCITY (MIDDLE) AND TEMPERATURE (RIGHT) CONTOURS. BOTTOM CONTOURS ARE CLOSEUPS

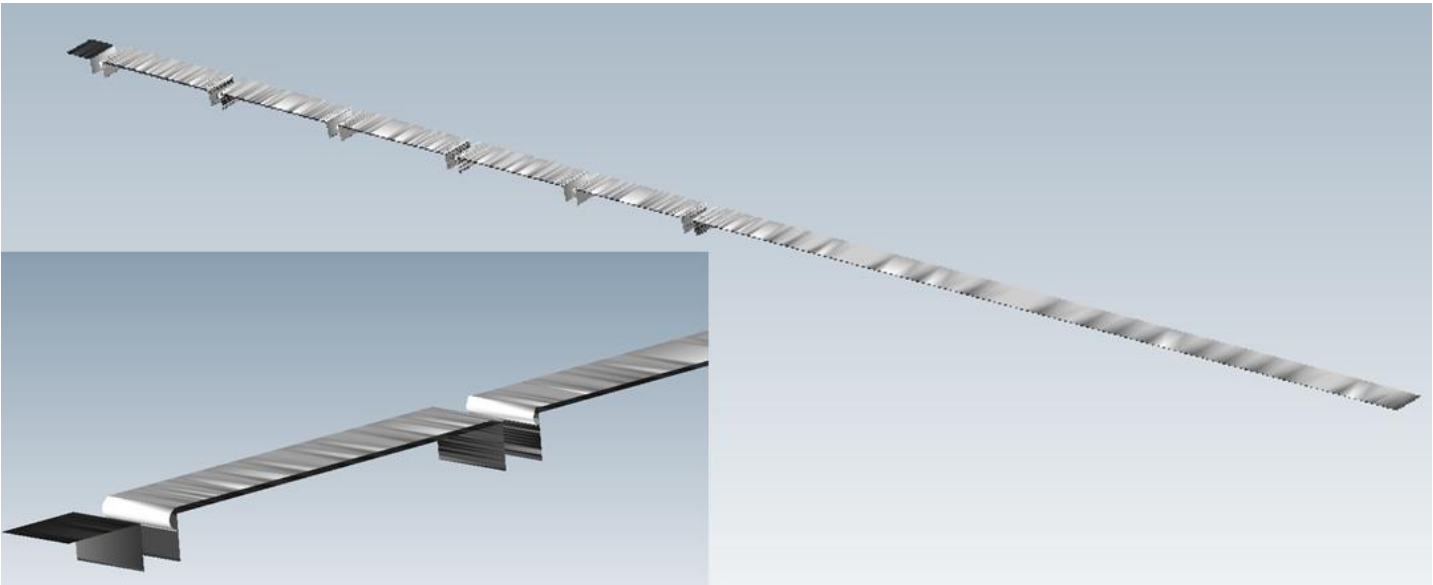


FIGURE 27: ICE ACCUMULATION. SMALLER PICTURE IS OF THE FRONT OF THE WEDGE.

The ice accretion for this case is shown in Figure 27 and is very similar to the baseline case with a layer of ice following the geometry of the wedge. While they are almost exactly the same on visual inspection, Figure 28 shows that the instant ice growth on the back corners of the SJA orifices are all less when compared to the baseline case. This can be explained by considering the temperature field inside the SJA orifice which is much higher than the freestream temperature. Even though there is not any actuation for this case the entire orifice is heated which acts to restrict ice growth in these regions. Conversely, the ice growth over the surface of the wedge is almost exactly the same as the baseline case because the heat from the SJA chamber is not directly ejected into the flow field over the wedge.

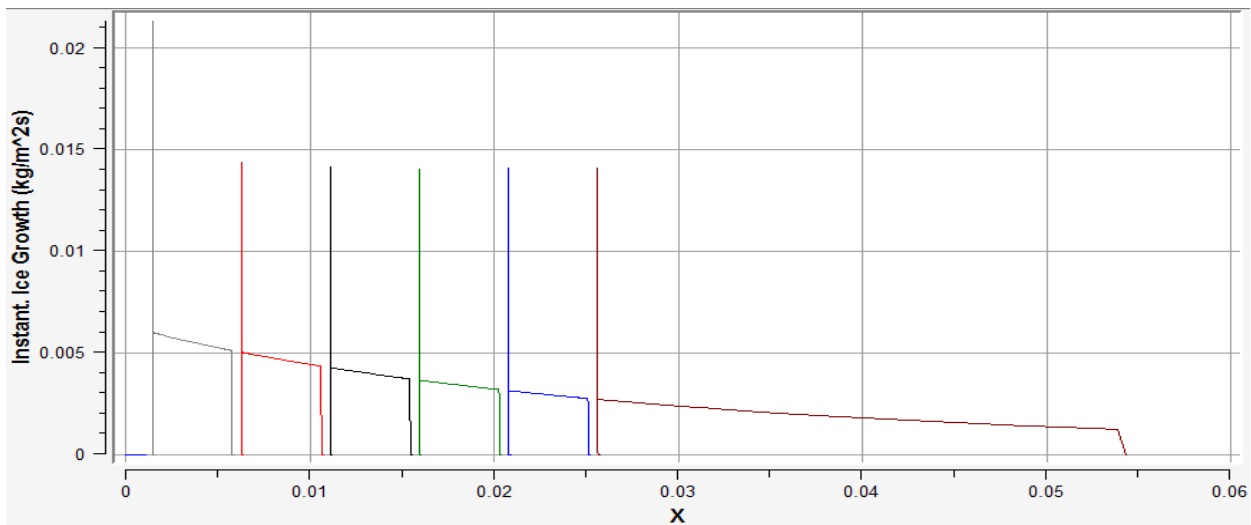


FIGURE 28: INSTANT ICE GROWTH PLOT

4.3 CASE C: ACTUATED, NON-HEATED SJA

Case C involves the time varying SJA inlet velocity without a heated SJA chamber. Figure 29 shows the pressure, velocity and temperature contours at the third time snapshot. This snapshot occurs when the SJA inlet velocity is zero after the ejection phase and before the suction phase. This snapshot was chosen because of the large modulation of the flow field at this

time. The actuation significantly modifies the flow field in both pressure and velocity while the temperature is still constant throughout the domain due to the lack of heat sources. The velocity contour shows several pockets of air next to the wall of the wedge which are due to the interaction of the freestream flow with the ejected air from the SJA orifice. These pockets can impede any incoming droplets away from the surface of the wedge by forcing the droplets to flow over and further back along the wedge thus reduce the amount of ice accretion. The pressure contours show the same higher pressure area at the tip of the wedge as in the previous cases but has lower pressure bubbles after each of the SJA's.

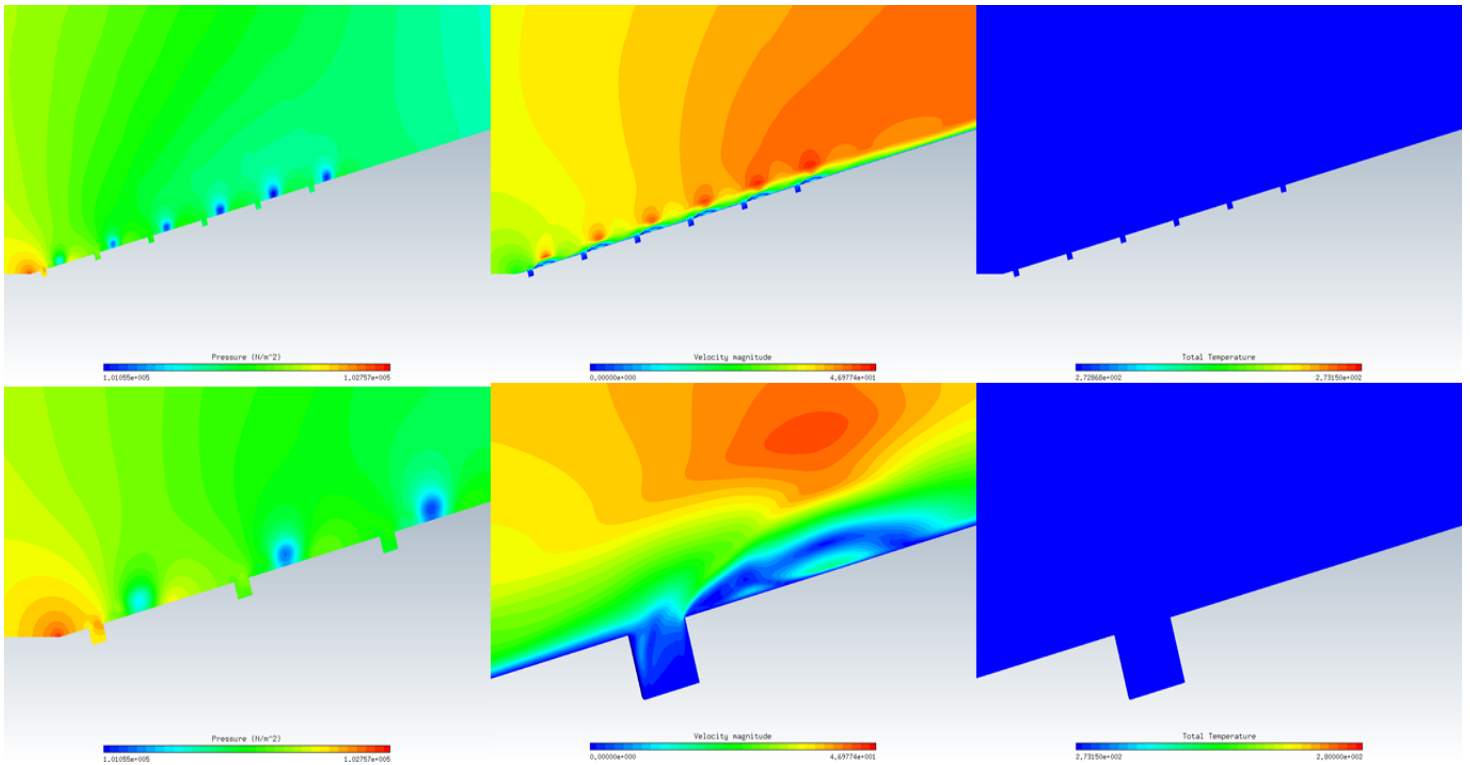


FIGURE 29: PRESSURE (LEFT), VELOCITY (MIDDLE) AND TEMPERATURE (RIGHT) CONTOURS. BOTTOM CONTOURS ARE CLOSEUPS

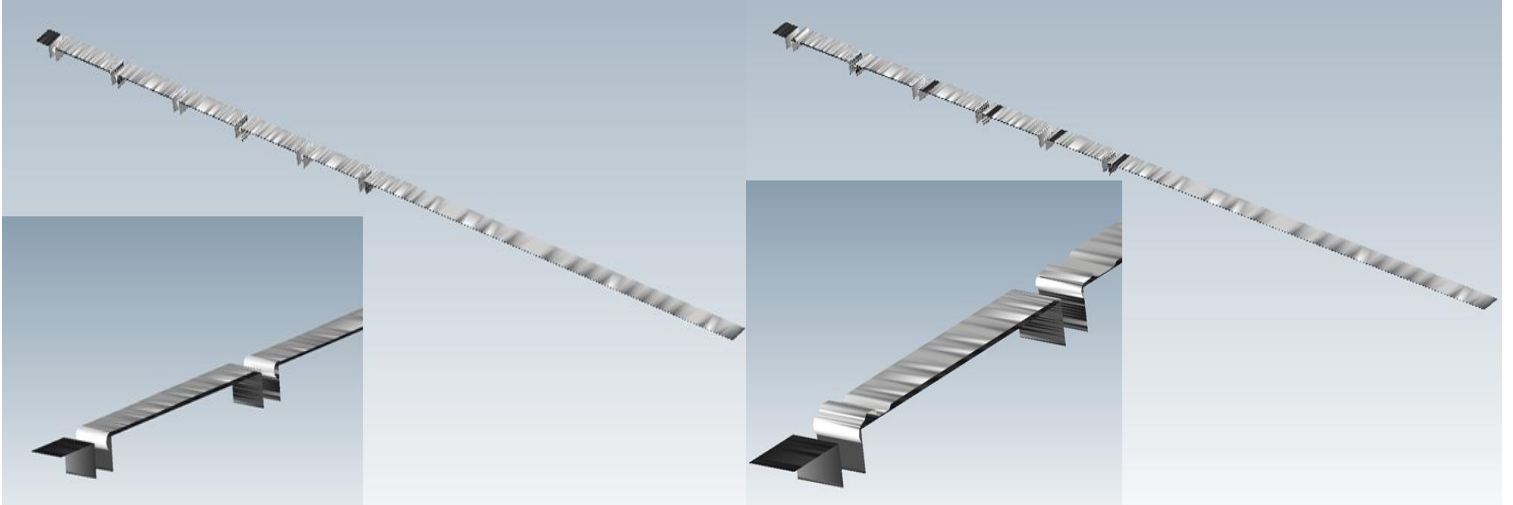


FIGURE 30: ICE ACCUMULATION. SMALLER PICTURE IS OF THE FRONT OF THE WEDGE. LANGMUIR-D DISTRIBUTION (LEFT) MONODISPERSE (RIGHT)

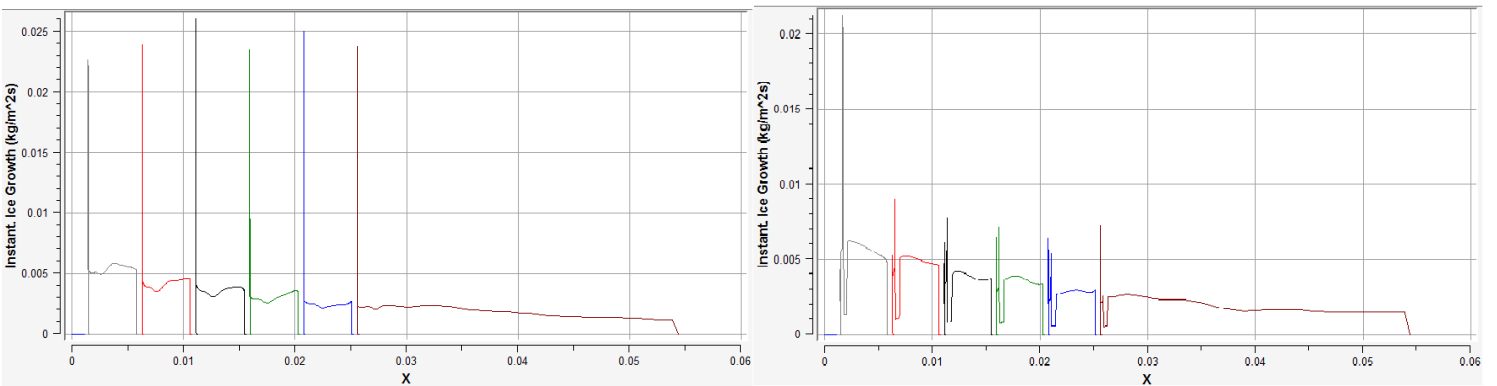


FIGURE 31: INSTANT ICE GROWTH PLOT. LANGMUIR-D DISTRIBUTION (LEFT) MONODISPERSE (RIGHT)

The ice accumulation (Figure 30) and the plot of instant ice growth (Figure 31) are shown for this case with both a Langmuir-D and a monodisperse droplet distribution. As seen in the figures, the monodisperse distribution exhibits a reduced amount of ice accretion due to the greater ease at which the smaller droplets are pushed away from the surface by the SJA actuation. The Langmuir-D droplet distribution contains some droplets that are smaller than 20microns and some droplets that are larger than 20microns. The SJA actuation is not as effective at keeping the larger droplets away from the wedge surface as it is for the smaller

droplets. Both examples show a decrease in ice accumulation along the wedge just after the SJA orifice when compared to the previous two cases.

4.4 CASE D: ACTUATED, HEATED SJA

This case will look at all four time snapshots because the heat that is ejecting from the SJA orifice will induce different amounts of heat flux between the freestream flow and the surface of the wedge. This requires a CHT3D analysis to be performed at each time snapshot due to the module only being able to implement a steady state analysis. Each snapshot is done with a Langmuir-D droplet distribution centered at 20microns, a SJA temperature of 100°C and a freestream temperature of -20°C.

4.4.1 SNAPSHOT 1

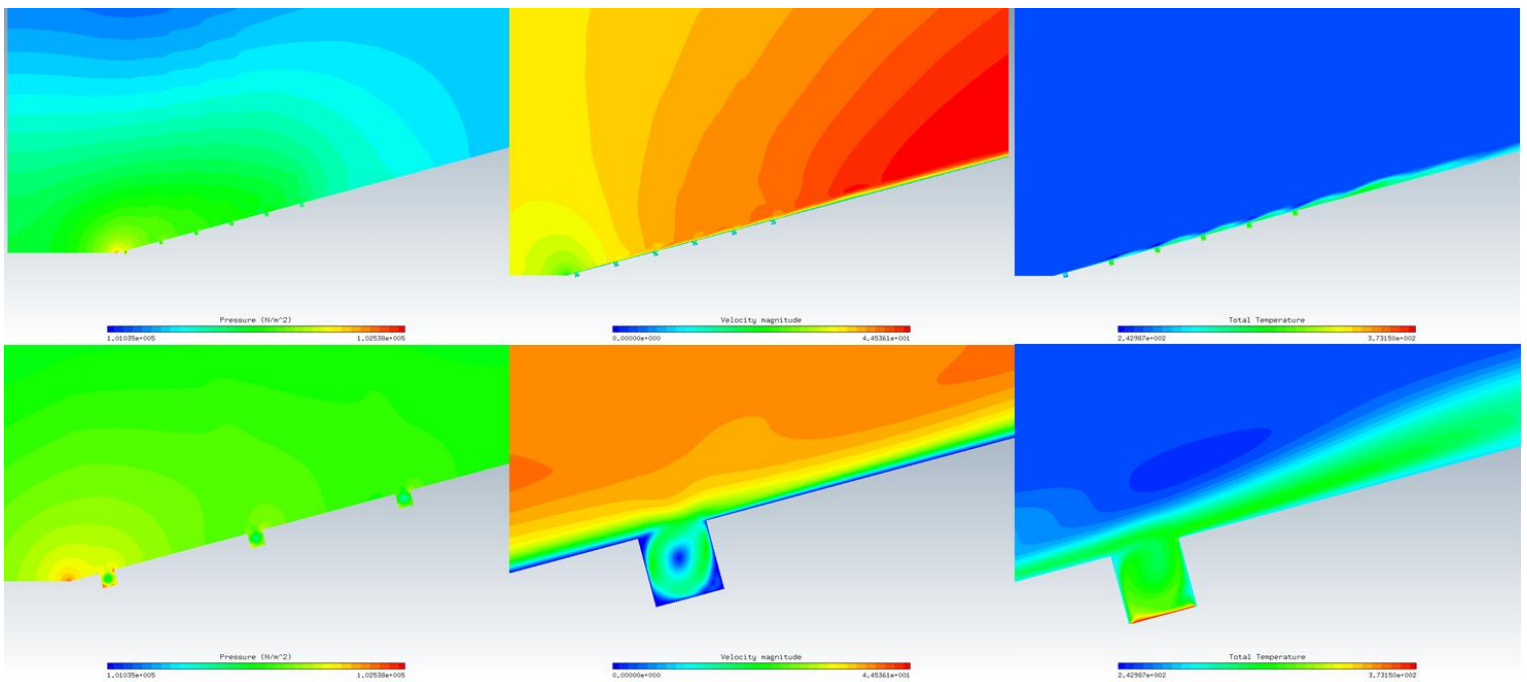


FIGURE 32: PRESSURE (LEFT), VELOCITY (MIDDLE) AND TEMPERATURE (RIGHT) CONTOURS.

BOTTOM CONTOURS ARE CLOSEUPS.

Snapshot 1 is the time at which the SJA inlet velocity is zero after the suction phase and before the ejection phase. Figure 32 shows the pressure contours away from the wedge being modified by the previous SJA cycle with the contour lines having a noticeable dip toward the SJA due to the suction phase which had just finished in this snapshot. The velocity contour also shows a small amount modification compared to the baseline. The vortices inside the SJA orifice are much stronger with the center of circulation clearly seen. The temperature just above the wedge surface is still several tens of degrees above freezing even with this snapshot being the farthest time from peak ejection. This warmer temperature is also carried nearly to the back of the wedge with some cooling taking place downstream.

The total ice accretion (Figure 33) exhibits a marked decrease in the amount of ice on the surface of the wedge with only trace amounts seen near the front and a small section at the rear. This is presumably solely due to the temperature of the residual air ejected from the heated SJA chamber since this amount of reduction was not observed in the non-heated actuating case and this snapshot should give the most amount of ice accretion.

Figure 34 shows how little instant ice growth exists for this time snapshot with their only being the trace amount detected. While the temperature of the flow over the surface of the wedge is not high enough to evaporate the impinging water droplets, the flow does make it difficult for ice to form by heating the wedge surface and not allowing any ice crystals to stick.

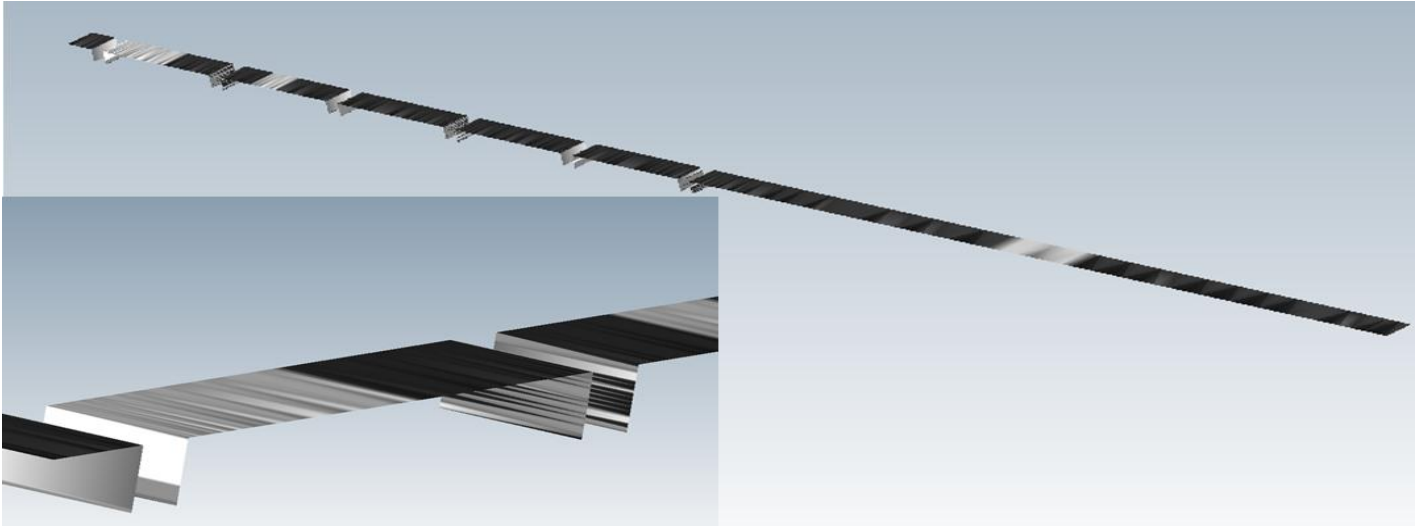


FIGURE 33: ICE ACCUMULATION. SMALLER PICTURE IS OF THE FRONT OF THE WEDGE.

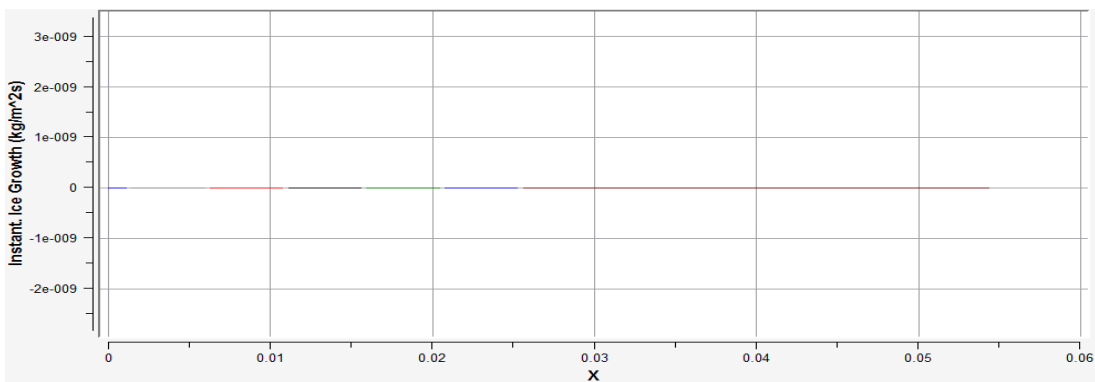


FIGURE 34: INSTANT ICE GROWTH PLOT

4.4.2 SNAPSHOT 2

The second snapshot is when the SJA is fully ejecting the hot air out of the orifice and into the flow above the wedge. The pressure and velocity contours in Figure 35 still show modification from the actuation with the small velocity and pressure bubbles aft of the SJA orifices seen in case C beginning to form. The temperature field shows these structures clearly with the heat air flowing over them.

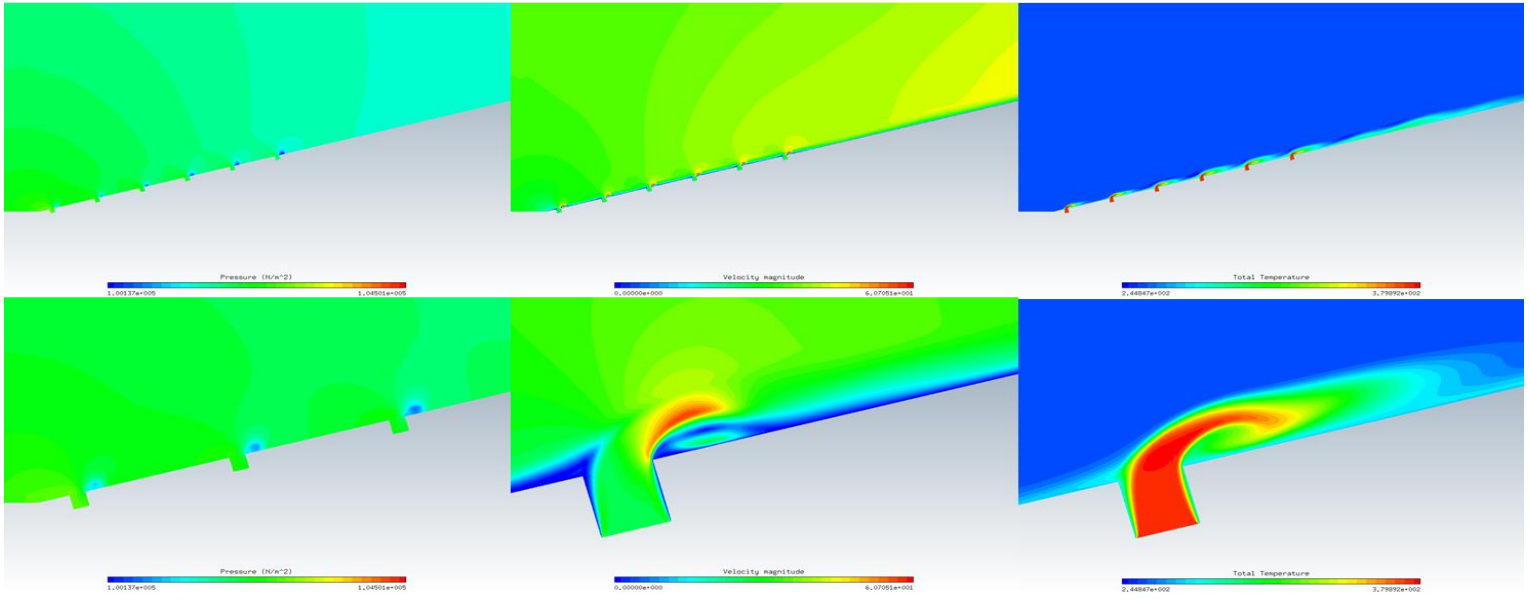


FIGURE 35: PRESSURE (LEFT), VELOCITY (MIDDLE) AND TEMPERATURE (RIGHT) CONTOURS.
 BOTTOM CONTOURS ARE CLOSEUPS.

The ice accretion in Figure 36 exhibits a very similar pattern as the previous snapshot with trace amounts of ice between the first and second SJA and a small section near the end of the wedge. The heat conduction through the wedge surface from the heated air keeps the temperature high enough to impede the ice accretion process and only allow these trace amounts to form. Figure 37 displays the instant ice growth for this time snapshot and contains the same trace amounts as the previous snapshot.

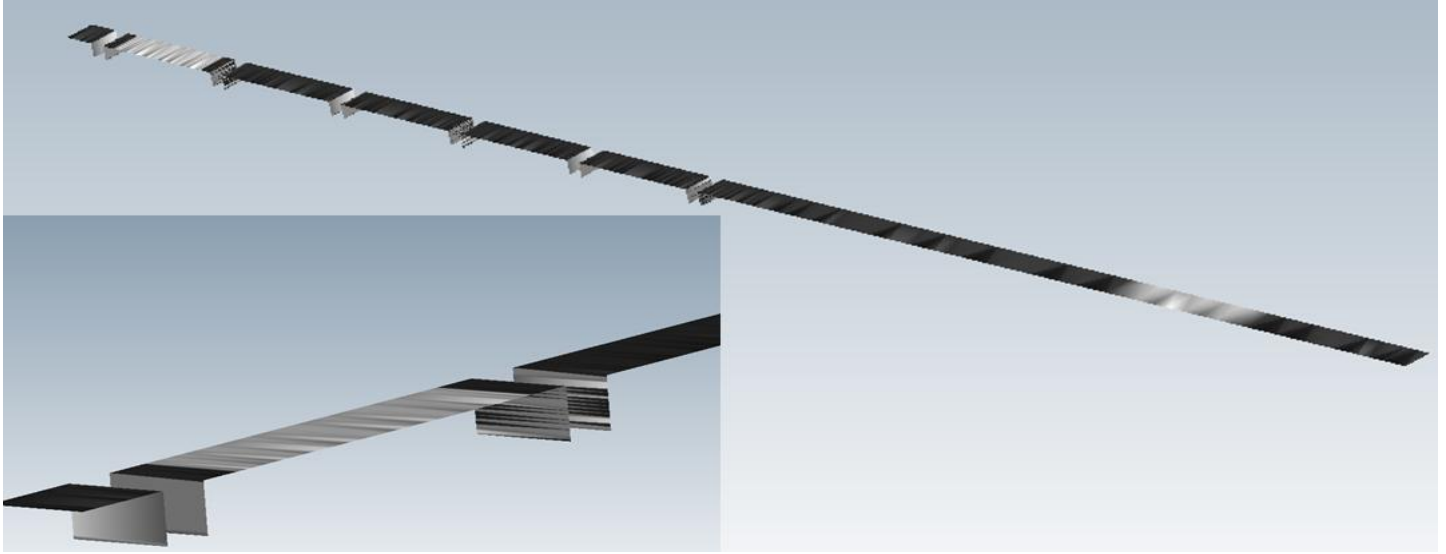


FIGURE 36: ICE ACCUMULATION. SMALLER PICTURE IS OF THE FRONT OF THE WEDGE.

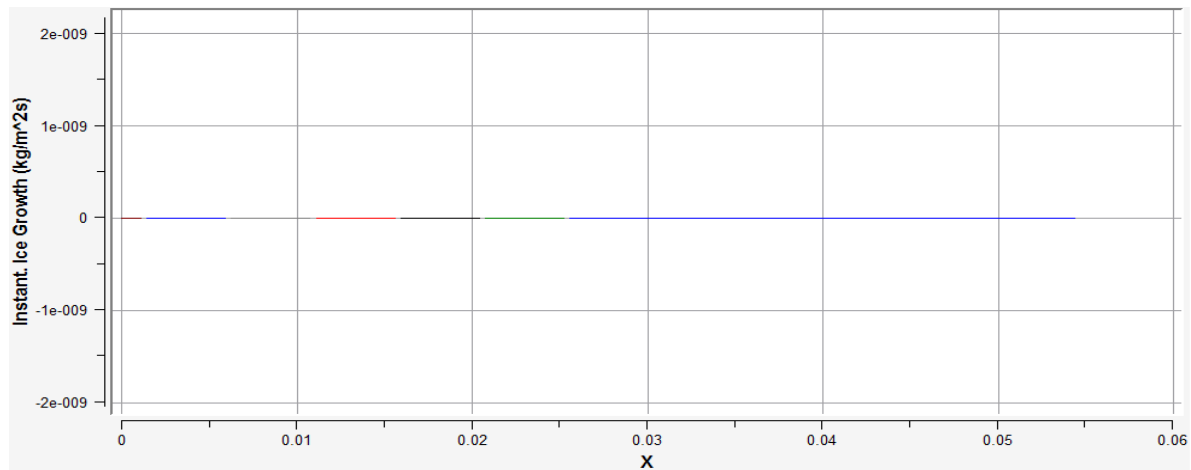


FIGURE 37: INSTANT ICE GROWTH PLOT

4.4.3 SNAPSHOT 3

The third snapshot is when the SJA velocity is zero in between the ejection and suction phases as previously described in the section on Case C. The pressure and velocity low fields (Figure 38) show similar characteristics as in that case but the temperature field has high temperature air flowing back along the wedge wall while it cools slightly.

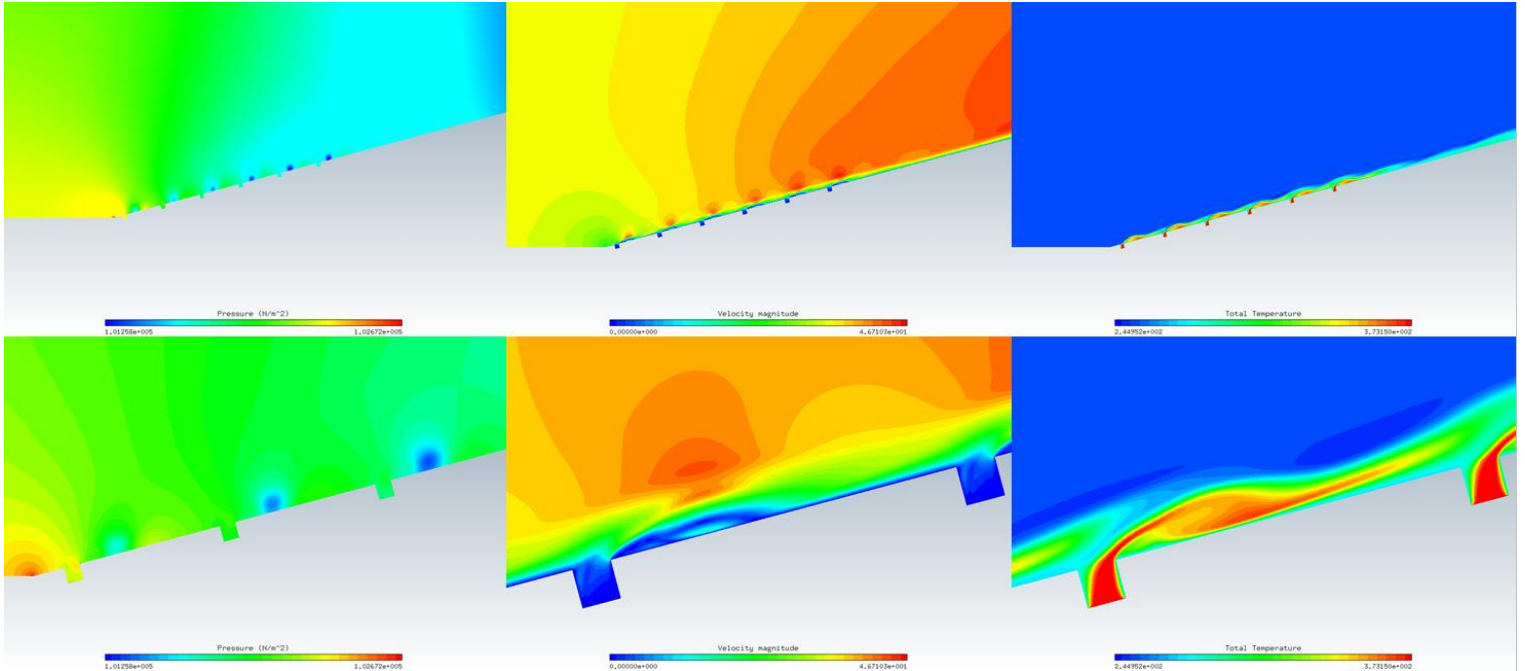


FIGURE 38: PRESSURE (LEFT), VELOCITY (MIDDLE) AND TEMPERATURE (RIGHT) CONTOURS.

BOTTOM CONTOURS ARE CLOSEUPS.

The ice accretion in Figure 39 shows much less ice compared to Case C but with different locations of the trace ice when compared to the previous two snapshots. The different locations are due to the change of the temperature and velocity fields compared to the previous times. The heat from the ejected SJA air keeps the flow near the wedge warm enough to prevent ice formation due to the impinging supercooled droplets. Figure 40 shows that all of the ice in Figure 39 is only a trace amount.

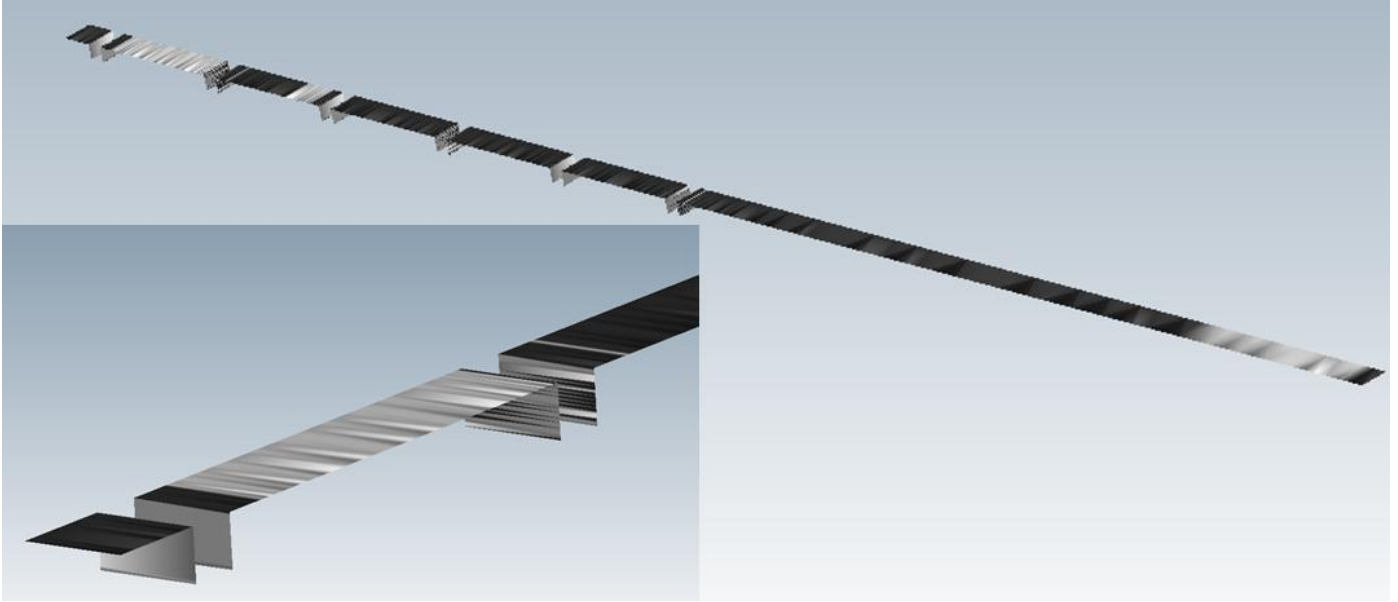


FIGURE 39: ICE ACCUMULATION. SMALLER PICTURE IS OF THE FRONT OF THE WEDGE.

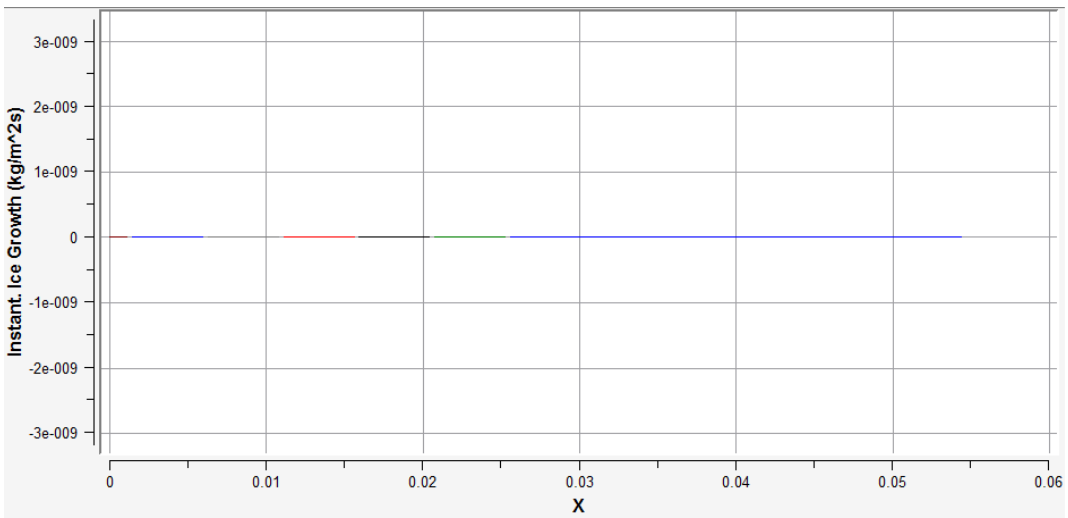


FIGURE 40: INSTANT ICE GROWTH PLOT

4.4.4 SNAPSHOT 4

The last snapshot is when the SJA is fully in the suction phase with a velocity normal to the inlet set to -25m/s. The pressure contour in Figure 41 has the expected increase of pressure at the tip of the wedge but has bubbles of high pressure behind the SJA's in contrast to the previous

snapshots. The velocity shows the expected flow field lines into the SJA due to the suction. The temperature field in Figure 41 shows the interesting feature of the SJA's pulling in the previously ejected air warmer air of the SJA upstream. This has some important consequences for the power required for heating each SJA since some of the air flowing into the chamber would already be tens of degrees above the freestream temperature. This would reduce the amount of power required to heat the air in the SJA chamber for the SJA's downstream.

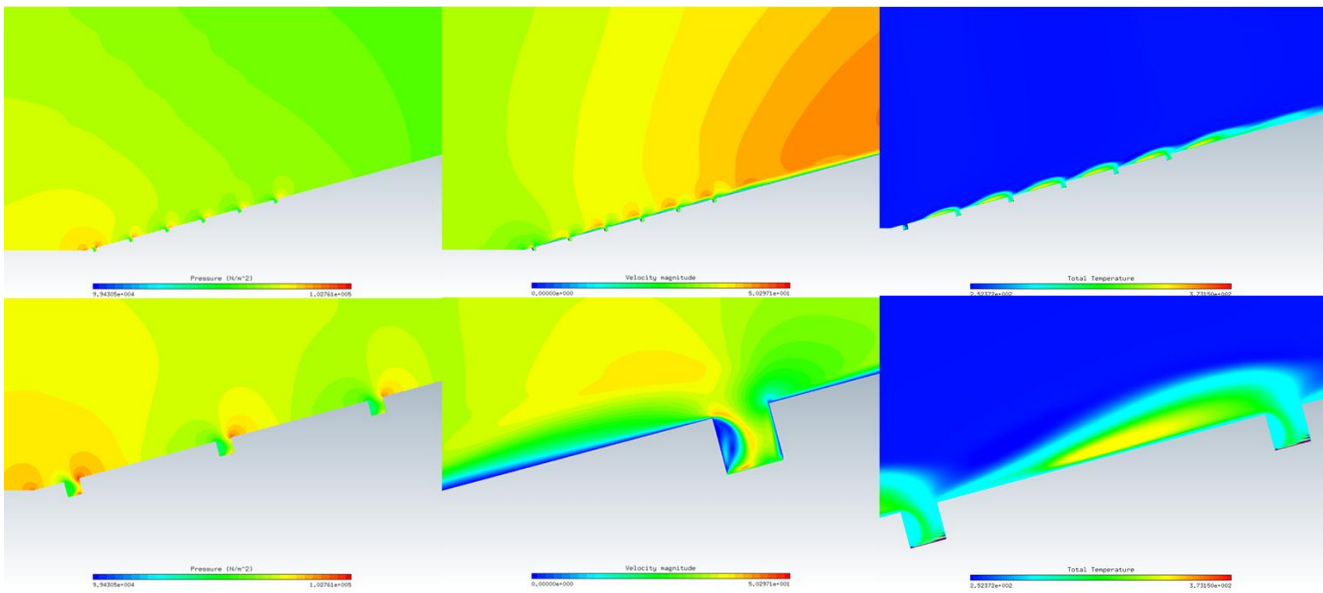


FIGURE 41: PRESSURE (LEFT), VELOCITY (MIDDLE) AND TEMPERATURE (RIGHT) CONTOURS.
 BOTTOM CONTOURS ARE CLOSEUPS.

Figure 42 still shows some amount of ice accretion on the surface of the wedge in different locations compared to the previous snapshots but Figure 43 proves that this is only a trace amount. The flow field just above the wedge is still at a higher temperature than the freestream which continues to impede ice growth. This also acts to keep the temperature of the solid wedge above freezing which contributes to the anti-icing performance.

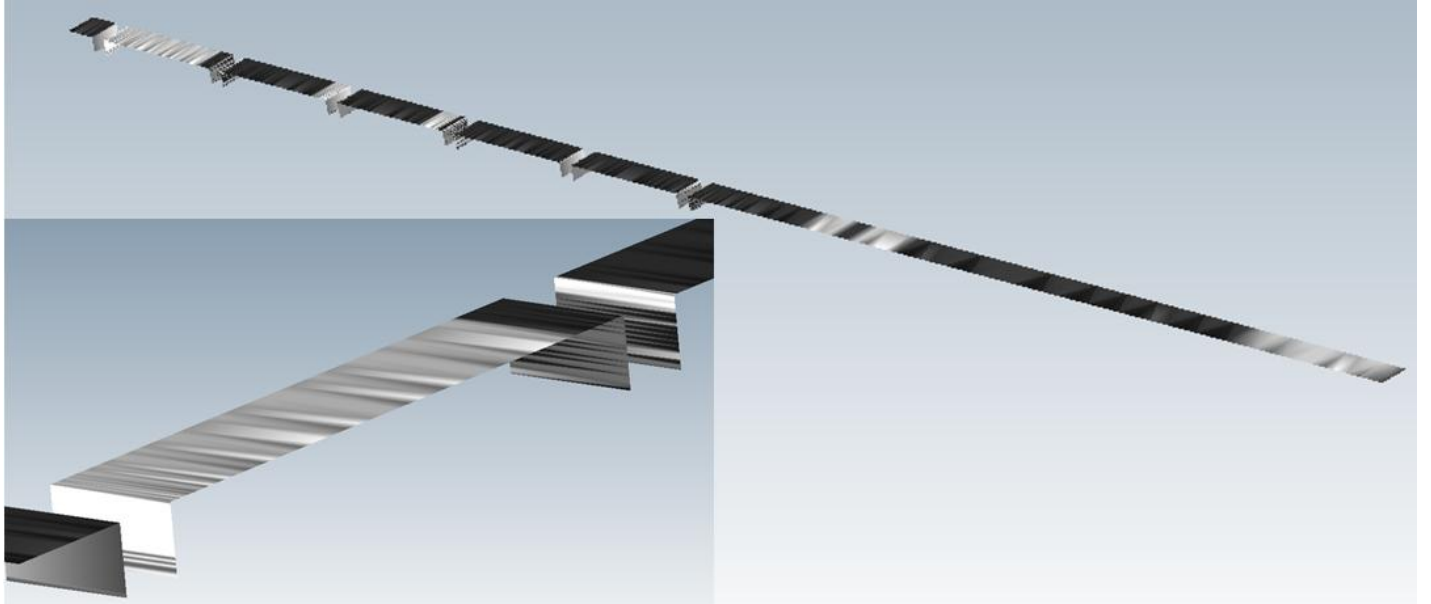


FIGURE 42: ICE ACCUMULATION. SMALLER PICTURE IS OF THE FRONT OF THE WEDGE.

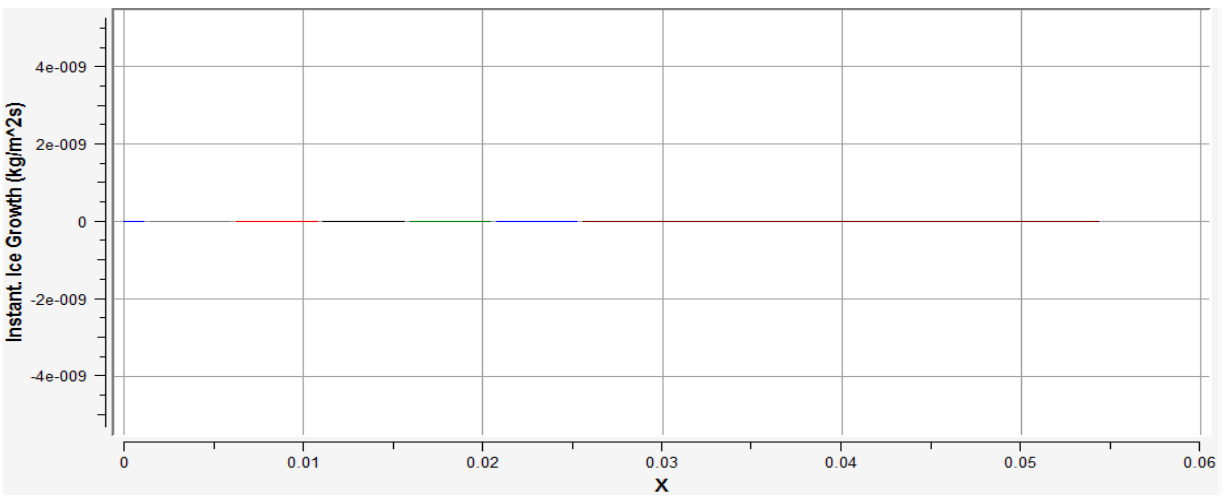


FIGURE 43: INSTANT ICE GROWTH PLOT

CHAPTER 5: CASE D PARAMETRIC STUDY

This chapter will use the heated and actuated SJA case as a basis for a parametric study on the effects of ice accretion due to four separate parameters as detailed in section 3.4. Only time snapshots one and three will be considered for these cases due to the previous chapter suggesting they contain the most ice (snapshot 1) and least ice (snapshot 3) compared to snapshots two and four. The flow conditions for each sub-case are very similar to Case D in the previous chapter and will not be discussed in this chapter. The specific flow results and snapshots two and four can be found in the Appendix.

5.1 PARAMETRIC STUDY I: DROPLET DISTRIBUTION

The first parametric study will analyze the effect that droplet distribution has on ice accretion over the surface of the wedge. The Langmuir-D distribution is centered on 20microns with the monodisperse distribution being equal to 20microns. Both cases have an SJA chamber temperature of 75°C with a freestream temperature of -20°C.

5.1.1 SNAPSHOT 1

The ice accretion for both cases is shown in Figure 44 with the Langmuir-D distribution on the right and the monodisperse distribution on the left. Unlike case C in the previous chapter, there is not any difference in ice accretion between the two distributions. This is due to the heated air from the SJA increasing the temperature of the wedge wall thereby hindering ice accretion. The plot in Figure 45 show how similar the ice thicknesses between the

cases are after ten seconds. Both distributions show ice growth near the front of the wedge with only a trace amount farther back.

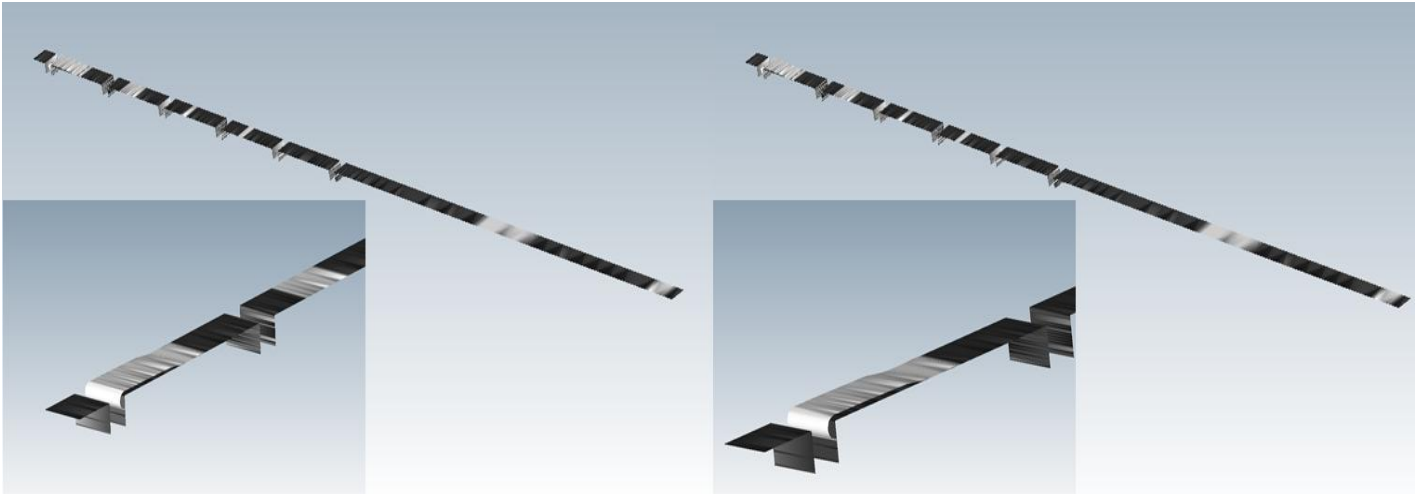


FIGURE 44: ICE ACCUMULATION (MONODISPERSE LEFT, LANGMUIR RIGHT)

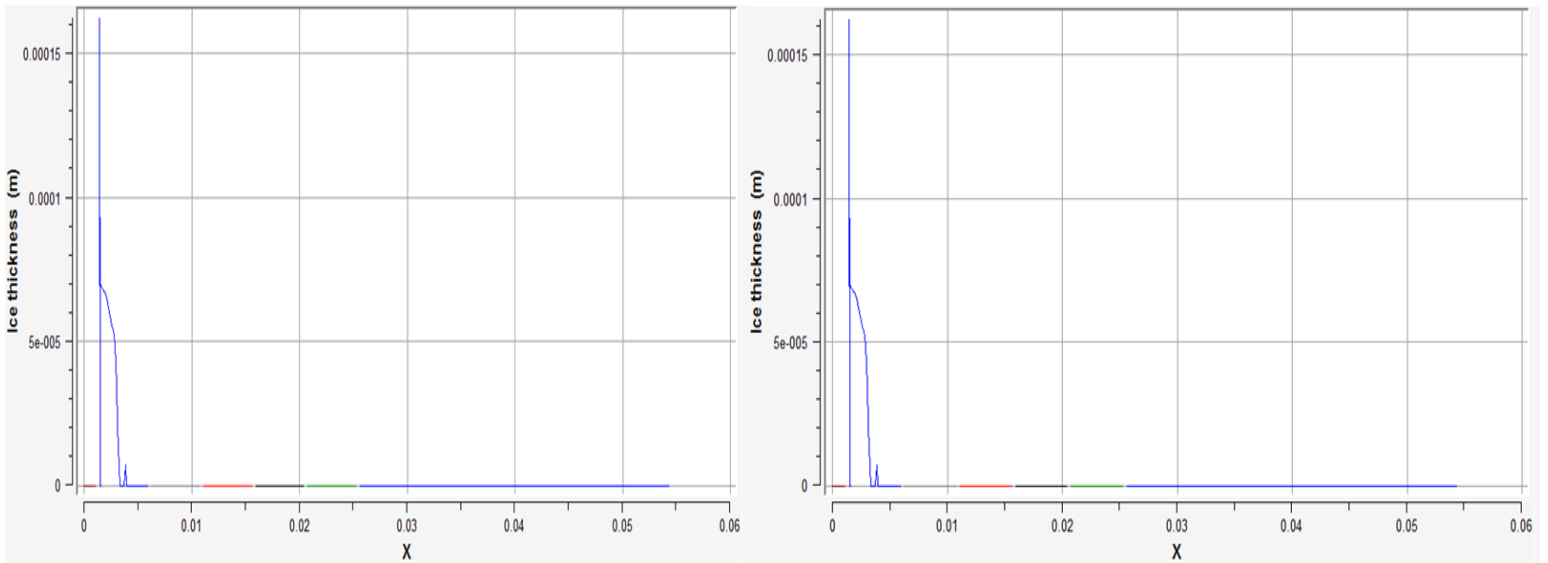


FIGURE 45: ICE THICKNESS PLOT (MONODISPERSE LEFT, LANGMUIR RIGHT)

5.1.2 SNAPSHOT 3

The third snapshot only has a trace amount of ice accumulation for both distributions as seen in Figure 46. The decreased ice accumulation is due to the amount of hot air flowing over the surface of the wedge from the SJA's. There are some slight differences in the trace amounts of ice that have formed, specifically the length of the ice at the end of the wedge and some accretion just after the first SJA. The total ice thickness plots in Figure 47 show that these trace amounts are negligible so it is concluded that the droplet distribution with small diameter droplets does not have a large impact on the amount of ice accretion with heated and actuated SJA's.

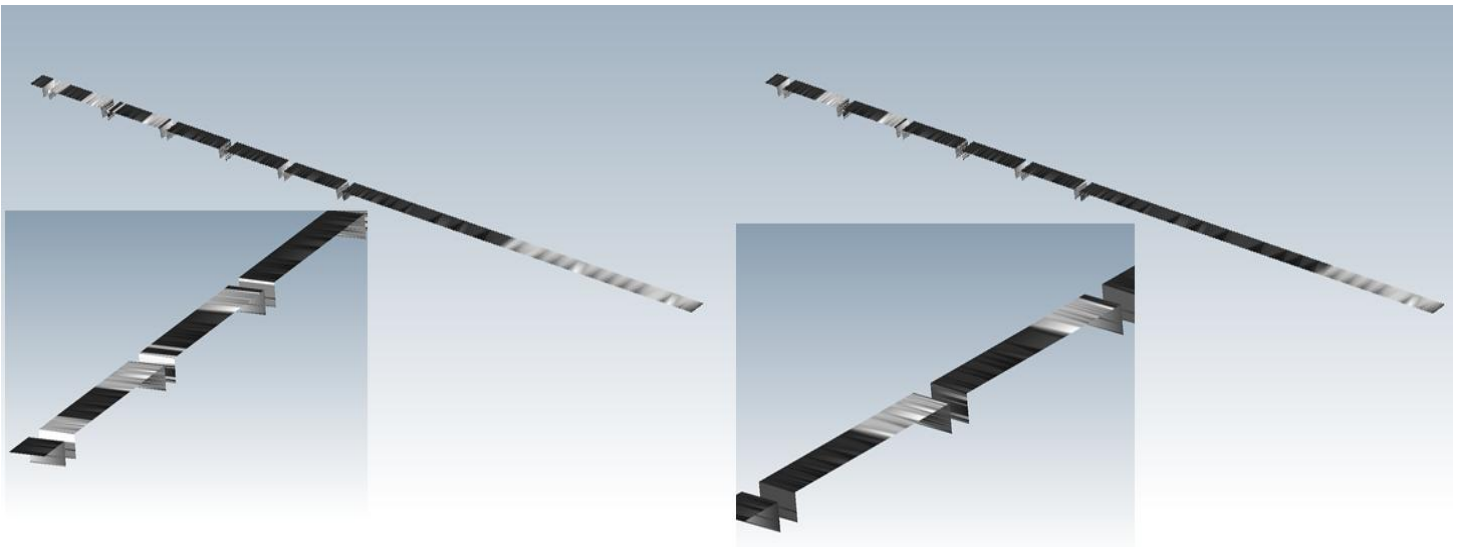


FIGURE 46: ICE ACCUMULATION (MONODISPERSE LEFT, LANGMUIR RIGHT)

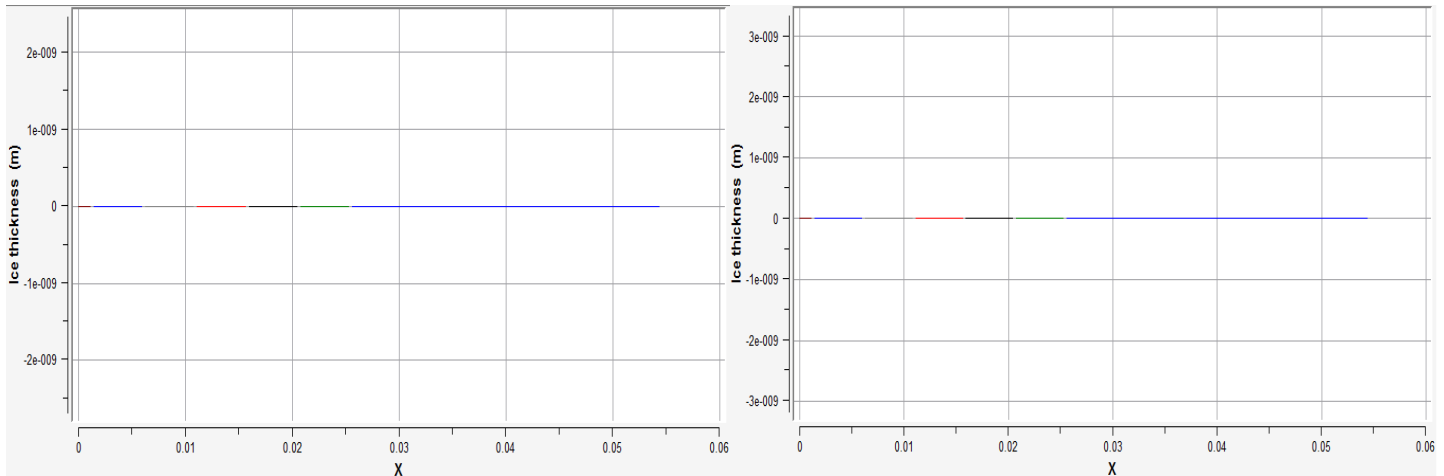


FIGURE 47: ICE THICKNESS PLOT (MONODISPERSE LEFT, LANGMUIR RIGHT)

5.2 PARAMETRIC STUDY II: SJA INLET TEMPERATURE VARIATION

This study will analyze the effect of SJA inlet temperatures of 75°C and 100°C on ice accretion over the wedge. A Langmuir-D droplet distribution with 20micron droplets is used with a freestream temperature of -20°C.

5.2.1 SNAPSHOT 1

Figure 48 shows the accumulation of ice after ten seconds with an SJA chamber temperature of 75°C on the left and 100°C on the right. The area of the surface just behind the first SJA exhibits noticeable ice accretion in the 75°C case, the same area in the 100°C case only has a trace amount of ice. This may be due to the residual outflow from the first SJA leaving this area of the surface not having a high enough temperature to evaporate the impinging supercooled droplets.

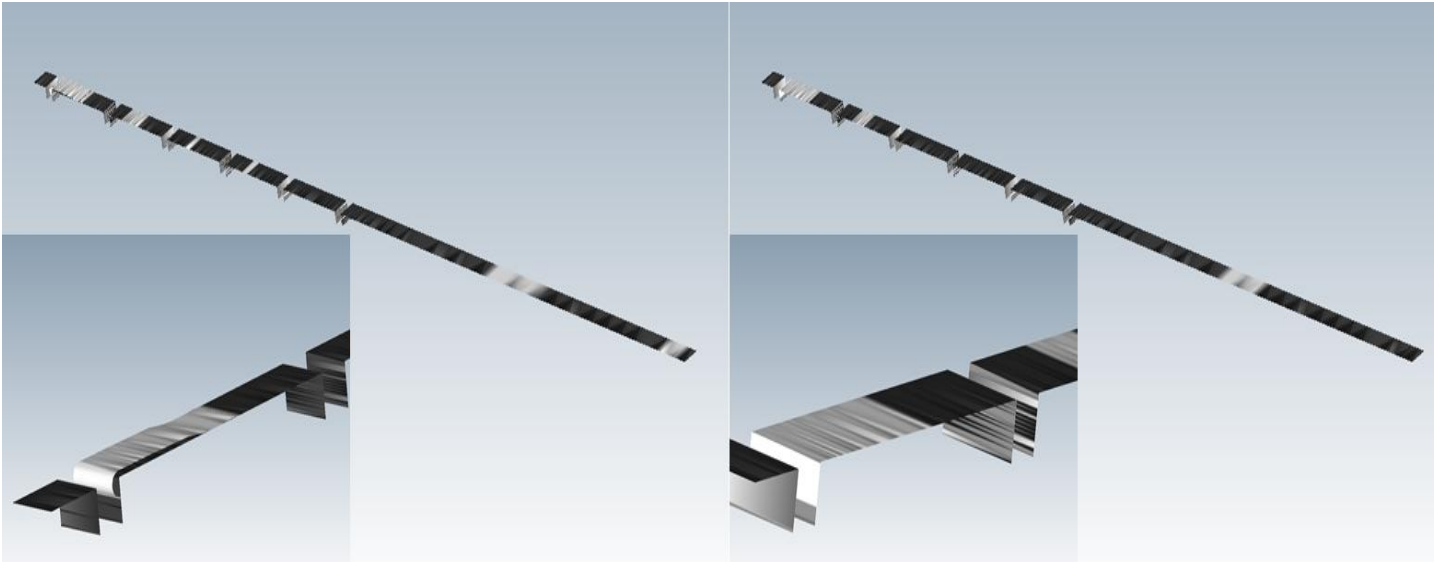


FIGURE 48: ICE ACCUMULATION (INLET TEMPERATURE: 75C LEFT, 100C RIGHT)

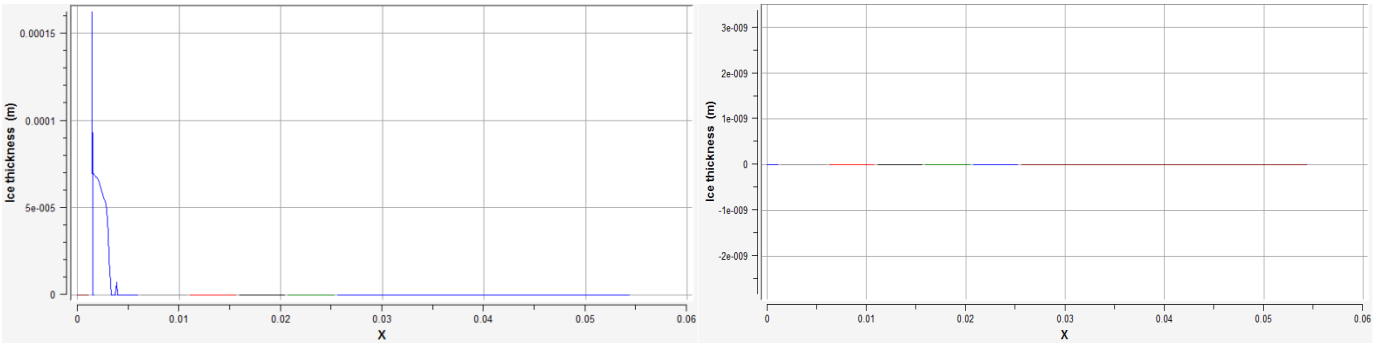


FIGURE 49: ICE THICKNESS PLOT (INLET TEMPERATURE: 75C LEFT, 100C RIGHT)

The ice thickness plot in Figure 49 clearly show the difference in ice accumulation at the front of the surface with the rear sections for both cases only containing trace amounts of ice. Figure 50 shows the temperatures of the solid grid due to the SJA outflow over the surface after the CHT3D analysis. It can be seen that the temperature of this sold is tens of degrees higher for the 100°C case compared to the 75°C case which has the effect of reducing the amount of ice accretion.

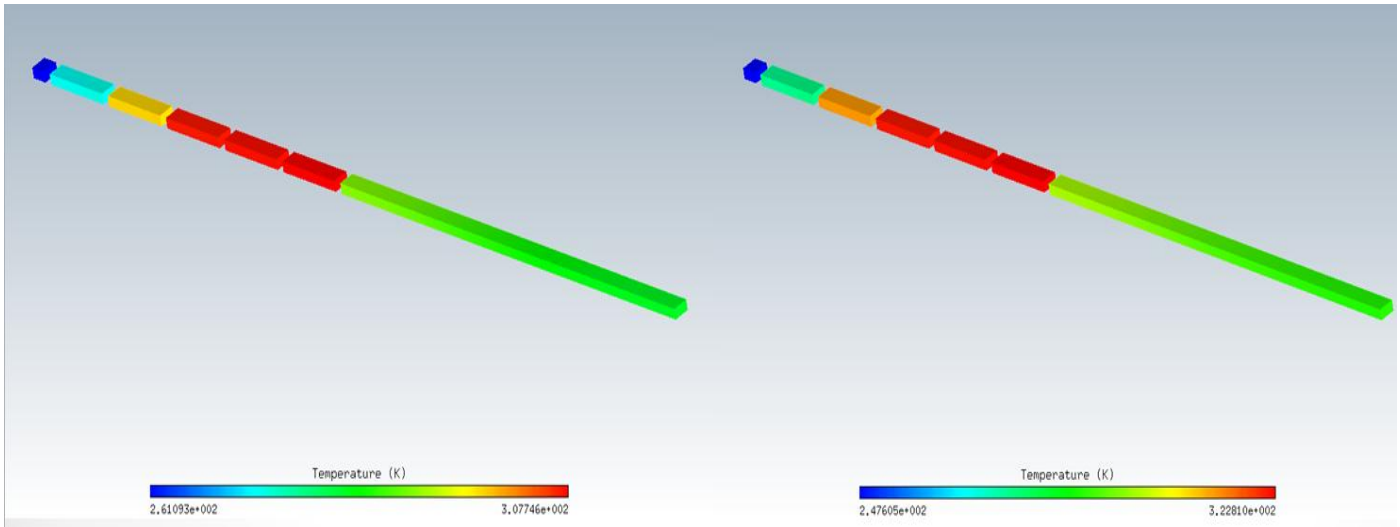


FIGURE 50: SOLID TEMPERATURE (INLET TEMPERATURE: 75C LEFT, 100C RIGHT)

5.2.3 SNAPSHOT 3

The ice accumulations in Figure 51 and the ice thickness plot in Figure 52 both show only trace amounts of ice accumulation on the surface of the wedge. The only difference is the location of the trace ice formations which may be due to some larger droplets experiencing water runback after impact and freeze further back along the surface in the 100°C case whereas these same droplets would freeze more quickly after impact in the 75°C case.

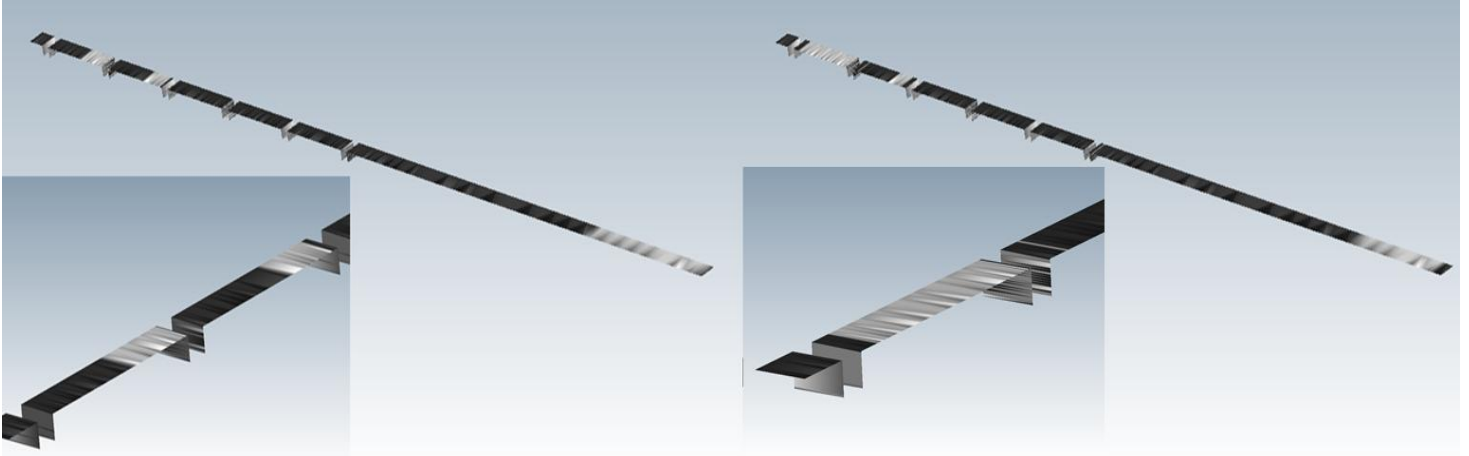


FIGURE 51: ICE ACCUMULATION (INLET TEMPERATURE: 75C LEFT, 100C RIGHT)

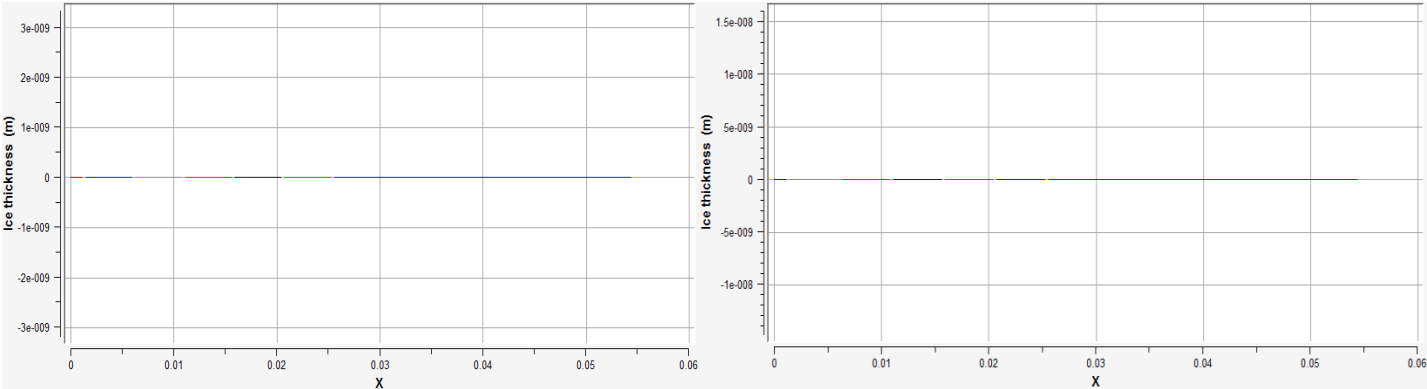


FIGURE 52: ICE THICKNESS PLOT (INLET TEMPERATURE: 75C LEFT, 100C RIGHT)

The temperatures of the solid grid in Figure 53 have higher temperatures when compared to the first snapshot which is expected due to the higher temperature flow over the wedge surface from the SJA outflow. Note that the temperature of the solid domain towards the end of the wedge is converged to approximately 10-12 degrees centigrade due to the outflow from the SJA’s cooling as it flows to the end of the wedge (Refer the Appendix for the fluid temperature profiles).

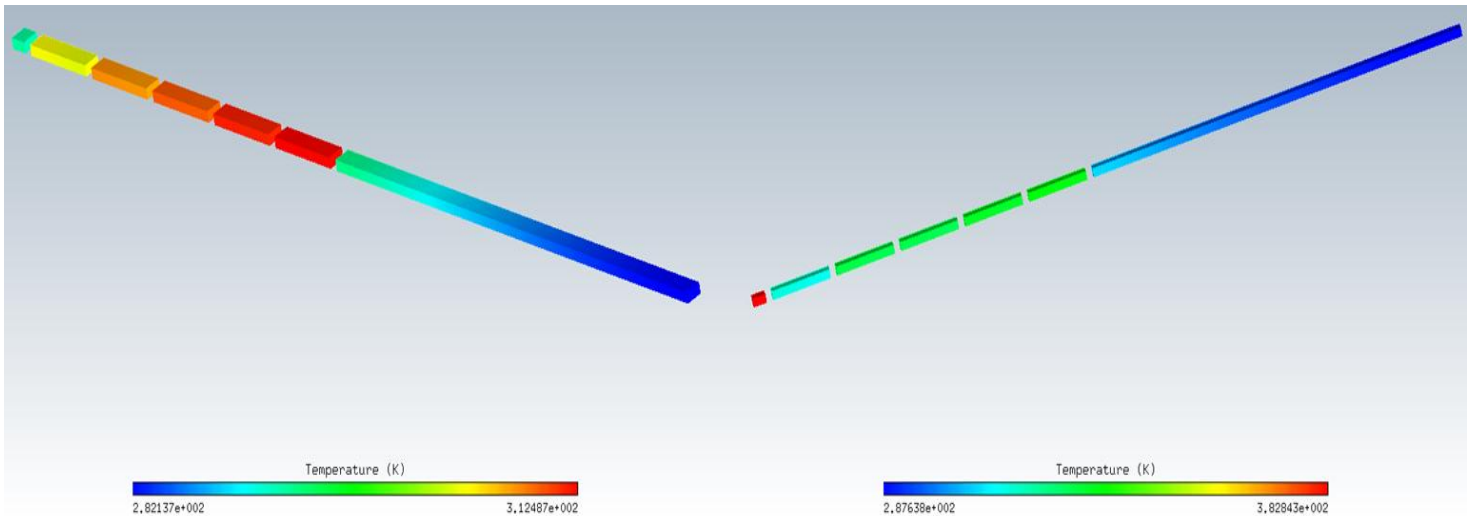


FIGURE 53: SOLID TEMPERATURE (INLET TEMPERATURE: 75C LEFT, 100C RIGHT)

5.3 PARAMETRIC STUDY III: SSD AND SLD

The third parametric study analyzes the effect of 20micron MVD compared to 100micron MVD on ice accretion over the surface of the wedge. A Langmuir-D droplet distribution with a SJA chamber temperature of 100°C and a freestream temperature of -20°C is used for both cases.

5.3.1 SNAPSHOT 1

Figure 54 shows the ice accumulation due to a Langmuir-D droplet distribution centered around 20microns (left) and ice accumulation due to a Langmuir-D droplet distribution centered around 100microns (right). Both cases only show trace amounts of ice formation in nearly the exact same locations along the surface. Figure 55 shows the ice thickness being nearly zero throughout the wedge for both the large and small droplet sizes.

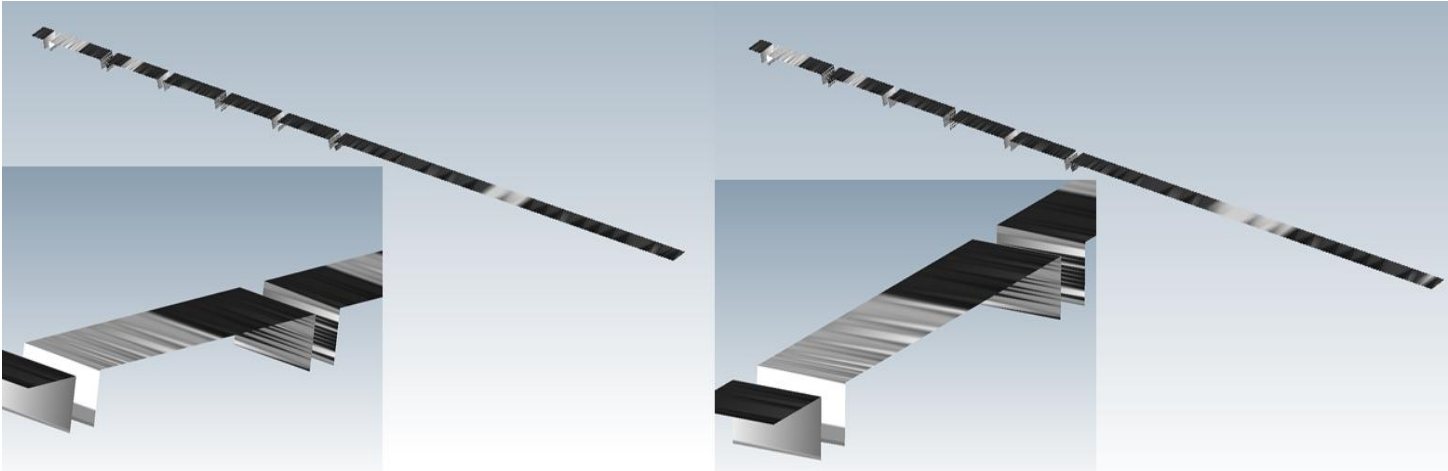


FIGURE 54: ICE ACCUMULATION (SSD LEFT, SLD RIGHT)

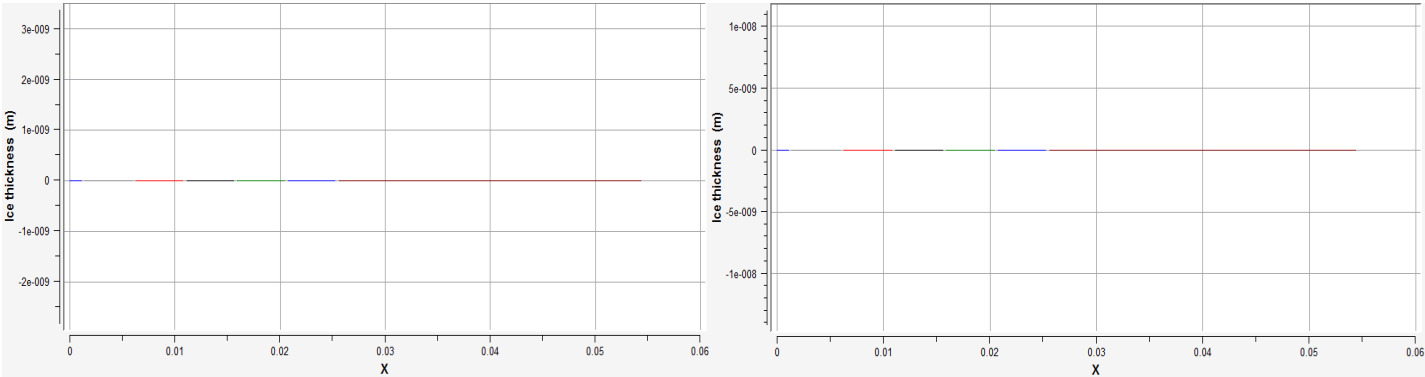


FIGURE 55: ICE THICKNESS PLOT (SSD LEFT, SLD RIGHT)

5.3.3 SNAPSHOT 3

The ice accumulation in Figure 56 and the ice thickness plot in Figure 57 again only shows trace amounts along the surface of the wedge for both large and small droplets. There are some small differences in the size of the patches that can be explained by water film runback from the larger droplets. When large droplets impact the surface of the wedge only a portion will freeze upon impact with the rest of the water from the droplet becoming runback and being carried farther downstream by the flow field freezing again. This explains the larger patch of ice at the front of the wedge in the small droplet case and the larger patch at the rear of the wedge in

the large droplet case. The smaller droplets are forming rime ice while the larger ones cause glaze due to runback water.

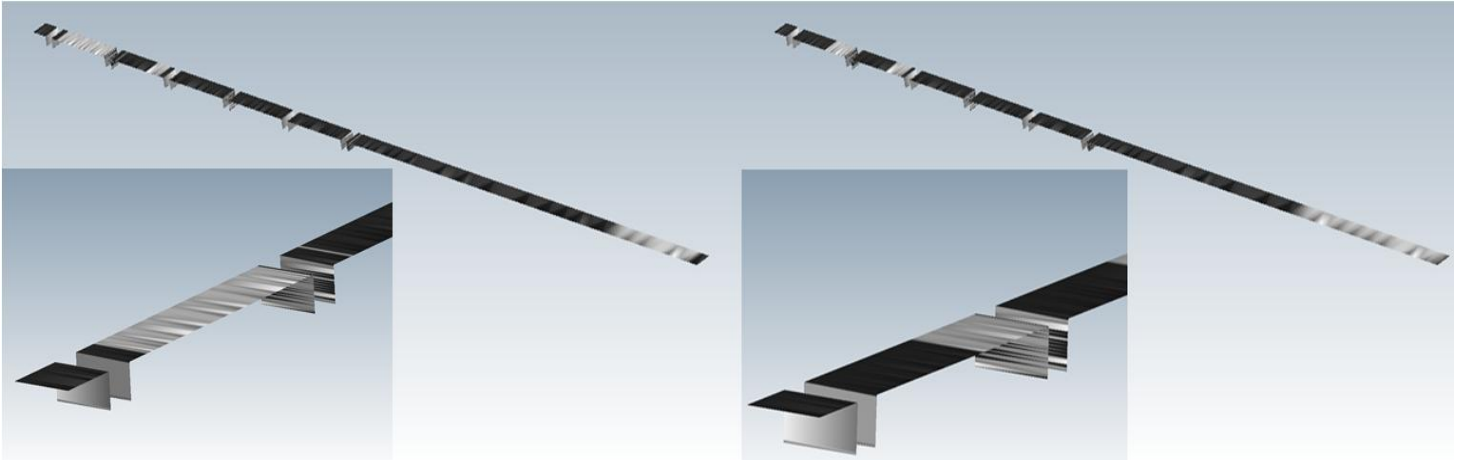


FIGURE 56: ICE ACCUMULATION (SSD LEFT, SLD RIGHT)

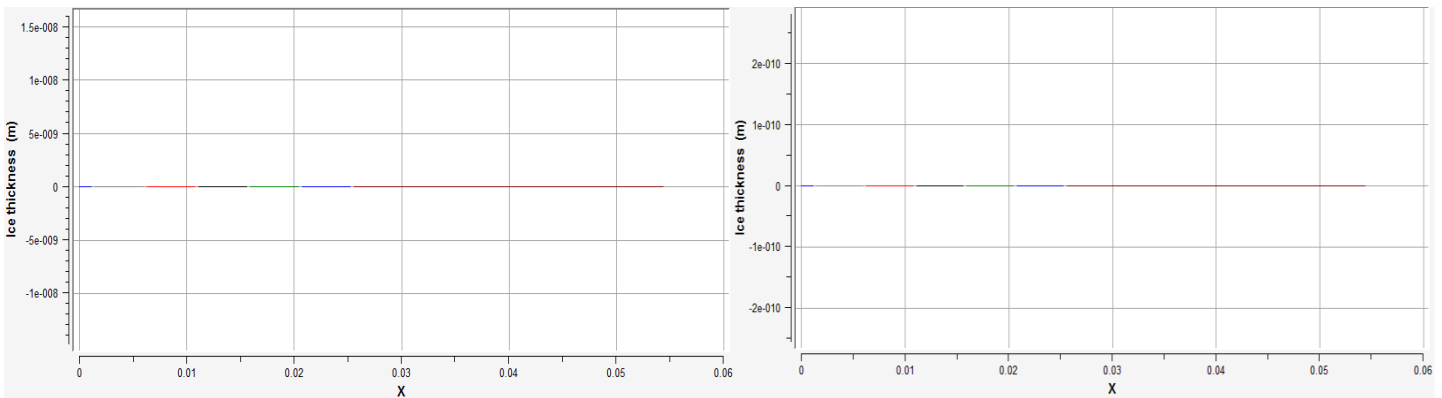


FIGURE 57: ICE THICKNESS PLOT (SSD LEFT, SLD RIGHT)

5.4 PARAMETRIC STUDY IV: FREESTREAM TEMPERATURE VARIATION

The last parametric study will investigate the effects of freestream temperature on ice accumulation on the wedge with the heated and actuated SJA's. Freestream temperatures of -20°C and -10°C are used to study the effects of the heated and actuated SJA's on rime and glaze

ice. A Langmuir-D distribution centered around 20microns with a SJA chamber temperature of 100°C is used for this study.

5.4.1 SNAPSHOT 1

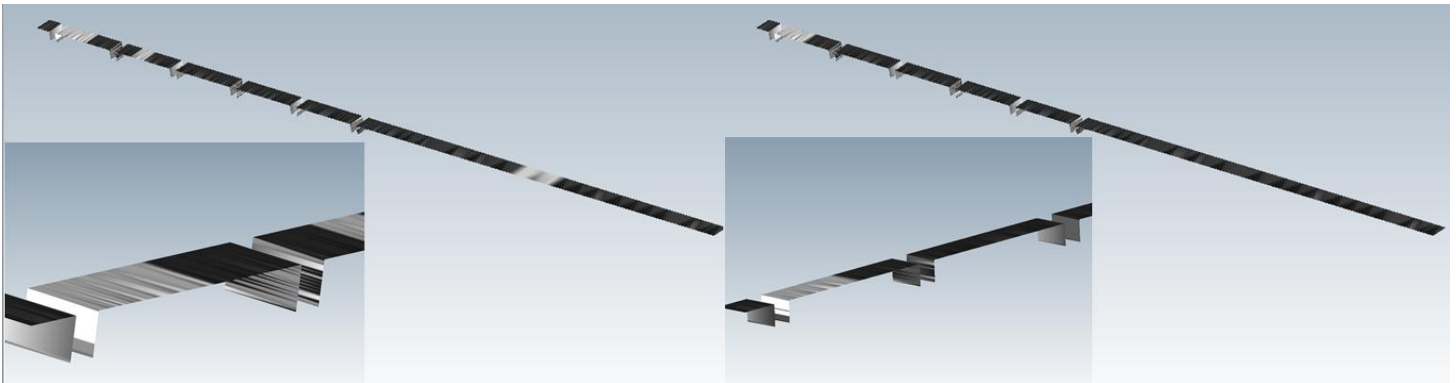


FIGURE 58: ICE ACCUMULATION (FREESTREAM TEMPERATURES OF -20C LEFT, -10 RIGHT)

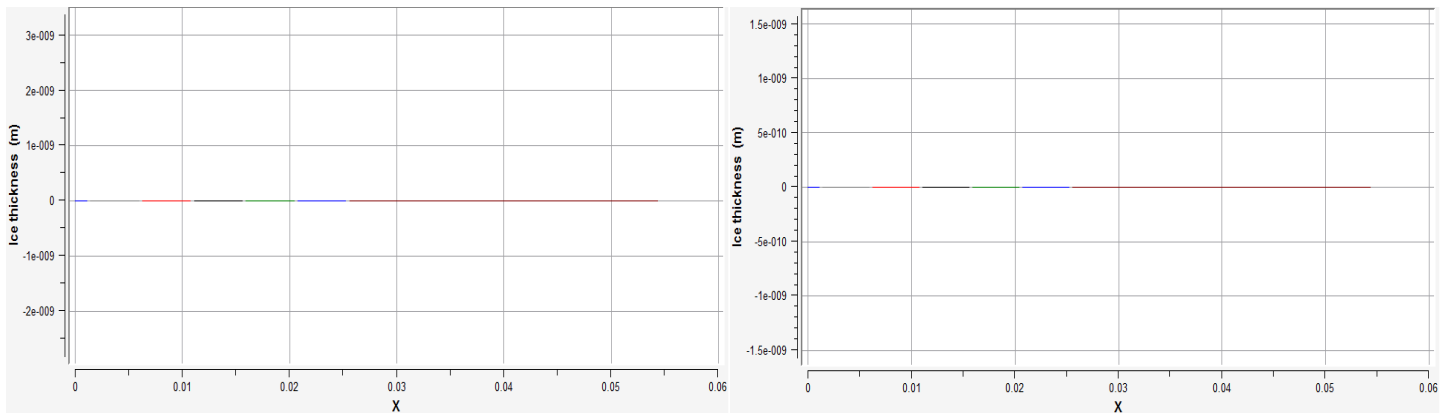


FIGURE 59: ICE THICKNESS PLOT (FREESTREAM TEMPERATURES OF -20C LEFT, -10 RIGHT)

Figure 58 and Figure 59 show the effects of freestream temperature on the amount of ice accretion with -20°C on the left and -10°C on the right. Both cases show only trace amounts of ice accretion with the -20°C case having a slight amount more. Rime and glaze ice form at different temperature ranges so these results suggest that the SJA's are effective in anti-icing

with both types of ice. Figure 60 shows the temperature of the solid domain which has only a few degrees of difference between the two freestream temperature conditions.

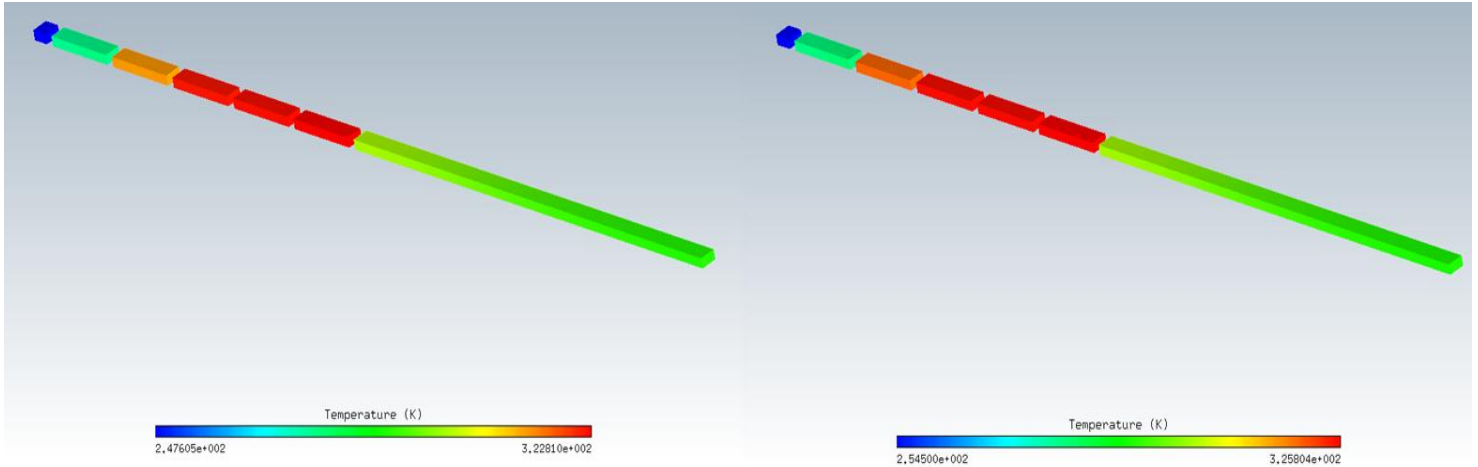


FIGURE 60: SOLID TEMPERATURE (FREESTREAM TEMPERATURES OF -20C LEFT, -10 RIGHT)

5.4.3 SNAPSHOT 3

For the third snapshot, the lower freestream temperature caused an increase in the amount of accreted trace ice on the surface of the wedge shown in Figure 61. This may be caused by the mechanism that forms rime ice with the supercooled droplets impinging on the surface and immediately freezing. This does not allow enough time for the SJA's to evaporate the ice completely so a trace amount will form. Conversely, glaze ice is formed by water runback due to the impinging droplets so there is sufficient time for the SJA's to heat and evaporate the droplets and the runback off the wedge surface.

Figure 63 shows the temperature of the solid for both freestream temperature conditions. At this snapshot, the temperature of the solid is higher when compared to snapshot one but the two cases are still only within a few degrees of each other.

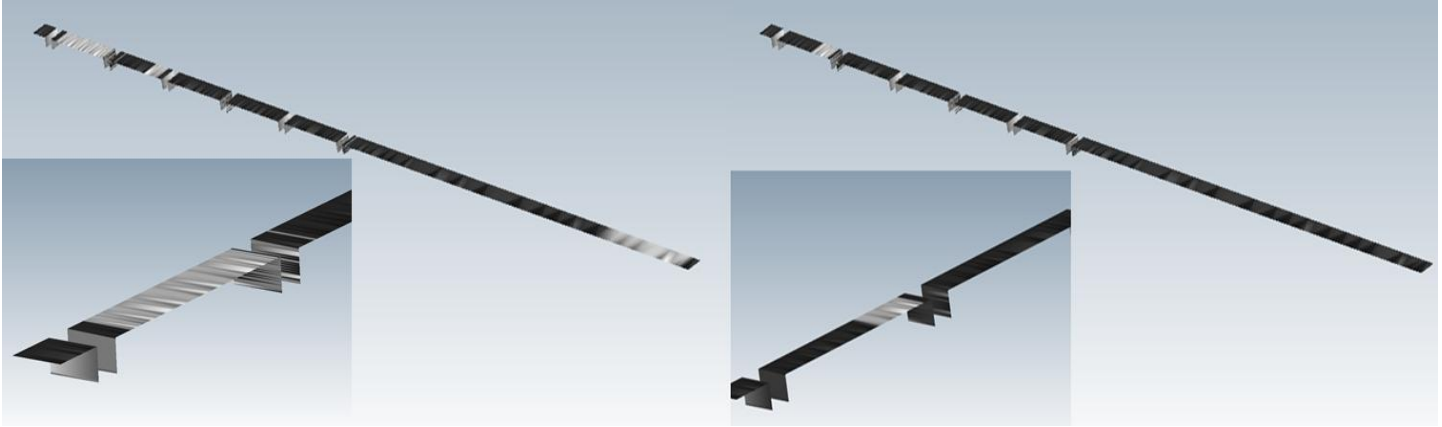


FIGURE 61: ICE ACCUMULATION (FREESTREAM TEMPERATURES OF -20C LEFT, -10 RIGHT)

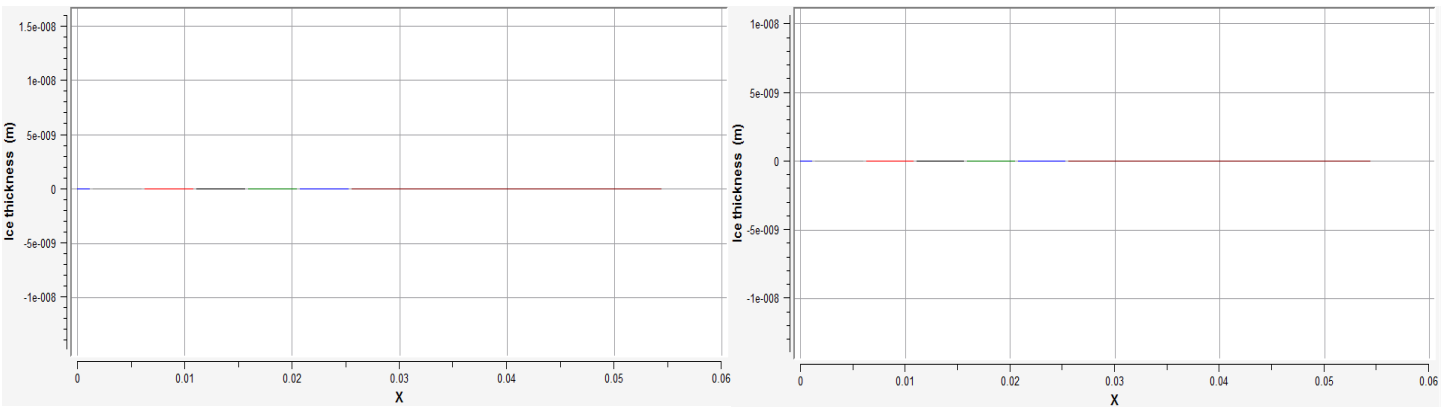


FIGURE 62: ICE THICKNESS PLOT (FREESTREAM TEMPERATURES OF -20C LEFT, -10 RIGHT)

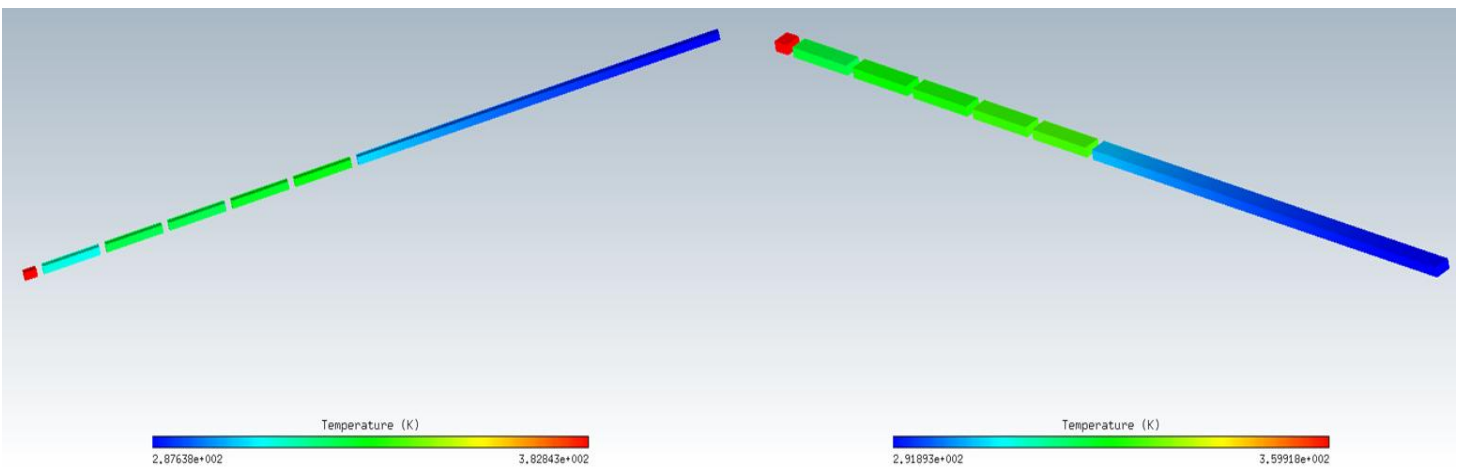


FIGURE 63: SOLID TEMPERATURE (FREESTREAM TEMPERATURES OF -20C LEFT, -10 RIGHT)

5.5 ONE SJA ANTI-ICE EFFECTIVENESS

The effectiveness of one SJA is analyzed as part of a future optimization study on number of SJA's and the distance between them. This case has a Langmuir-D distribution with a MVD of 20microns, an SJA inlet temperature of 100°C, and a freestream temperature of -20°C. This will only be for snapshot 3, after full ejection, due the heated air over the wedge that has not cooled completely will give a minimum value of the ice accretion on the surface.

Figure 64 shows the ice accretion on the surface of the wedge after 10 seconds. The wedge surface clearly shows patches of the surface without any ice accretion due to the heated air from the previous cycle heating the surface of the wedge at the center. The heated air from the next cycle has kept a small section of wedge wall behind the SJA, ice-free. This patch section will travel down the length of the wedge until the freestream has cooled the heated air enough to not affect the surface ice accretion.

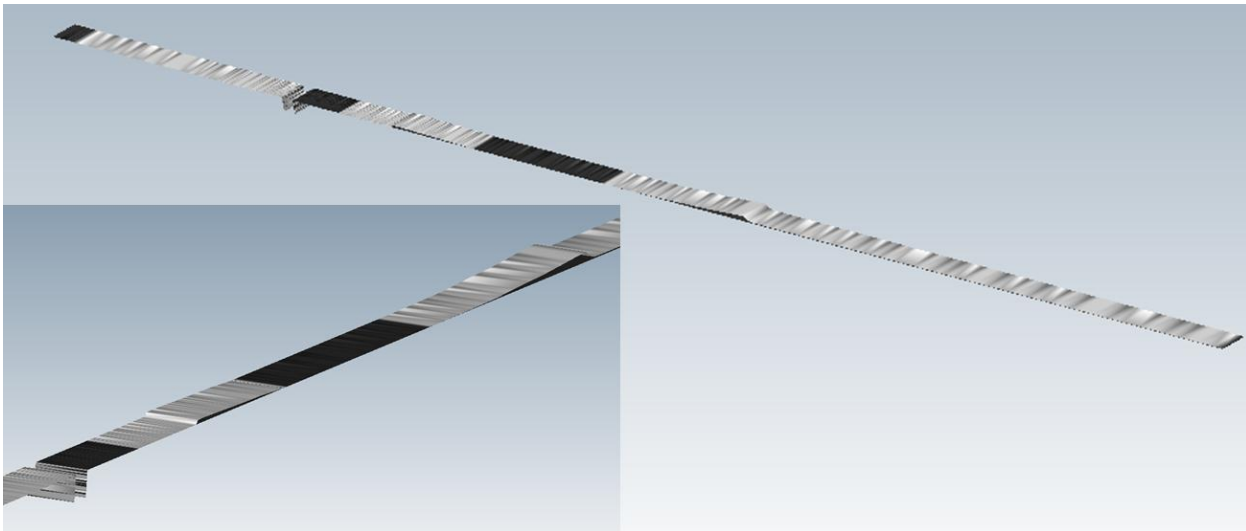


FIGURE 64: ICE ACCRETION USING ONE SJA

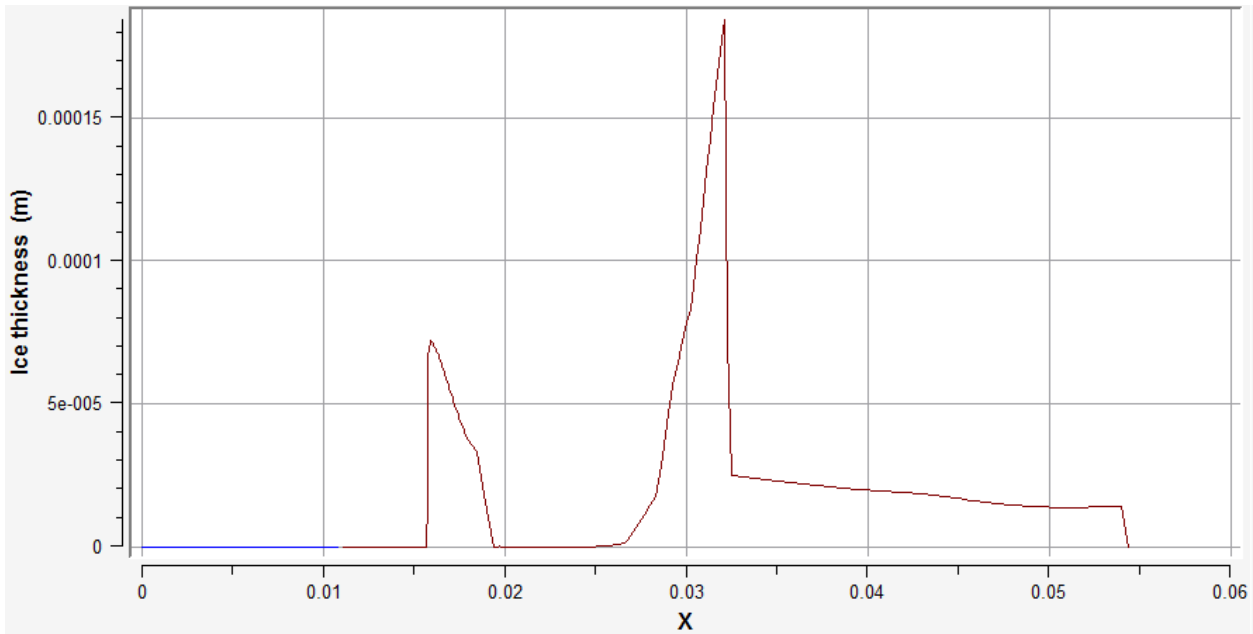


FIGURE 65 ICE THICKNESS PLOT USING ONE SJA

Figure 65 shows the ice thickness for this case which shows two clear spikes in ice thickness as previously seen. The portion of the wedge after this section has a normal amount of ice whereas the front of the wedge has a decreased amount. By using multiple SJA's and spacing them correctly the ice would not have a chance to form.

5.6 PRELIMINARY POWER REQUIREMENT FOR HEATED AND ACTUATED SJA

The power required for a single SJA to heat -20°C air up to 100°C will be compared to the power loss from a gas turbine engine with a bleed air system using the same mass flow. To begin, a realistic diaphragm displacement profile [23] is integrated spherically to find total volume of air displaced during each cycle:

$$\delta(r, t) = \frac{\Delta}{2} \left[1 - \frac{r^2}{r_c^2} + \frac{2r^2}{r_c^2} \ln \frac{r}{r_c} \right] \sin(2\pi ft) \quad \text{EQUATION 5.17}$$

The Δ is found by the following equation found from Reference [23]:

$$U_{peak} = \frac{\pi}{4} \Delta f \left(\frac{D_c}{D_o} \right)^2 \quad \text{EQUATION 5.18}$$

With $U_{peak} = 25 \frac{m}{s}$, $D_c = 15mm$, $D_o = 0.5mm$, and $f = 1000Hz$ the Δ becomes $3.5368e^{-5}m$.

Now the maximum displacement occurs when $\sin(2\pi ft) = 1$ so that the total volume of the displaced air inside the SJA is:

$$V = \int_0^{2\pi} \int_0^{\pi} \int_0^{r_c} \delta \left(r, \frac{1}{4f} \right) r^2 \sin \theta \, dr d\theta d\phi = 5e^{-12} \frac{m^3}{cycle} \quad \text{EQUATION 5.19}$$

Now using the Ideal Gas Law:

$$\dot{m} = \frac{PV}{RT} \quad \text{EQUATION 5.20}$$

Substituting the conditions $P = 101325Pa$, $R = 287 \frac{J}{kg \cdot K}$, $T = 373.15K$:

$$\dot{m} = 4.7307e^{-12} \frac{kg}{cycle} = 4.7307e^{-9} \frac{kg}{s} \quad \text{EQUATION 5.21}$$

Now with the definition of power:

$$\dot{Q} = C_p * \Delta T * f * \dot{m} \quad \text{EQUATION 5.22}$$

And using the following values: $C_p(air) = 1005 \frac{J}{kg \cdot K}$ $\Delta T = 100^\circ C - (-20^\circ C) = 120^\circ C$

$$\dot{Q} = 5.7052e^{-4}W \quad \text{EQUATION 5.23}$$

Which is the required energy to heat the displaced air inside the SJA per second.

A 15mm Piezoceramic diaphragm from APC International was used to find the current required to actuate the diaphragm at a maximum voltage suggested by the APC International of 30V peak to peak at a resonance frequency of 9.2kHz. At these conditions the diaphragm drew 6.4mA of current.

$$Power = VI = 6 * 30V * 6.4mA = 1.152W \quad \text{EQUATION 5.24}$$

$$Total\ SJA\ Power = 1.152W + 5.7052e^{-4}W = 1.1526W \quad EQUATION\ 5.25$$

To calculate the power loss from the gas turbine engine the isentropic relations are used to find the stagnation temperature and pressures with $T_a = 253.15$, $M_\infty = 0.1$, and $\gamma_\infty = 1.4$:

$$T_{0a} = T_a \left[1 + \frac{\gamma_\infty - 1}{2} M_\infty^2 \right] = 253.656K \quad EQUATION\ 5.26$$

$$P_{0a} = P_a \left[1 + \frac{\gamma_\infty - 1}{2} M_\infty^2 \right]^{\frac{\gamma_\infty}{\gamma_\infty - 1}} = 102036Pa \quad EQUATION\ 5.27$$

The power for a gas turbine engine for total mass flow rate $\dot{m}_{GT} = 285 \frac{kg}{s}$ is defined as:

$$Total\ Power = \dot{m}C_p(T_{02} - T_{0a})\eta \quad EQUATION\ 5.28$$

T_{02} is found taking $\gamma = 1.33$, $\frac{P_{02}}{P_{0a}} = 29$, $\eta = 0.9$ and the relation:

$$T_{02} = T_{0a} \left[\frac{\left(\frac{P_{02}}{P_{0a}} \right)^{\frac{\gamma-1}{\gamma}} - 1}{\eta} + 1 \right] = 621.711K \quad EQUATION\ 5.29$$

And using the definition of C_p it inside the gas turbine:

$$C_p = \frac{\gamma R}{\gamma - 1} = 1156.7 \frac{J}{kgK} \quad EQUATION\ 5.30$$

$$Total\ Power = 1.092e^8W \quad EQUATION\ 5.31$$

To find the power loss from the same mass flow as the SJA uses a ratio of total mass flow rates is used with $\dot{m}_{Core} = 57 \frac{kg}{s}$:

$$\frac{\dot{m}_{SJA}}{\dot{m}_{Core}} = 8.3e^{-11} \quad EQUATION\ 5.32$$

$$Power\ Loss = 8.3e^{-11} * Total\ Power = 9.06e^{-3}W \quad EQUATION\ 5.33$$

This means that the power loss by the turbine for a bleed air system is much less than the power required for actuating and heating the SJA. This first order calculation does not account for the added weight due to ducting for the bleed air and the generator to pump the bleed air into the ducts which reduces the available power for thrust. So while it will not be worth the loss of power to install the SJA's solely for the purpose of anti-icing, the chamber can be heated on already installed SJA's for a comparable power loss as a bleed air system.

5.7 PICCOLO TUBE SIMULATION

A piccolo tube is a numerical model for the popular Thermal bleed air anti-ice system. A Piccolo tube numerical analysis was performed in FENSAP-ICE for the same freestream conditions as for the wedge to acquire the power requirement for this anti-icing system. **Error! Reference source not found.** shows the velocity and temperature contours for the interior part of the Piccolo tube as computed by the FENSAP flow solver.

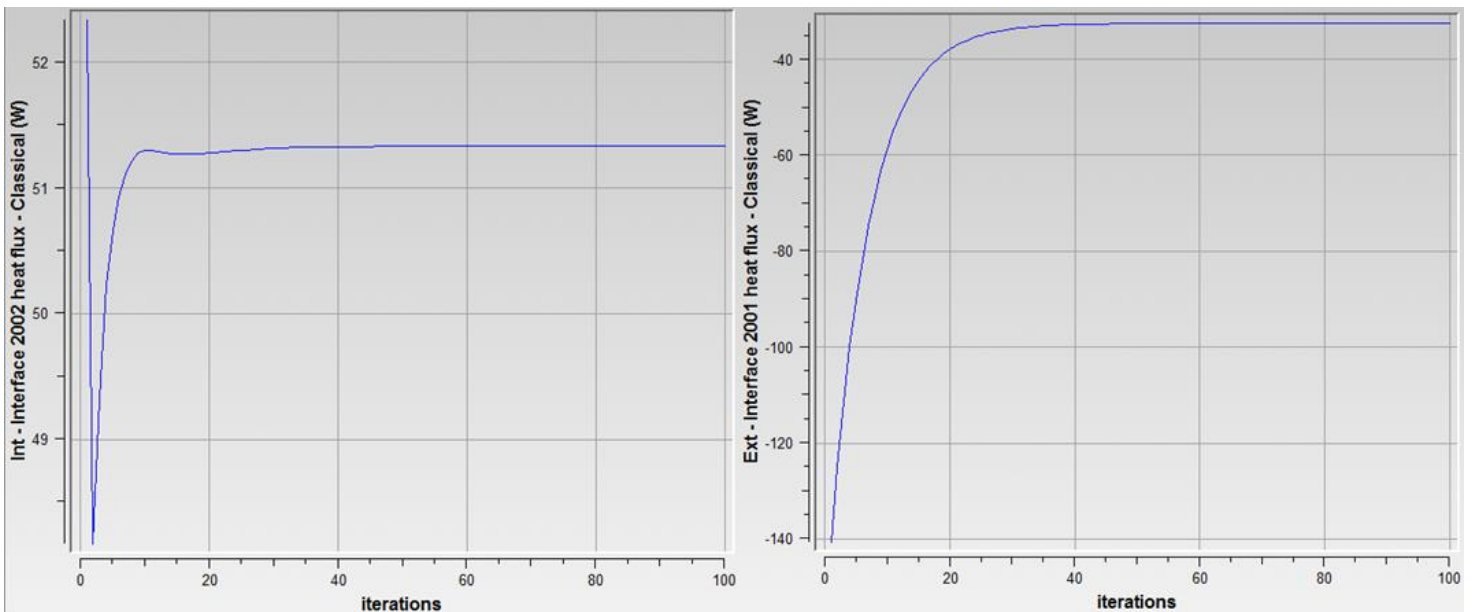


Figure 66: CHT3D convergence history for heat flux for Internal and External piccolo tube

The maximum heat between external and internal interface is approximately 51.3Watts from Figure 66. The span of the piccolo tube in this simulation is 20mm. Therefore the power per area for piccolo tube is;

$$\text{Surface Area for Piccolo Tube} = 20\text{mm} * 96\text{mm} = 1920\text{mm}^2 \quad \text{EQUATION 5.344}$$

$$\text{Power/Surface Area for Piccolo Tube} = \frac{51.3\text{W}}{1920\text{mm}^2} = 0.0267\text{W/mm}^2 \quad \text{EQUATION 5.355}$$

Using dimensions from Rizzetta.et.al [28], the width of a SJA is 15mm. The power per area for the six SJA is;

$$\text{Surface Area for Wedge} = 15\text{mm} * 96\text{mm} = 810\text{mm}^2 \quad \text{EQUATION 5.366}$$

$$\text{Power/Span for SJA} = \frac{6 * 1.1526\text{W}}{810\text{mm}^2} = 0.001422\text{W/mm}^2 \quad \text{EQUATION 5.377}$$

For this numerical calculation the six heated SJA's require less power than the Piccolo tube for the same freestream conditions. This may be a more accurate representation of the difference in power draw between the two methods because the previous analytical results used simple adiabatic and isentropic equations. The numerical simulation did not use these assumptions and as such offers a more correct result.

CHAPTER 6: CONCLUSION

The current work introduced a new method of efficient icing control using an array of thermally activated synthetic jet actuators (SJAs) embedded on an aircraft surface exposed to ice accretion due to super-cooled upstream flow.

In a benchmark test study, six SJAs were distributed on a 15° wedge subject to an upstream flow with Mach number $M=0.1$ and temperature $T=-20^\circ\text{C}$. The prescribed amplitudes of the time-periodic jet velocities at the bottoms of the actuators' orifices were 25m/s produced by SJAs with orifice diameters and heights of 0.5mm and actuation frequencies of 1000Hz. The actuators were distributed 5mm apart along the wedge with length $L=54\text{mm}$.

The effects of SJA actuation with and without jet heating on ice accretion were studied numerically using NTI's FENSAP-ICE software. Compared to the baseline case of non-heated, non-actuated SJAs, the obtained results revealed a notable impact of actuation observed for small droplet MVD even without added heat. This was presumably caused by the actuated jets diverting the upstream flow away from the wedge surface thus reducing the droplet impingement and accumulation on the surface and partially inhibiting the ice accretion process. The impact was lessened with larger droplet MVD's. Furthermore, for the case of heated actuated SJAs, the jet-induced convective heat transfer was able to almost completely preclude any ice formation on the wedge surface.

The parametric study investigating the effects of droplet distribution, SJA chamber temperature, droplet MVD and freestream temperature was performed. Only the temperature of the SJA chamber induced any significant effects on ice accretion on the surface of the wedge. The heated air expelled from the SJA's evaporated the impinging droplets and prevented and

significant ice accretion for the remaining parameters studied. The introduced icing control approach appears highly promising and will be further investigated in the subsequent parametric studies.

6.1 FUTURE WORK

A parametric study will be conducted for optimizing the number of SJA's per unit area of a surface needed for total anti-ice purposes. Different orifice geometries will be analyzed to minimize or prevent the impinging droplets and runback water from entering the SJA chamber. The current study will be implemented into an airfoil and nacelles the anti-ice performance will be characterized.

REFERENCES

1. David, Landsberg. *Aircraft Icing*. 2008. AOPA, Frederick, MD
2. Mingione, Giuseppe, and Massimo Barocco. *Flight in Icing Conditions Summary*. 1997. French DGAC.
3. Politovich, MK. *Aircraft Icing*. 2003. Elsevier Science Ltd.
4. Verdin, P. (2007). An automatic multi-stepping approach to aircraft ice prediction.
5. *Aircraft Icing Handbook*
6. "Supercooled Water Droplets." *SKYbrary* -. N.p., n.d. Web. 6 Feb. 2013. <http://www.skybrary.aero/index.php/Supercooled_Water_Droplets>.
7. Charlson, Robert J.; Lovelock, James; Andreae, Meinrat O.; Warren, Stephen G. (1987). "Oceanic phytoplankton, atmospheric sulphur, cloud albedo and climate". *Nature* **326** (6114): 655–661. [Bibcode 1987Natur.326..655C](#)
8. "METEOROLOGY (Part II)." *Commercial Pilot Meteorology, Part 2, Langley Flying School*. N.p., n.d. Web. 6 Feb. 2013. <http://www.langleyflyingschool.com/Pages/CPGS_Meteorology_Part_2.html>.
9. Gent, R. W., Dart, N. P., Cansdale, J. T., Gent, R. W., Dart, N. P., & Cansdale, J. T. (2000). Aircraft icing. *Philosophical Transactions of the Royal Society of London. Series A: Mathematical, Physical and Engineering Sciences*, 358(1776), 2873-2911.
10. "Ice Accretion." *Extice Site*. N.p., n.d. Web. 7 Feb. 2013. <<http://extice.cira.it/project/proposal-summary/ice-accretion>>.
11. "Icing." *Icing*. N.p., n.d. Web. 7 Feb. 2013. <http://eumetrain.org/data/2/253/print_2.htm>.
12. "A Pilot's Guide to In-Flight Icing - Web Version." *A Pilot's Guide to In-Flight Icing - Web Version*. N.p., n.d. Web. 8 Feb. 2013. <http://aircrafticing.grc.nasa.gov/courses/inflight_icing/main.html>.
13. Goraj, Z. An Overview of the Deicing and Antiicing technologies with Prospects for the future. In *ICAS (International Congress of the Aeronautical Sciences)*, Warsaw *University of Technology* (p. 7).
14. "Newmerical Technologies Int. \hat{A} » FENSAP-ICE: In-flight Icing Simulation System." *Newmerical Technologies Int. \hat{A} » FENSAP-ICE: In-flight Icing Simulation System*. N.p., n.d. Web. 9 Feb. 2013. <<http://www.newmerical.com/index.php/products/fensap-ice-cfd-software/>>.
15. Bourgault, Y., Boutanios, Z., & Habashi, W. G. (2000). Three-dimensional Eulerian approach to droplet impingement simulation using FENSAP-ICE, Part 1: Model, algorithm, and validation. *Journal of aircraft*, 37(1), 95-103.
16. Bourgault, Y., Habashi, W. G., Dompierre, J., & Baruzzi, G. S. (1999). A finite element method study of Eulerian droplets impingement models. *International journal for numerical methods in fluids*, 29(4), 429-449.
17. POTAPCZUK, M. (1992). LEWICE/E: an Euler based ice accretion code.
18. Croce, G., De Candido, E., Habashi, W. G., Munzar, J., Aubé, M. S., Baruzzi, G. S., & Aliaga, C. (2010). FENSAP-ICE: Analytical Model for Spatial and Temporal Evolution of In-Flight Icing Roughness. *Journal of Aircraft*, 47(4), 1283-1289.

19. <http://www.collectionscanada.gc.ca/obj/thesescanada/vol2/QMM/TC-QMM-95154.pdf>
20. Myers, T. G. (2001). Extension to the messinger model for aircraft icing. *AIAA journal*, 39(2).
21. Beaugendre, H., Morency, F., & Habashi, W. G. (2003). FENSAP-ICE's three-dimensional in-flight ice accretion module: ICE3D. *Journal of aircraft*, 40(2), 239-247.
22. Croce, G., Beaugendre, H., & Habashi, W. G. (2002). CHT3D: FENSAP-ICE conjugate heat transfer computations with droplet impingement and runback effects. *AIAA paper*, 386(4), 0.
23. Zhong, S., Jabbal, M., Tang, H., Garcillan, L., Guo, F., Wood, N., & Warsop, C. (2007). Towards the design of synthetic-jet actuators for full-scale flight conditions. *Flow, turbulence and combustion*, 78(3), 283-307.
24. "Inviscid Flow Past a Semi-Infinite Wedge." *Inviscid Flow Past a Semi-Infinite Wedge*. N.p., n.d. Web. 11 Feb. 2013.
<<http://farside.ph.utexas.edu/teaching/336l/fluidhtml/node67.html>>.
25. Crowther, Bill. "Synthetic Jet Actuators." February 22, 2012,
http://www.billcrowther.net/research/Flow_control/FMSJA/FM_SJAs.html
26. Nakhla, H., Bourlier, A., Nguyen, L., Bhatt, S., Brodnick, J., Golubev, V., (2011), "High-Accuracy Simulations of Synthetic Jets for Low-Re Flow Control." AIAA 2011-469, 49th AIAA Aerospace Science Meeting and Exhibit, Orlando, January 2011.
27. Jones, Sharon Monica, et al. "Subsonic Aircraft Safety Icing Study." (2008).
28. Rizzetta, Donald P., Michael J. Stanek, and Miguel R. Visbal. "Numerical investigation of synthetic-jet flowfields." *AIAA journal* 37.8 (2012).

APPENDIX

A.1 VALIDATION OF NUMERICAL RESULTS TO ANALYTICAL MODEL

The analytical solution for a flow over a wedge begins with considering an incompressible, irrotational flow in two-dimensional cylindrical coordinates. The generalized wedge angle is $\alpha\pi$, Figure 67, and the boundary conditions for the wedge say that a streamline will always be tangent to the wedge surface [24]:

$$\psi\left(r, \frac{\alpha\pi}{2}\right) = \psi\left(r, 2\pi - \frac{\alpha\pi}{2}\right) = 0,$$

And that the streamline will meet the apex of the wedge and split into two portions along the top and bottom of the wedge:

$$\psi(r, \pi) = 0.$$

Laplace's equation two-dimensional cylindrical coordinates will be solved with the above boundary conditions.

$$\frac{1}{r} \frac{\partial}{\partial r} \left(r \frac{\partial \psi}{\partial r} \right) + \frac{1}{r^2} \frac{\partial^2 \psi}{\partial \theta^2} = 0$$

Which can be shown to give:

$$\psi(r, \theta) = \frac{A}{1+m} r^{1+m} \sin[(1+m)(\pi - \theta)], \quad m = \frac{\alpha}{2 - \alpha}$$

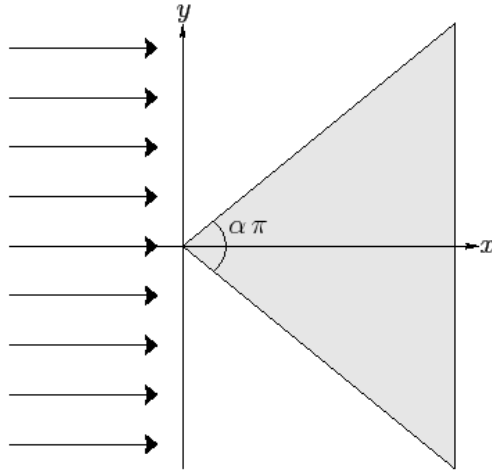


FIGURE 67: INCOMPRESSIBLE AND IRROTATIONAL FLOW PAST A WEDGE [35]

For the cases here, the total wedge angle is 30° which gives $\alpha = \frac{30}{180} rad$. A simple MATLAB script was created to plot the streamlines on a specified grid and is shown in Figure 68.

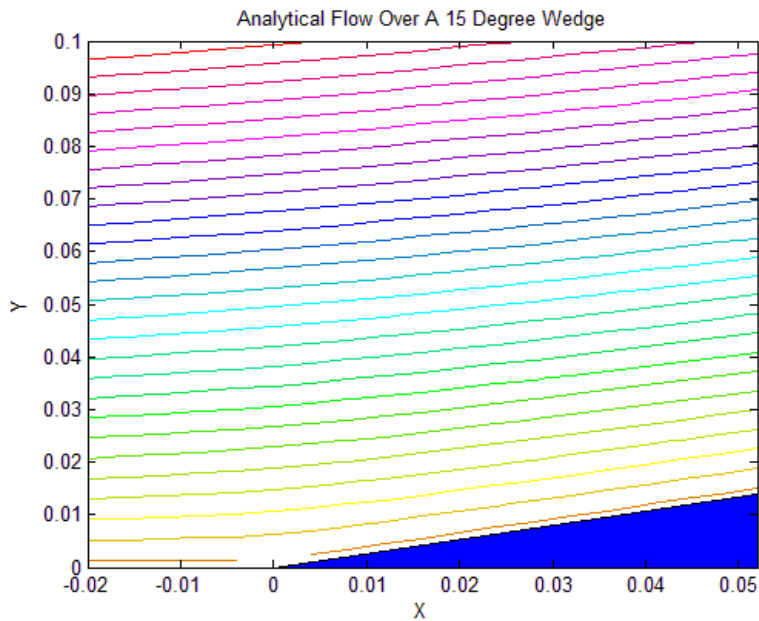


FIGURE 68: ANALYTICAL SOLUTION FOR STREAMLINES

A.2 CASE D, SNAPSHOT 2 FLOW COMPARISON WITH PREVIOUS FLUENT RESULTS

A part of this work was previously presented at the AIAA 2013 ASM using FLUENT as the flow solver instead of the FENSAP flow solver. The velocity fields for both results when the SJA is fully ejecting is shown in Figure 69 with the FENSAP results on the left and the FLUENT results on the right. Both plots contour levels are set to range from 0m/s to 50m/s with red being higher. Each is also displayed in a different postprocessor software with the FENSAP results displayed using NTI's VIEWMERCAL software and the FLUENT results displayed using CFX-Post. Upon inspection of the flow fields there are some differences in contour shape between the solutions with FENSAP having the contours that rise farther than with FLUENT. There are also some small differences in the magnitudes of the velocity field with the FLUENT results being slightly higher overall compared to the FENSAP results. Near the SJA's the actuation patterns for both results are very similar with the effect of the actuation increasingly modulating the flow farther back on the wedge.

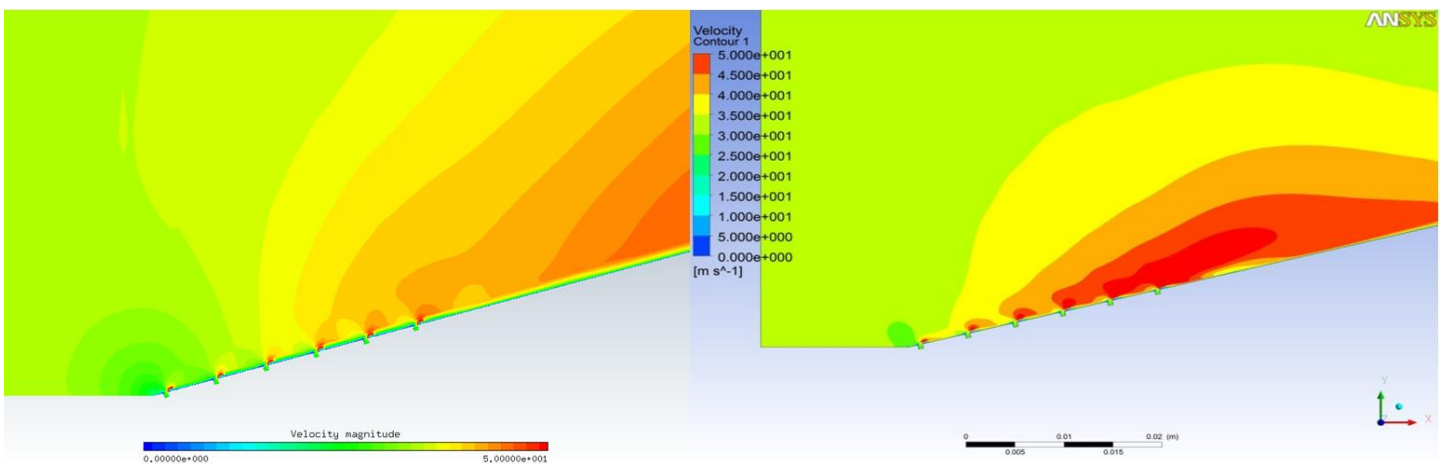


FIGURE 69: VELOCITY FLOW FIELD COMPARISON. FENSAP (LEFT) FLUENT (RIGHT)

The temperature fields for both cases are shown in Figure 70 and show many similarities in the general flow patterns over the top of the wedge. The FLUENT results do not show the small vortex bubble structure just rear of each SJA orifice that is shown in the FENSAP temperature field.

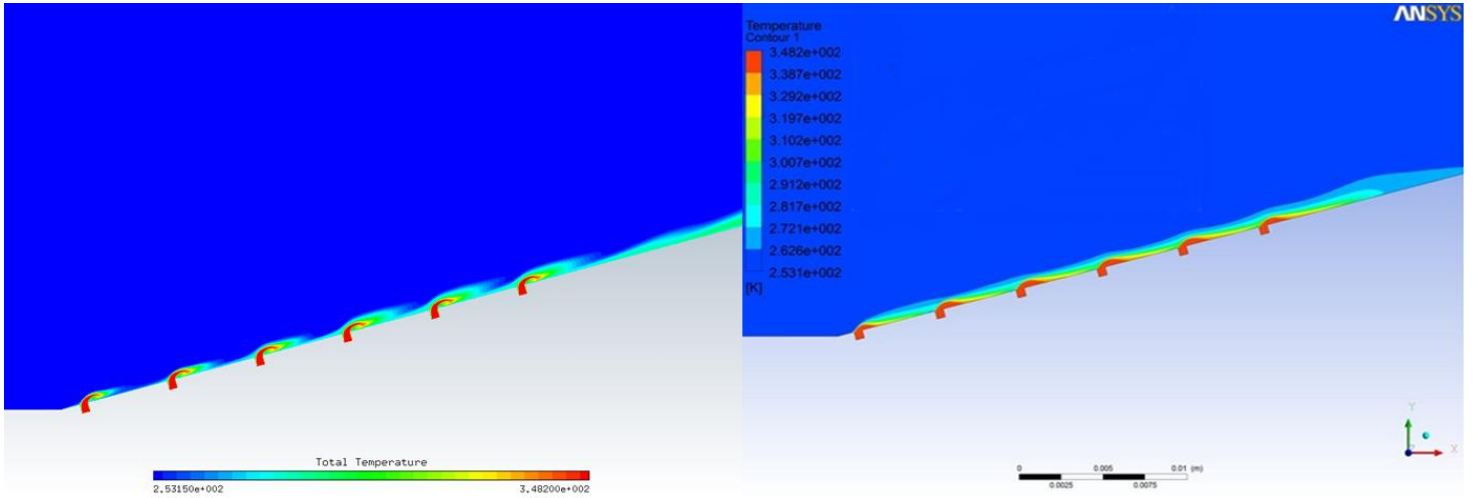


FIGURE 70: TEMPERATURE FIELD COMPARISON. FENSAP (LEFT) FLUENT (RIGHT)

Both the FENSAP and FLUENT results are overall very similar to each other where any small discrepancies can be attributed to the different methods that each flow solver uses to calculate the flow field.

A.3 ADDITIONAL RESULTS FROM CHAPTER 5

CASE D: DROPLET DISTRIBUTION COMPARISON

SNAPSHOT 1

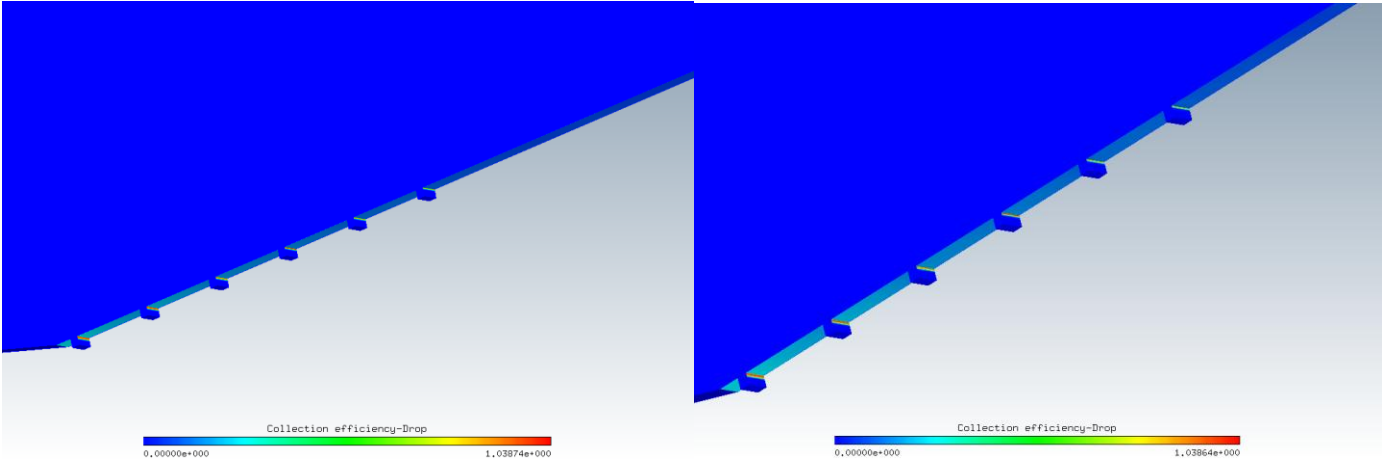


FIGURE 71: COLLECTION EFFICIENCY (MONODISPERSE LEFT, LANGMUIR RIGHT)

SNAPSHOT 2

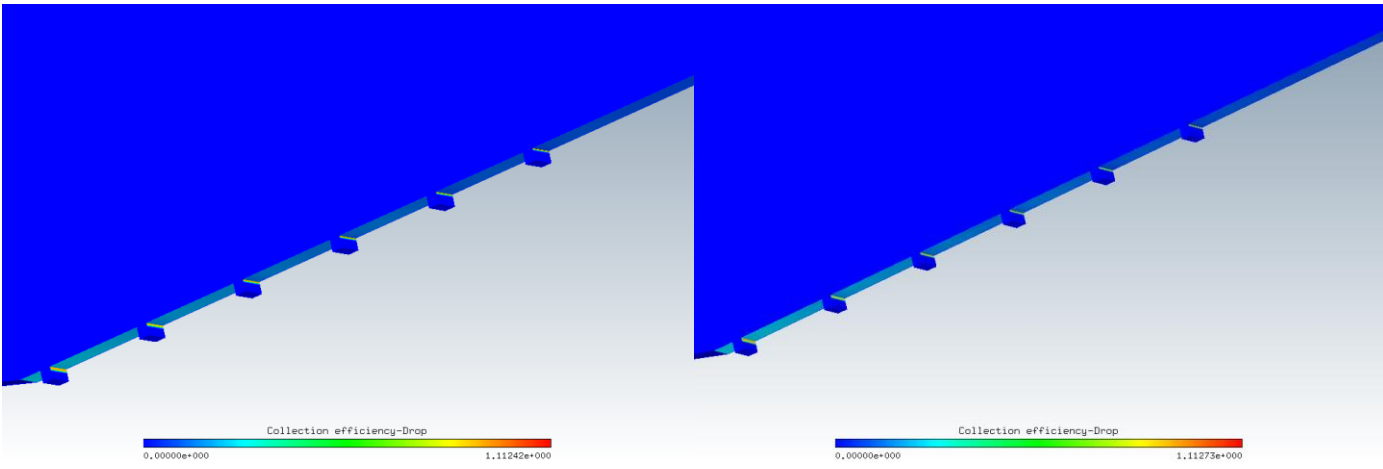


FIGURE 72: COLLECTION EFFICIENCY (MONODISPERSE LEFT, LANGMUIR RIGHT)

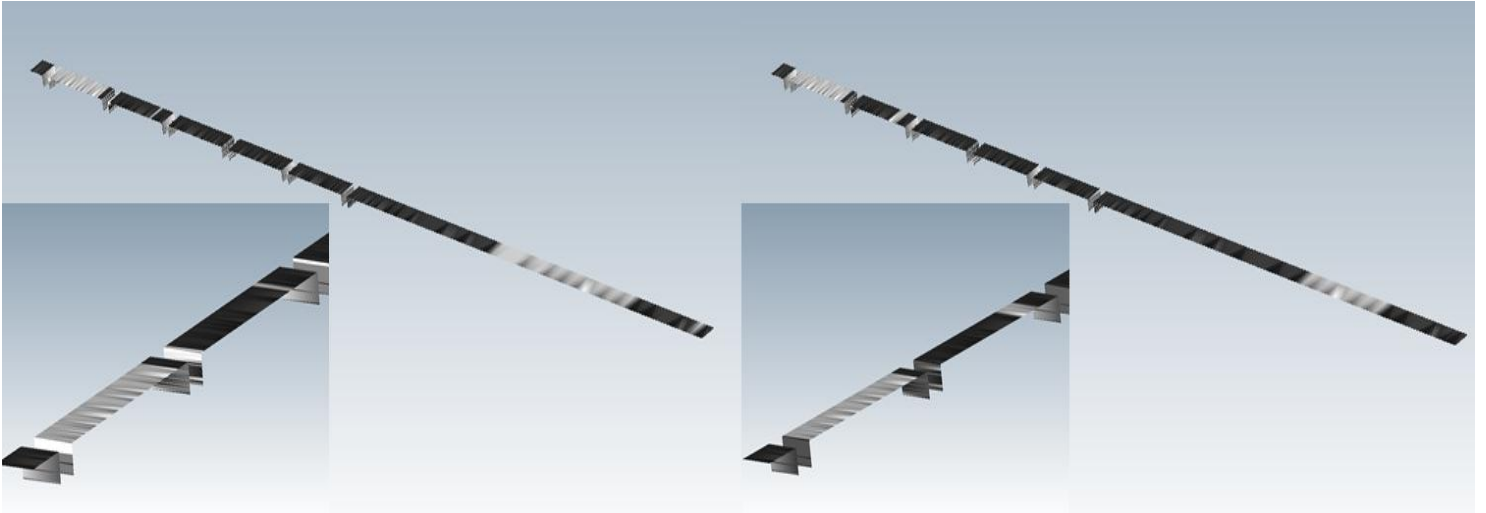


FIGURE 73: ICE ACCUMULATION (MONODISPERSE LEFT, LANGMUIR RIGHT)

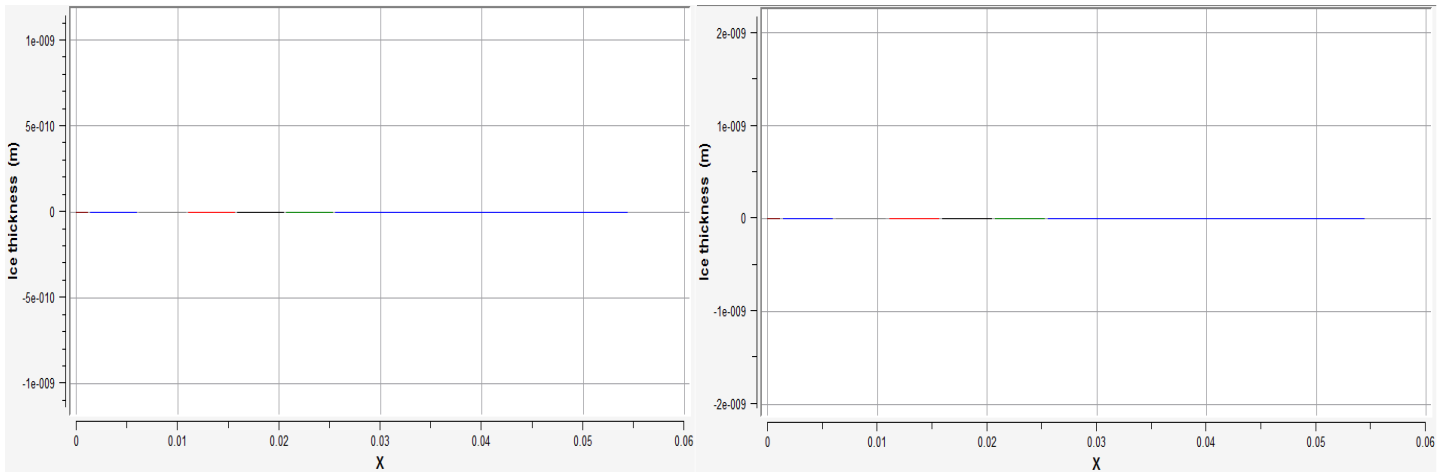


FIGURE 74: ICE THICKNESS PLOT (MONODISPERSE LEFT, LANGMUIR RIGHT)

SNAPSHOT 3

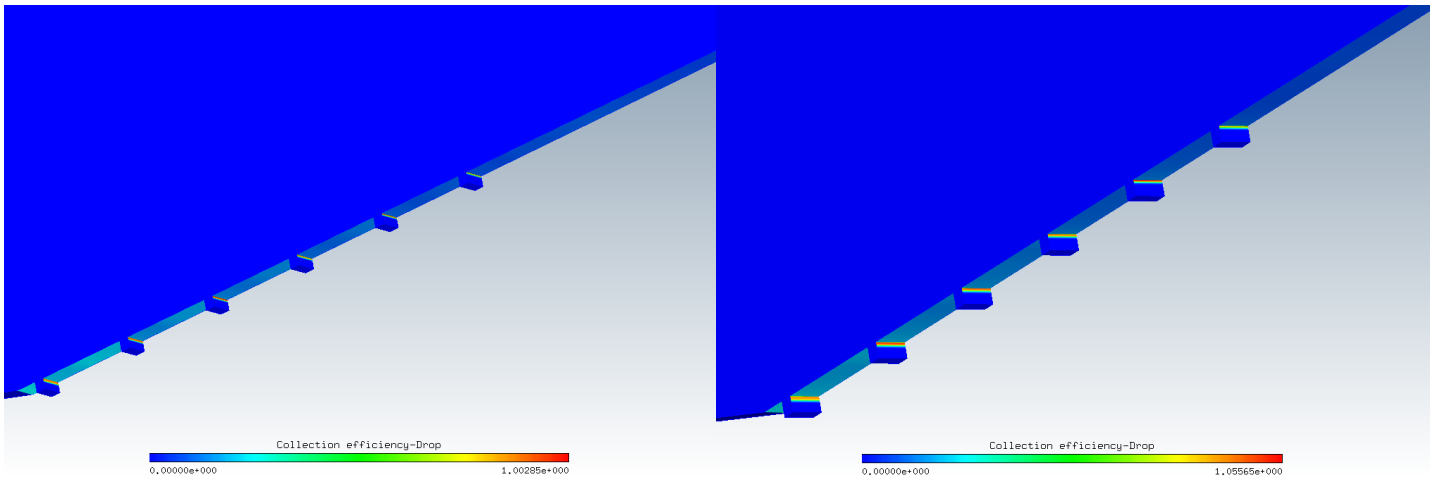


FIGURE 75: COLLECTION EFFICIENCY (MONODISPERSE LEFT, LANGMUIR RIGHT)

SNAPSHOT 4

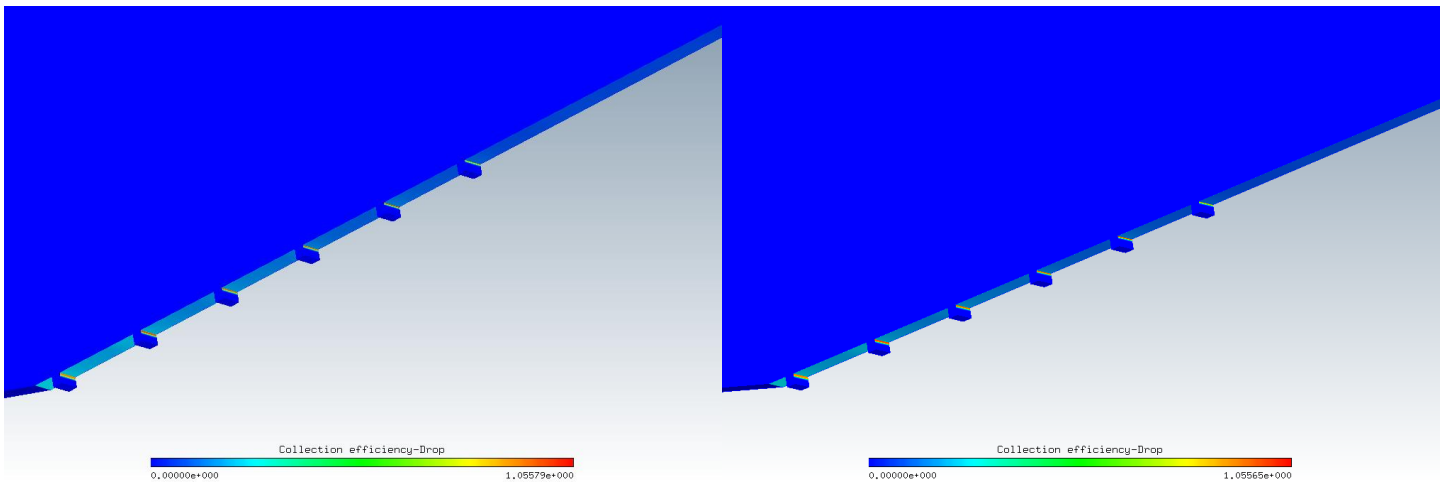


FIGURE 76: COLLECTION EFFICIENCY (MONODISPERSE LEFT, LANGMUIR RIGHT)



FIGURE 77: ICE ACCUMULATION (MONODISPERSE LEFT, LANGMUIR RIGHT)

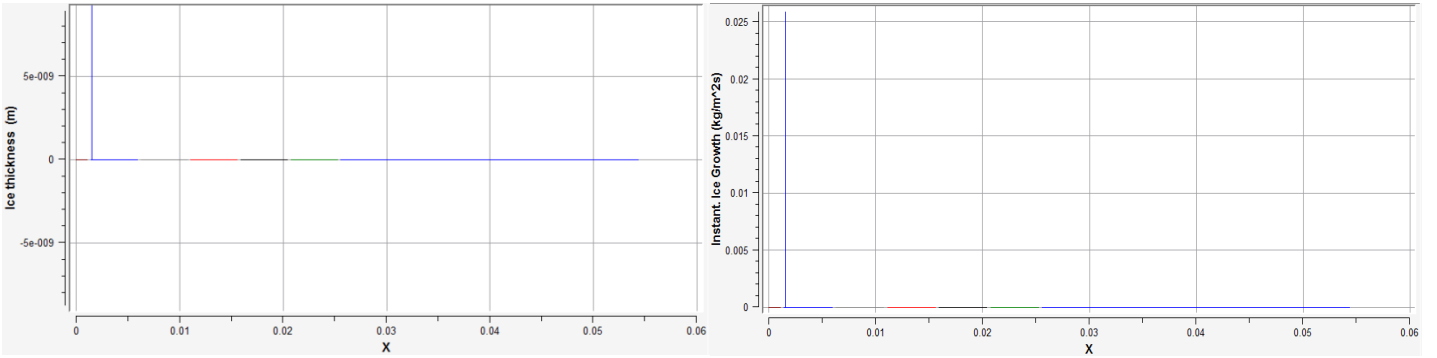


FIGURE 78: ICE THICKNESS PLOT (MONODISPERSE LEFT, LANGMUIR, RIGHT)

CASE D: SJA TEMPERATURE COMPARISON

SNAPSHOT 2

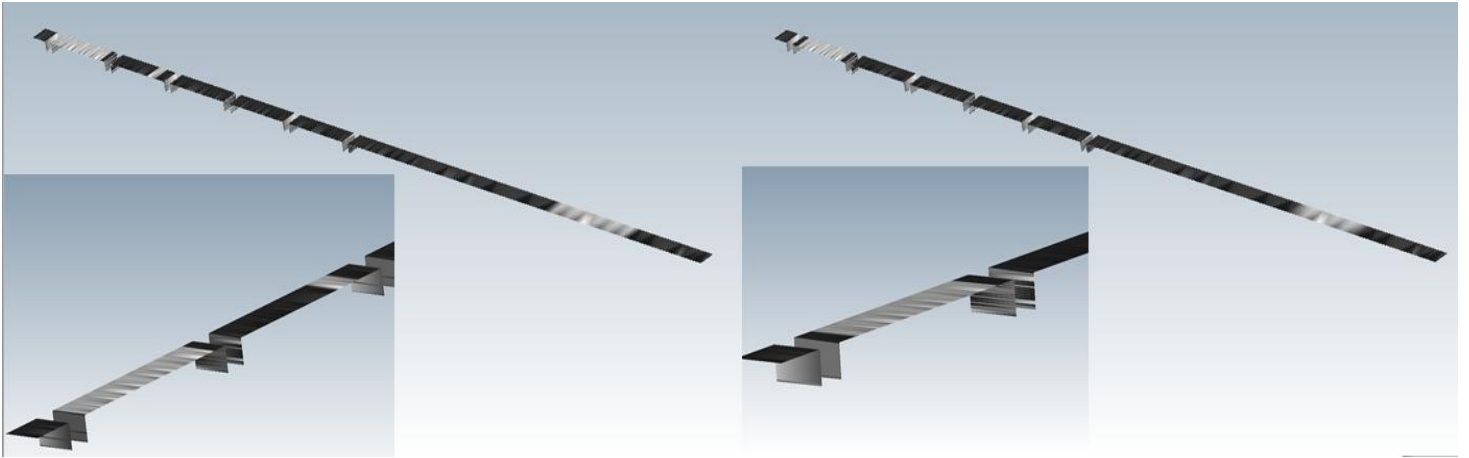


FIGURE 79: ICE ACCUMULATION (INLET TEMPERATURE: 75C LEFT, 100C RIGHT)

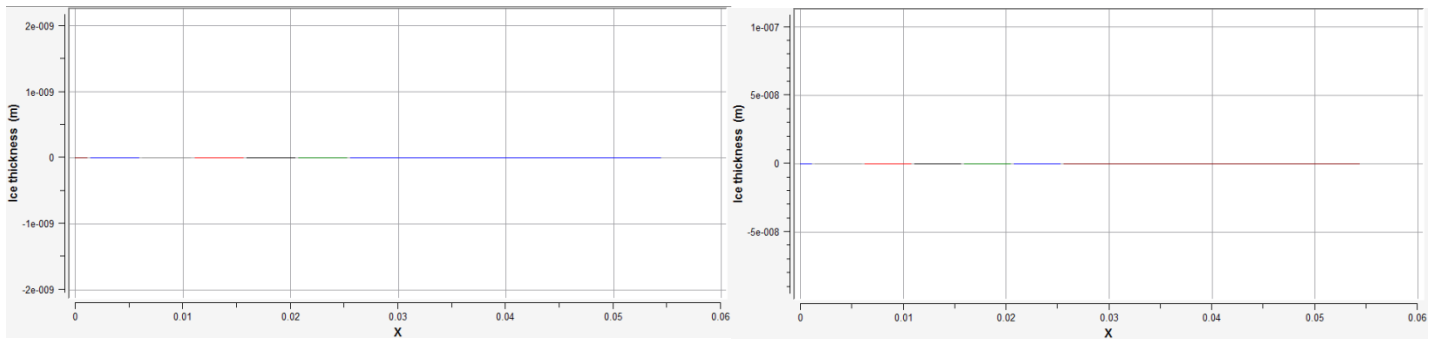


FIGURE 80:ICE THICKNESS PLOT (INLET TEMPERATURE: 75C LEFT, 100C RIGHT)

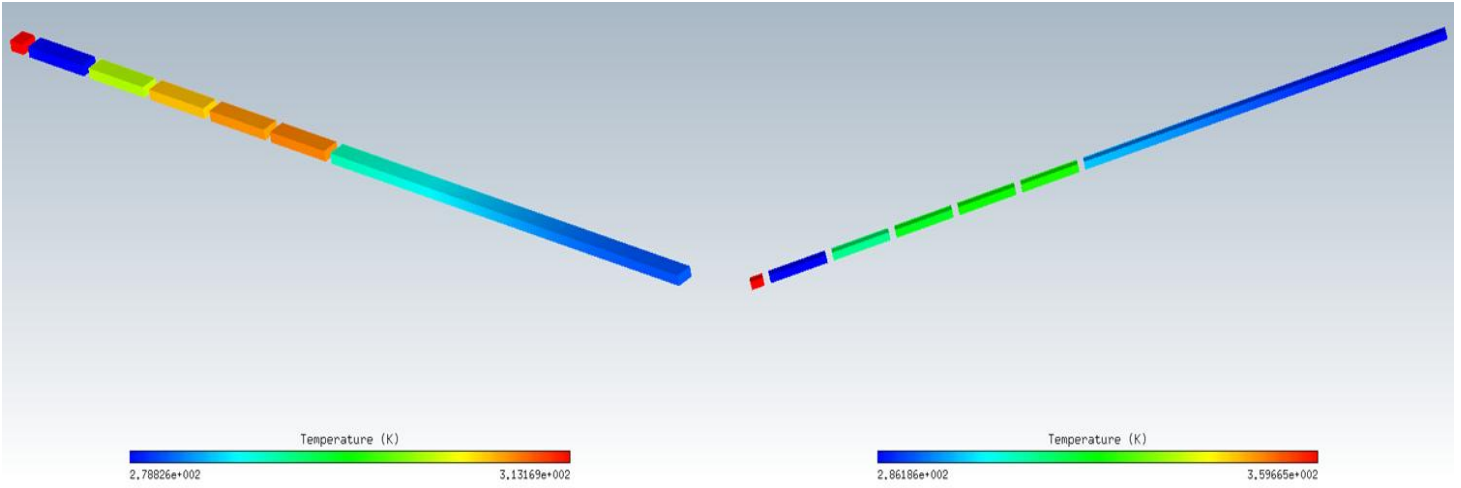


FIGURE 81: :SOLID TEMPERATURE (INLET TEMPERATURE: 75C LEFT, 100C RIGHT)

SNAPSHOT 4

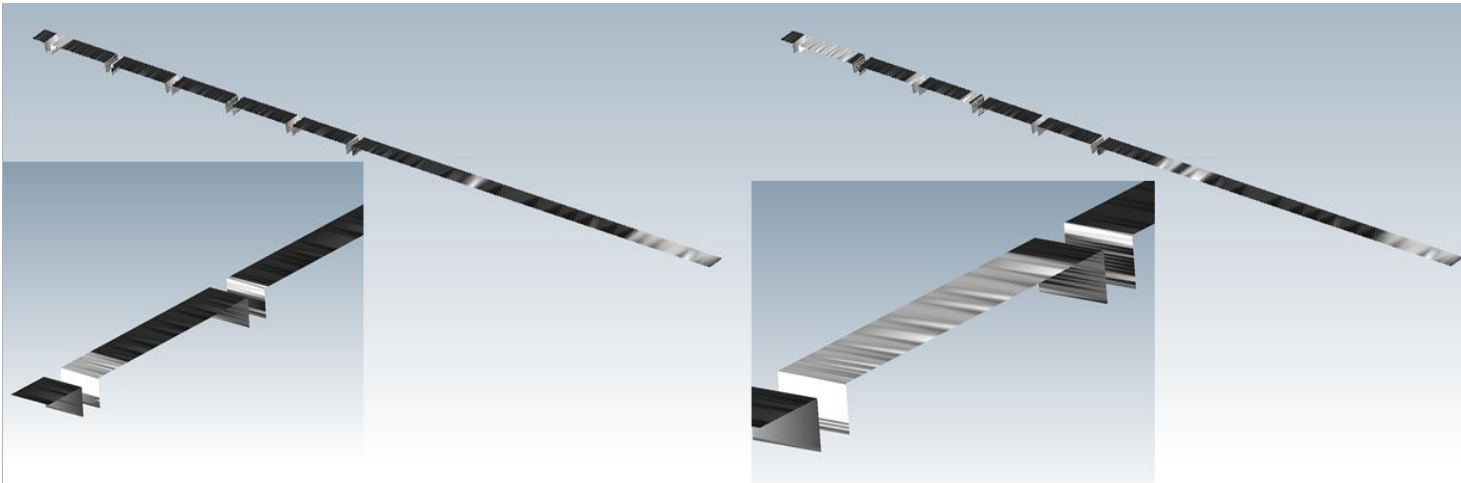


FIGURE 82:ICE ACCUMULATION (INLET TEMPERATURE: 75C LEFT, 100C RIGHT)

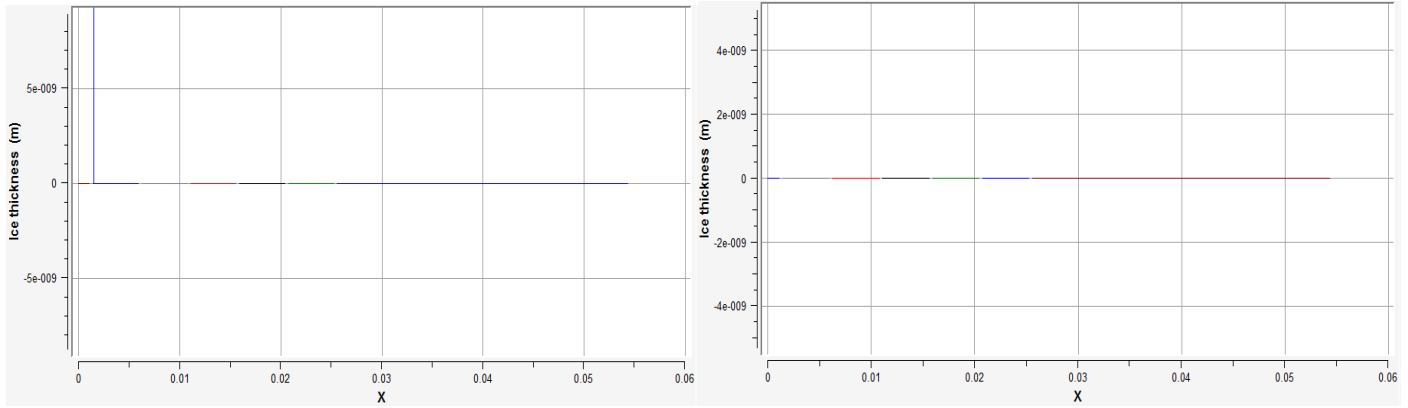


FIGURE 83:ICE THICKNESS PLOT (INLET TEMPERATURE: 75C LEFT, 100C RIGHT)

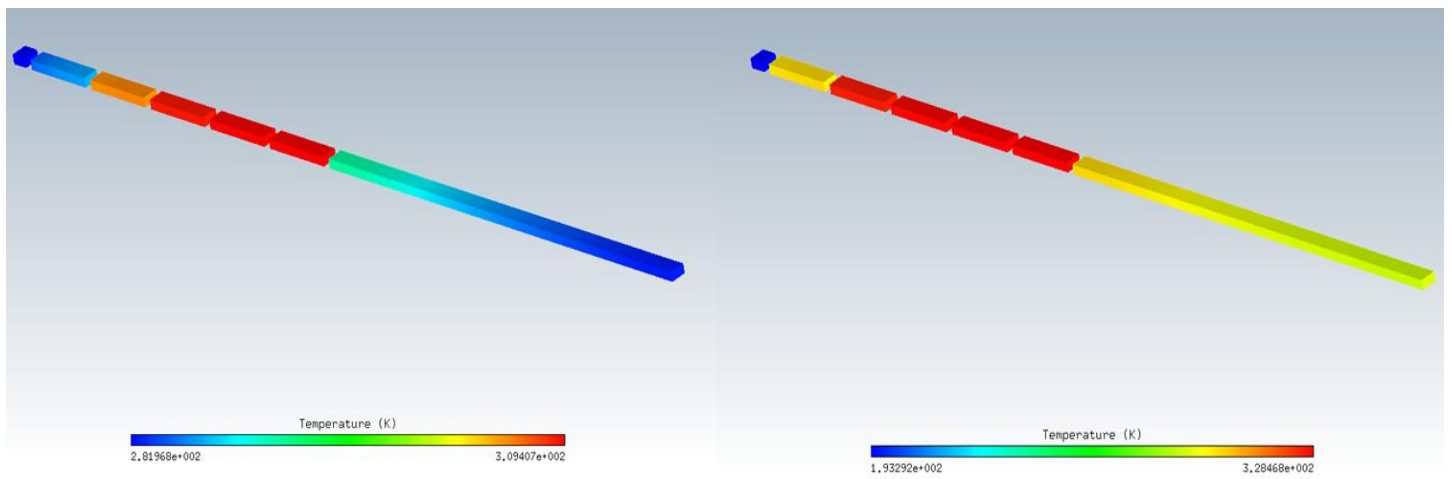


FIGURE 84: SOLID TEMPERATURE (INLET TEMPERATURE: 75C LEFT, 100C RIGHT)

CASE D: SSD VS SLD

SNAPSHOT 1

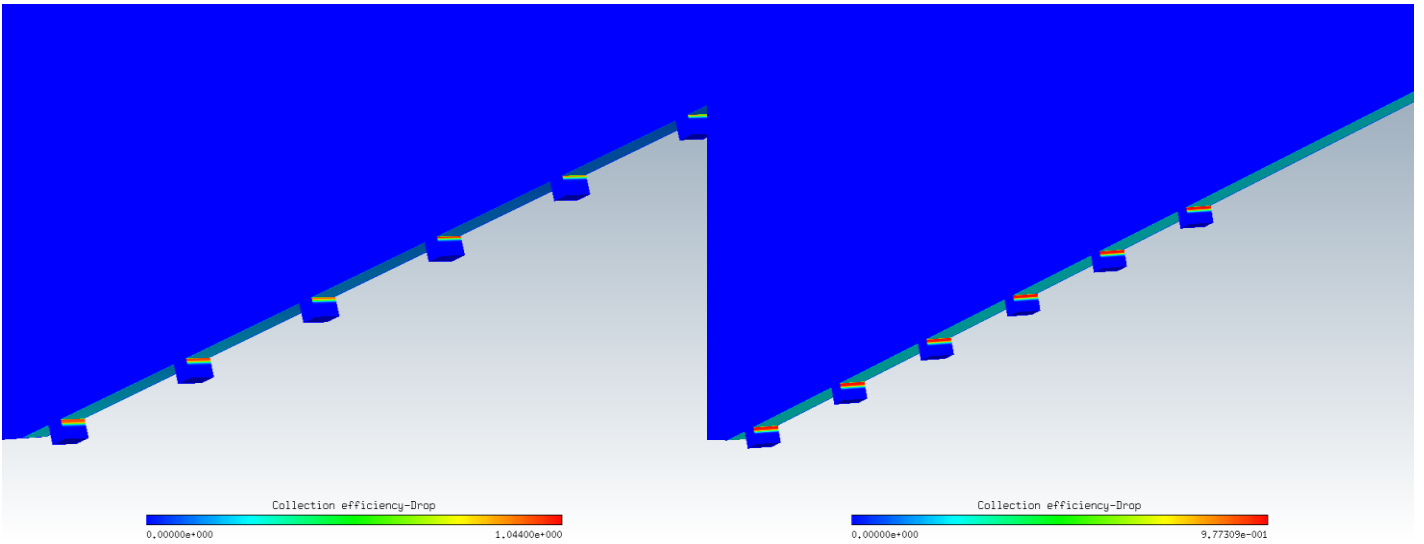


FIGURE 85: COLLECTION EFFICIENCY (SSD LEFT, SLD RIGHT)

SNAPSHOT 2

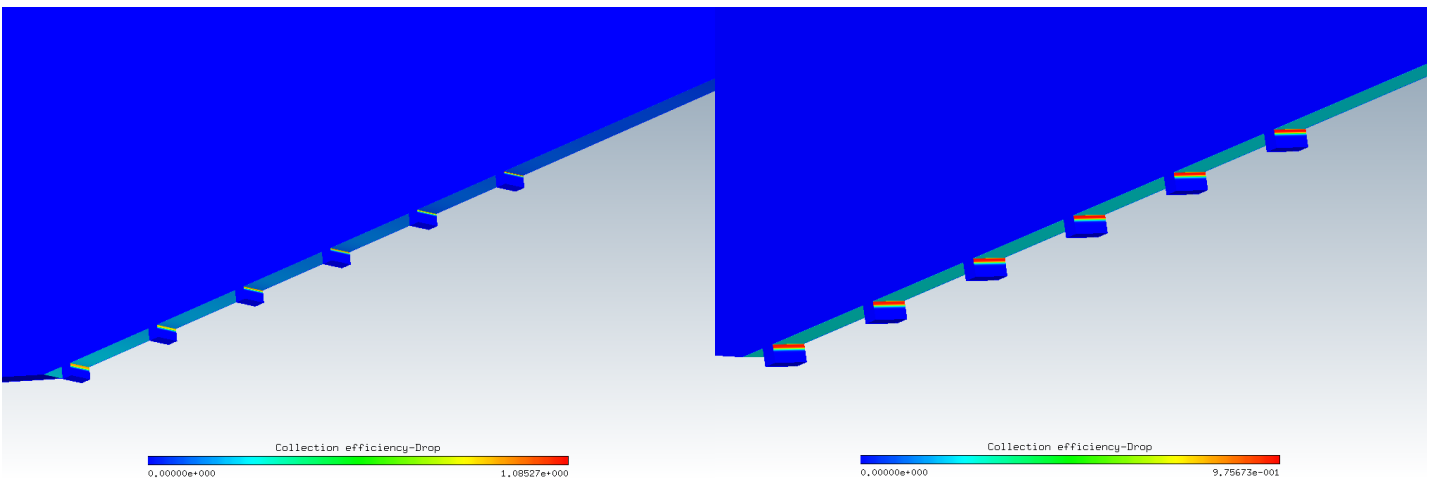


FIGURE 86: COLLECTION EFFICIENCY (SSD LEFT, SLD RIGHT)

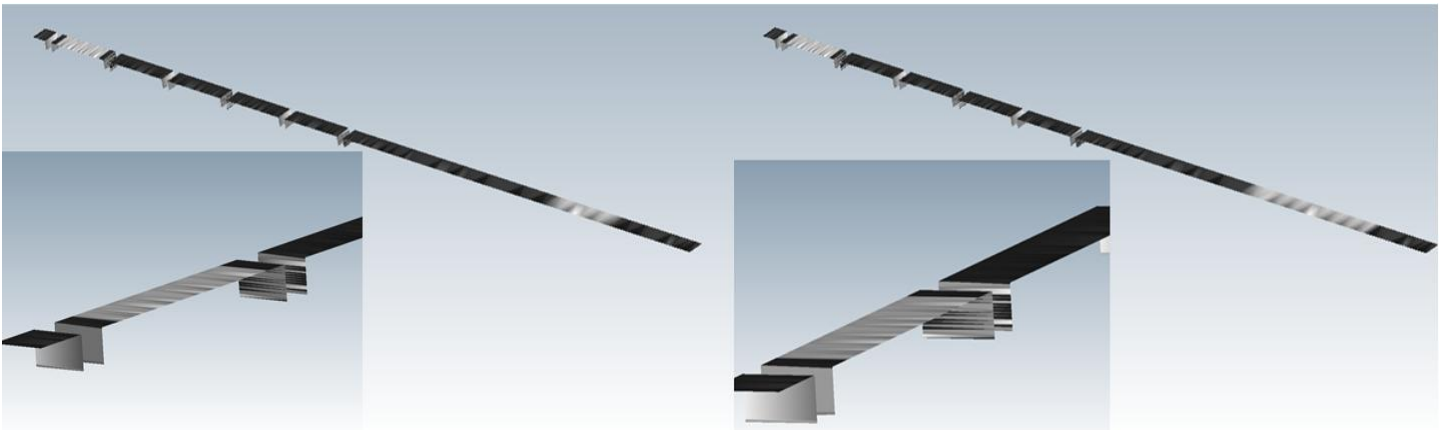


FIGURE 87: ICE ACCUMULATION (SSD LEFT, SLD RIGHT)

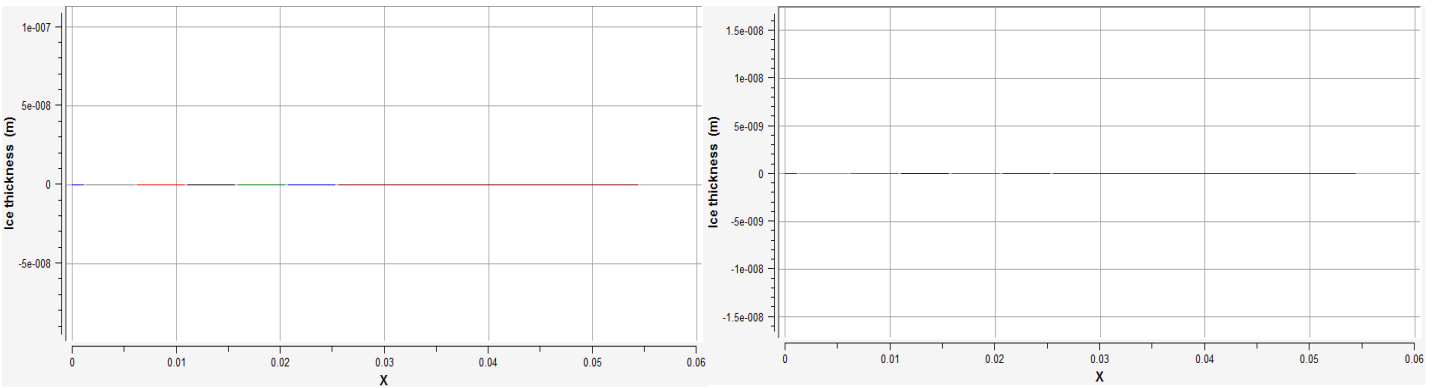


FIGURE 88: ICE THICKNESS PLOT (SSD LEFT, SLD RIGHT)

SNAPSHOT 3

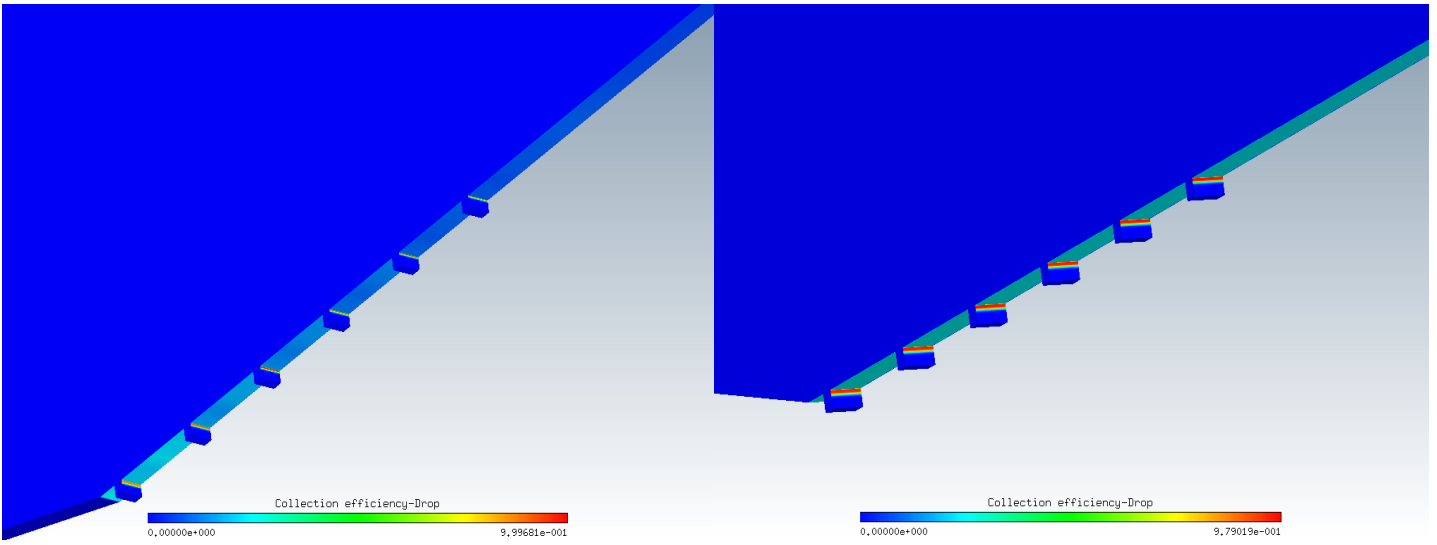


FIGURE 89: COLLECTION EFFICIENCY (SSD LEFT, SLD RIGHT)

SNAPSHOT 4

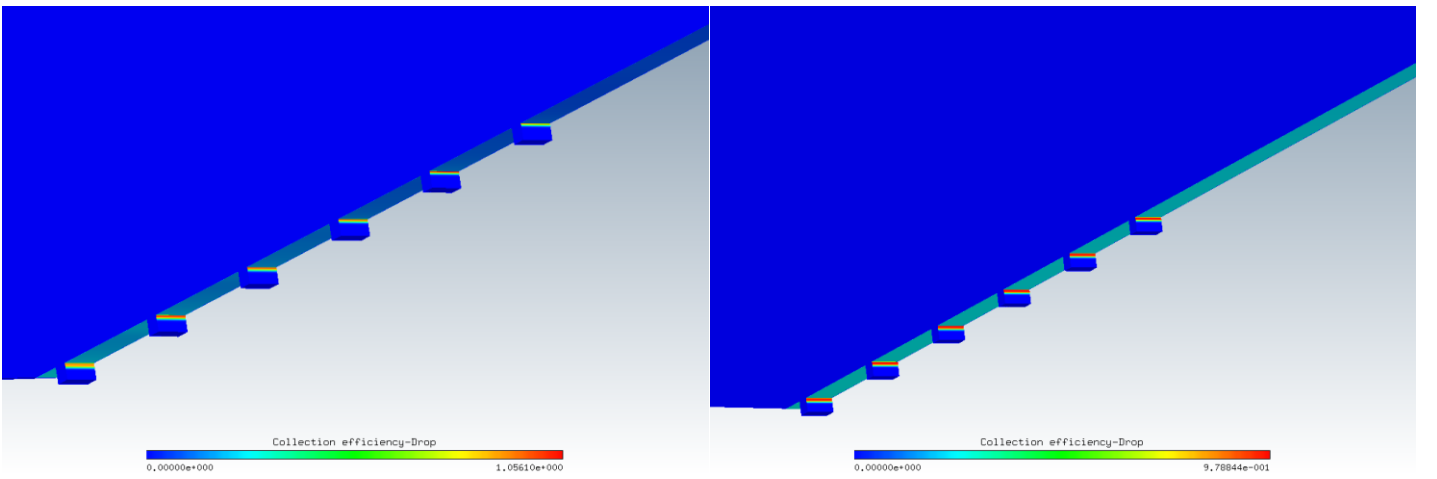


FIGURE 90: COLLECTION EFFICIENCY (SSD LEFT, SLD RIGHT)

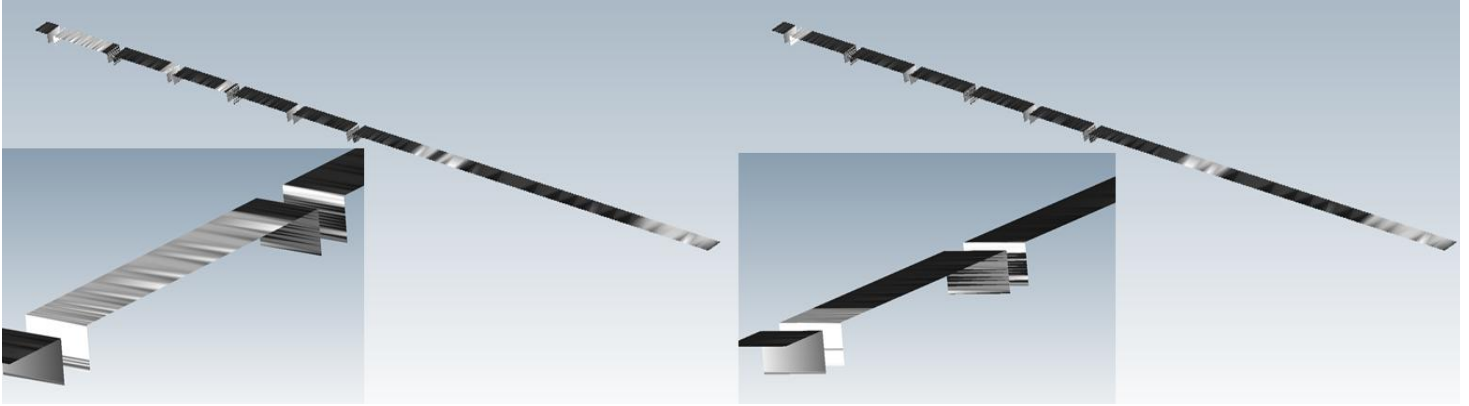


FIGURE 91: ICE ACCUMULATION (SSD LEFT, SLD RIGHT)

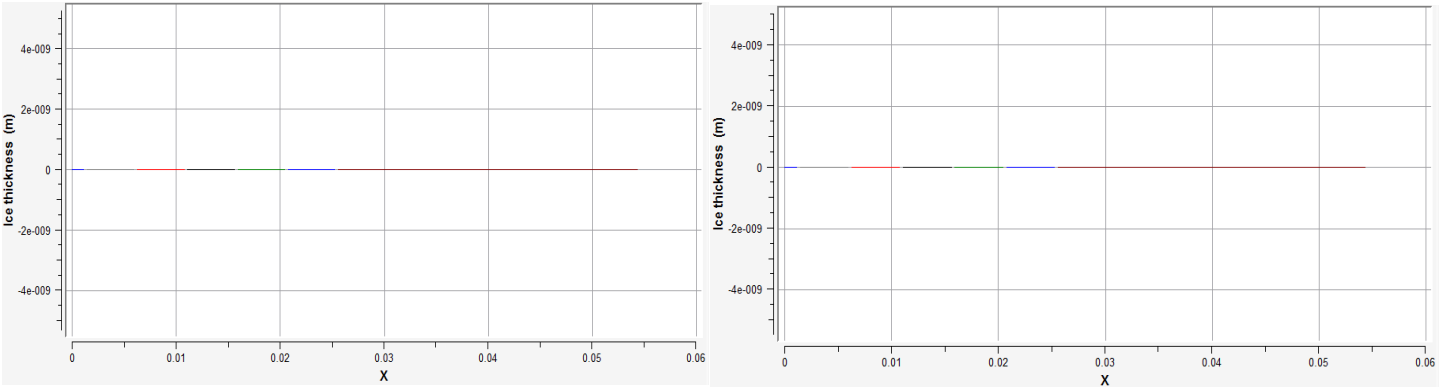


FIGURE 92: ICE THICKNESS PLOT (SSD LEFT, SLD RIGHT)

CASE D: FREESTREAM TEMPERATURE COMPARISON

SNAPSHOT 2

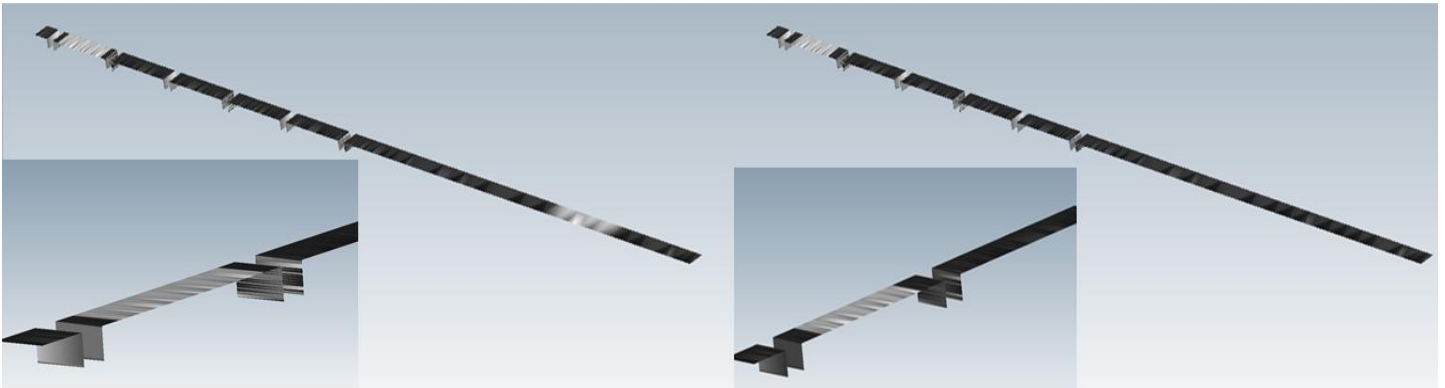


FIGURE 93: ICE ACCUMULATION (FREESTREAM TEMPERATURES OF -20C LEFT, -10 RIGHT)

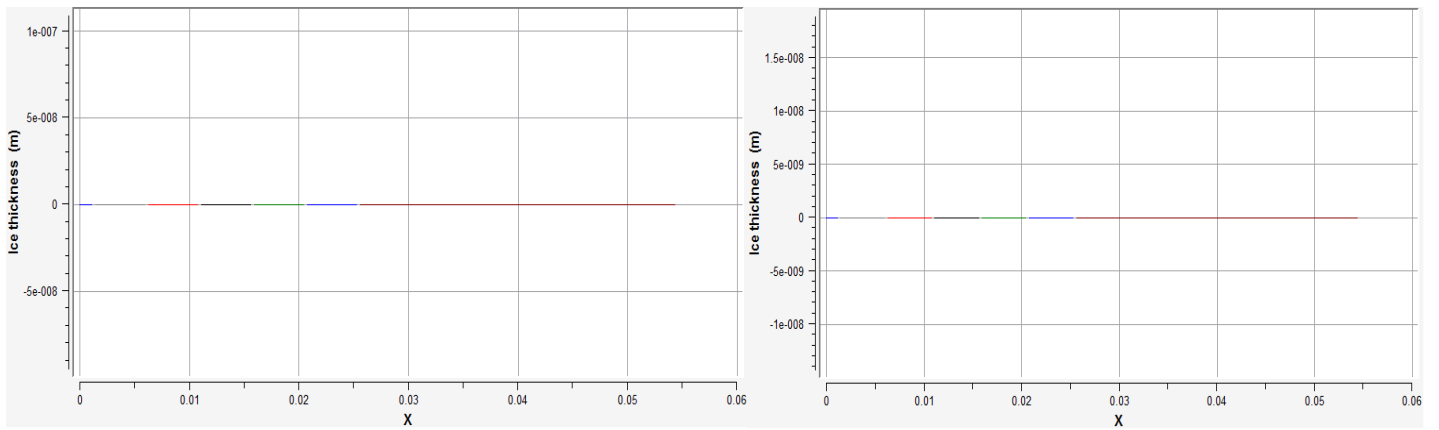


FIGURE 94: ICE THICKNESS PLOT (FREESTREAM TEMPERATURES OF -20C LEFT, -10 RIGHT)

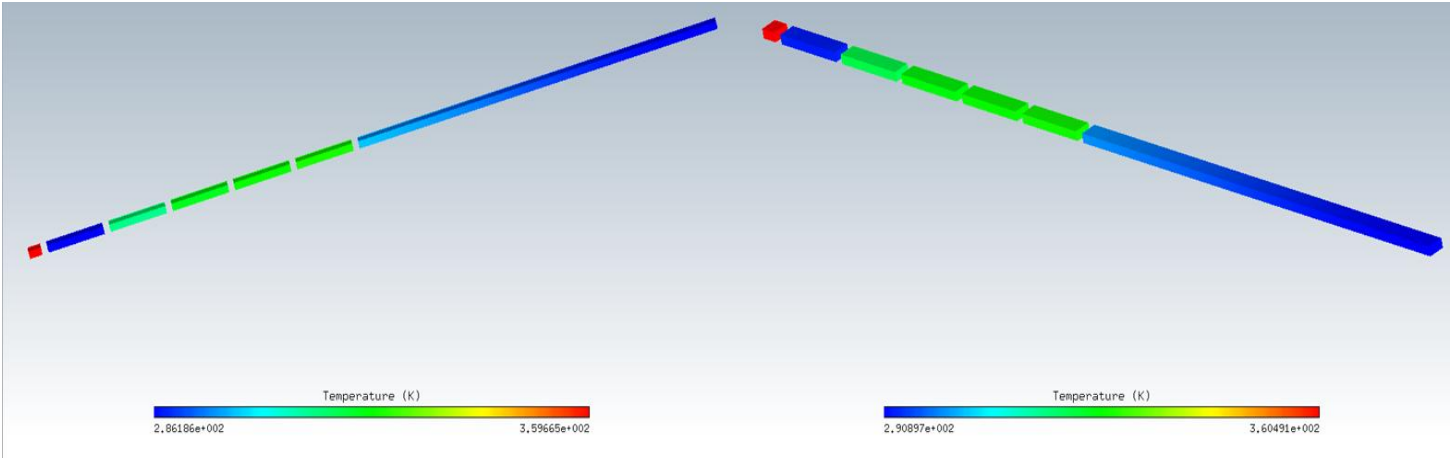


FIGURE 95: SOLID TEMPERATURE (FREESTREAM TEMPERATURES OF -20C LEFT, -10 RIGHT)

SNAPSHOT 4



FIGURE 96: ICE ACCUMULATION (FREESTREAM TEMPERATURES OF -20C LEFT, -10 RIGHT)

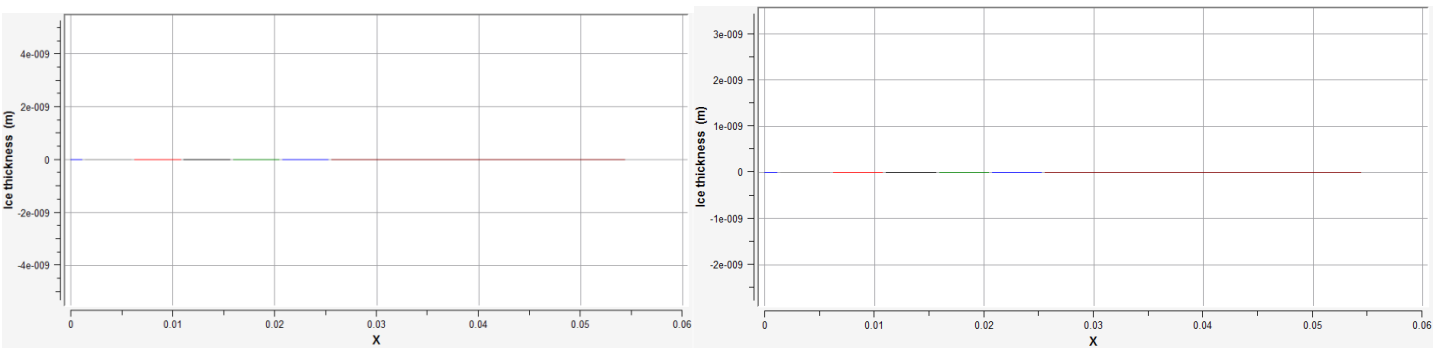


FIGURE 97: ICE THICKNESS PLOT (FREESTREAM TEMPERATURES OF -20C LEFT, -10 RIGHT)

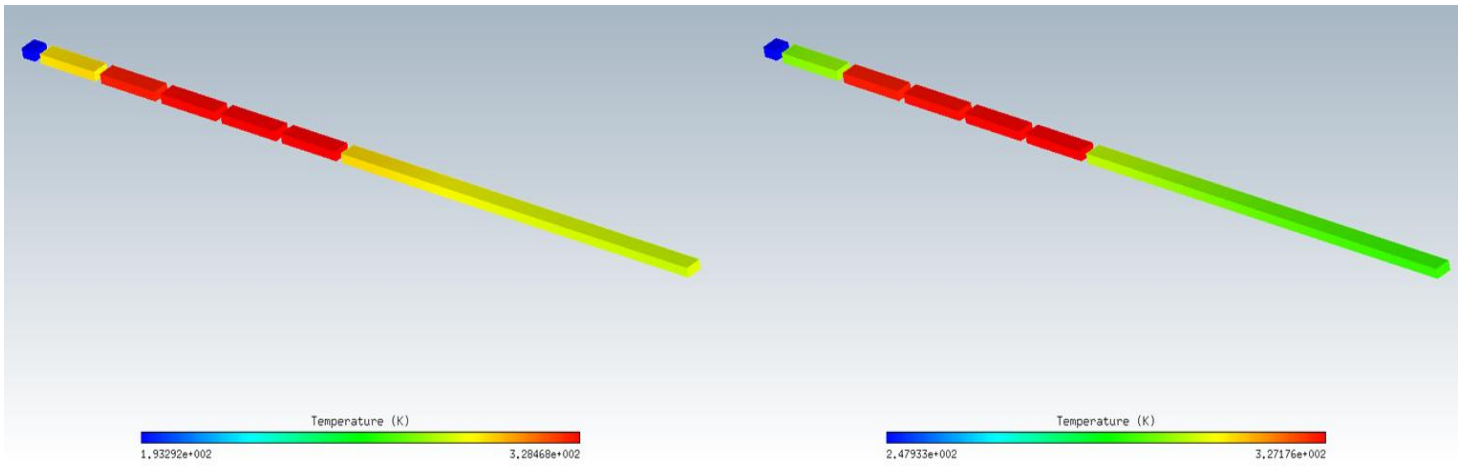


FIGURE 98: SOLID TEMPERATURE (FREESTREAM TEMPERATURES OF -20C LEFT, -10 RIGHT)